Real-Time Image-Based Transcranial Refocusing of Dual-Mode Ultrasound Arrays

A DISSERTATION
SUBMITTED TO THE FACULTY OF THE GRADUATE SCHOOL
OF THE UNIVERSITY OF MINNESOTA
BY

Hasan Ali Aldiabat

IN PARTIAL FULFILLMENT OF THE REQUIREMENTS
FOR THE DEGREE OF
Doctor of Philosophy

Prof. Emad S. Ebbini, Advisor

January, 2019

Acknowledgements

I would like to express my deepest gratitude and sincere appreciation to my advisor, Professor Emad S. Ebbini, for his continuous encouragement, helping and guidance through my years in graduate school at University of Minnesota. Prof. Ebbini, helped me reshape the way I think when approaching problems. He provided me an unlimited source of advice and knowledge that improved my understanding of ultrasound and many more subjects that would impact the rest of my life.

I am also grateful to the members of my committee: Professor Anand Gopinath, Professor Soheil Mohajer, and Professor Hubert Lim for reviewing my thesis as well as providing invaluable and insightful comments.

I would like to sincerely acknowledge Dr. Dalong Liu, currently at Siemens Healthineers and formerly a Research Assistant Professor in Dr. Ebbini's laboratory. My thesis research would not have been possible without the unique features of the *Software Designed Ultrasound* (SDUS) system designed and implemented by Dr. Liu.

I would like to thank my colleagues in Ultrasound and Signal Processing Laboratory (UISPL): Mr. Parker O'Brien, Mr. Anas Al-Hussayen, Mr. Collin Smith, Mr. Nayef Alshamlan, and Mr. Abhishek Sahoo for their help and support. They provided a great discussions and useful suggestions.

Many thanks go out to my previous professors and friends. Specially Professor Nihad Dib who kept tracking and encouraging me during my stay in the United

States, and my friends Mohamad Gharaibeh, Majdi Ababneh, Amr Tabari, Ahmad Sabbarine, and Mohammad Rawashdeh for their various forms of support during my graduate study.

A special thanks to Yarmouk University, National Institutes of Health, and International Cardio Corporation for funding me and my research during the graduate school years.

I would also like to express my gratitude to my family for their constant source of support and motivation through the hardest years of my life. My parents hardly sacrifice and dedicate everything they have to keep me up. Special thanks go to my uncle Rateb (may his soul rest in peace and heaven), he was the one who believed in me, he kept motivating and helping me through every step of my life.

Dedication

To my father, mother, and those who held me up over the years.

Abstract

Transcranial focused ultrasound (tFUS) is gaining wider acceptance in a range of therapeutic applications for the treatment of brain disorders. It represents a promising noninvasive modality for providing therapeutic ablative treatments as well as subtherapeutic treatments for brain conditions. Advances in image guidance modalities, especially MRI, have impacted progress and led to increased interest in tFUS-based therapies. While these advances have proved to be essential to improve tFUS applications, the precise delivery of localized tFUS beams is still difficult due to phase aberrations and attenuation of the beams by the skull. Compensating for these distortions requires refocusing techniques for ultrasound beams.

Based on the advent of dual-mode ultrasound array (DMUA) systems and their ability to operate in imaging and therapy modes in real time, we developed a real-time image-based refocusing algorithm to improve the safety and efficacy of tFUS therapy. The algorithm utilizes pre-beamforming DMUA echo data to perform optimal refocusing in multiple frequency bands within the transducer bandwidth based on user selection of the target and any critical points on the skull. The refocusing is performed by computing an improved estimate of propagation operators from the DMUA elements to the selected points, and then substituting the operators in the solution of the optimization problem for refocusing to calculate a refocused array excitation vector. The refocused vector minimizes the incident acoustic power at the critical point while maintaining or increasing the incident power at the target point.

In addition, the thesis experimentally demonstrated the feasibility of refocusing tFUS beams at a wideband range of operating frequencies. It also showed that the focusing gain improvement due to refocusing varies nonmonotonically as a function of frequency. In order to demonstrate this experimentally, we used

a set of 32 discrete frequencies that cover the frequency range from 1.9 to 5.0 MHz to generate tFUS beams with and without refocusing. The results clearly demonstrated the need to take the frequency dependence into account in the optimization of transcranial focusing. The results set the stage for the real-time implementation of optimal refocusing using wideband waveforms for improving the specificity and the localization of the focal region of the beam. In thermal therapy applications, this translates into enhancing the heating efficiency at the target location and minimizing the exposure over the skull. In neuromodulation applications, this translates into targeting brain circuitry with high degree of specificity to minimize inadvertent stimulation or inhibition of neural activity in non-targeted regions.

Contents

List of Tables

List of Figures

Chapter 1

Introduction

1.1 A Brief History of Medical Ultrasound

In 1944, the feasibility of using ultrasound for localized lesioning of deep-lying tissues without collateral damage to the intervening tissues in the path of the ultrasound beam was demonstrated. John Lynn and coworkers [1] showed that focused ultrasound (FUS) could successfully create reversible, partially reversible, and irreversible effects in brain and back tissues of animal models. The animals used during their studies received FUS doses for durations of 5 to 15 minutes to form lesions at targeted volumes. Well-defined lesions due to the ultrasound were observed after the histological examination of the targeted brain and back tissues.

In the 1950s, William J. Fry, a professor at the University of Illinois at Champaign, and his brother Francis J. Fry investigated ultrasound-induced bioeffects [2][3] [4]. The Fry brothers developed a four-transducer ultrasonic device that focused high intensity acoustic beams into a focal region of a few cubic millimeters. Figure 1.1 shows the ultrasonic device in the Biophysical Research Laboratory at the University of Illinois [5]. The device was utilized to form trackless lesions in the central nervous system of in vivo animals, including cats and monkeys. The Fry brothers performed comprehensive studies along with histological examinations to reveal the ability of FUS in creating reversible and irreversible effects in white

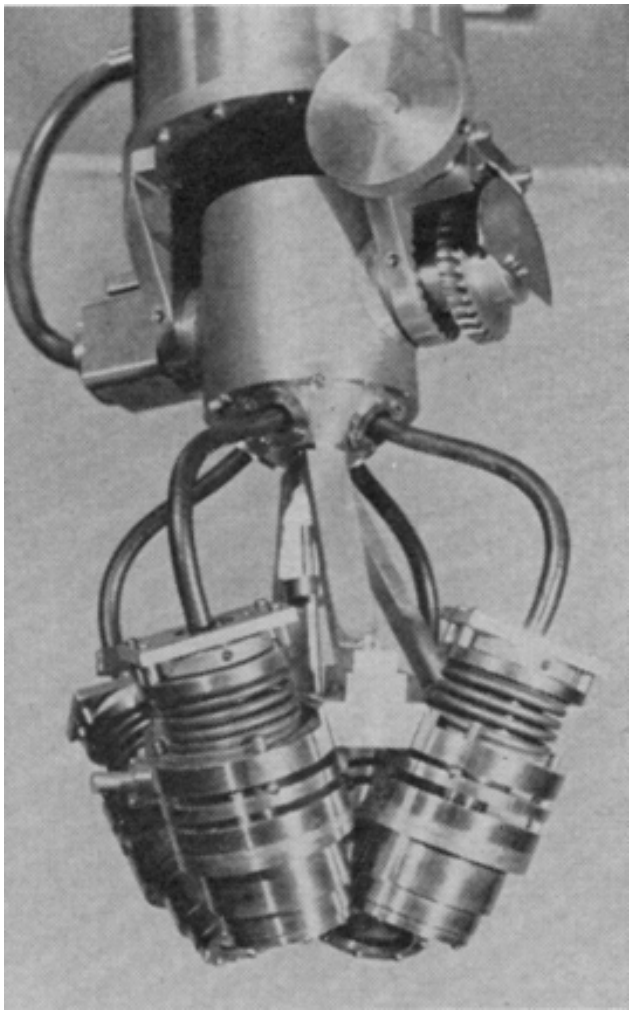

Figure 1.1: First multibeam focused ultrasound device.

and gray matter of brain tissues [6][7]. The studies paved the way towards a collaboration with Dr. Russell Meyers, Chief of Neurosurgery at the University of Iowa School of Medicine, to treat patients with various brain disorders including Parkinsons disease and tremors [5].

Until 1972, the prevailing doctrine about the mechanism of tissue damage using FUS was attributed to mechanical effects. This belief changed when Lele and coworkers [8] demonstrated that heat generation due to applying FUS has a

significant role in tissue destruction. The group performed *in vitro* and *in vivo* experimental studies to show the relationship between heat generation and the applied acoustic intensity level. They found that the ultrasound focal spot heat increases linearly with the intensity for intensity levels less than 1500 W/cm^2. However, at higher intensity levels, the linearity relationship vanished and transient cavitations appeared at the focal spot.

In spite of the aforementioned significant results, the high intensity focused ultrasound (HIFU) could not be moved from a laboratory to clinical usage by the time the results were released. This was due to the lack of FUS beam image guidance and monitoring capabilities as well as the difficulty in precise definition of beam dosimetry and the targeted location. To improve the safety and efficacy of FUS usage, the beam-tissue interaction and the temperature of the target tissue during the treatment have to be closely monitored to avoid any adverse effects of the beam. For example, the presence of blood vessels in the vicinity of the targeted location complicates the treatment due to the uncertainty in the tissue cooling process induced by the blood flow. Additionally, tissue layers of different acoustic and physical properties between the ultrasound transducer and the target location compromise the FUS beam reliability of targeting the intended location efficiently.

1.2 Overview of Current FUS Monitoring Modalities

Several techniques have been proposed for the monitoring and guidance of noninvasive and minimally invasive FUS application. However, the widely investigated and currently used techniques in clinics are magnetic resonance imaging (MRI) and ultrasound imaging. Both of the techniques have their own advantages and limitations as demonstrated in the following subsections.

1.2.1 MRI-Guided Focused Ultrasound

MRI-guided focused ultrasound (MRgFUS) is a safe, effective, and noninvasive treatment modality that utilizes MRI for target definition and providing a real-time temperature mapping of FUS usage. The modality is capable of detecting small temperature elevations in the treatment volume and its surroundings based on temperature sensitive MRI parameters, including proton resonance frequency and diffusion coefficient [9]. In addition, it has a high soft-tissue contrast and high spatial resolution as well as represents a nonionizing radiation tool, making it an attractive treatment option. MRgFUS has been used in the treatment of a variety of diseases, including breast fibroadenoma [10], brain tumors [11], and uterine fibroid treatments [12]. In 2004, the United States FDA (Food and Drug Administration) approved MRgFUS as a noninvasive treatment option for uterine fibroids. Figure 1.2 illustrates an MRgFUS machine example currently being used in the clinic.

Although MRgFUS has begun emerging as a noninvasive treatment option, there are still some limitations associated with its use. For example, the image acquisition duration required by MRI scanner is on the order of one second per frame [13], which may limit its compatibility with short FUS pulses that generate quick tissue heating. In addition to this, the claustrophobia and discomfort that some patients experience due the closed-bore design, the high cost of MRI systems, and the lack of portability are also considered limitations.

1.2.2 Ultrasound-Guided Focused Ultrasound

When ultrasound is used to guide and monitor ultrasound therapy, the modality is called ultrasound-guided focused ultrasound (USgFUS). Ultrasound imaging systems that support this modality are completely non-ionizing, therefore, it is possible to repeat focused ultrasound treatments without causing overdoses and without the risk of harming healthy tissues. Ultrasound, as compared to MRI, has high portability and low cost as well as it offers high imaging frame rate making

Figure 1.2: Example of currently available clinical MRgFUS machines. Image courtesy of InSightec Ltd.

it suitable to be used for moving organ treatments, such as liver. In addition, researchers have proved ultrasound capability to provide quantitative tissue property maps in the form of temperature [14][15] and elastography [16]. Perhaps the most attractive feature of USgFUS is the ability to use the same array transduce elements for both imaging and therapy. This feature has been achieved by the advent of dual-mode ultrasound array (DMUA) transducers [17]. DMUA transducers have inherent registration between its imaging and therapeutic coordinate systems, allowing for continuous feedback from the treatment location.

Ultrasound, the same as any other imaging modality, has some limitations. The major limitations of ultrasound include poor soft tissue contrast and the difficulty in penetrating boney structures. In addition, ultrasound cannot be used to image air-filled organs, such as lungs and digestive tracks.

Inspired by the advances in FUS monitoring and image guidance, several investigators conducted research to confirm the feasibility of using ultrasound transcranially to target brain tissues [18][19][20]. The significance of using ultrasound through the skull stems from the complexity of current brain treatment methods. The following section presents some of the treatment modalities utilized nowadays in clinics to treat brain disorders. In addition, it provides an overview of transcranial focused ultrasound (tFUS) modality and the limitations that hinder its use in clinical applications.

1.3 Overview of Brain Treatment Methods and tFUS

1.3.1 Clinical Brain Treatment Modalities

Treatment of brain conditions including tumors is usually a complex operation and may be life threatening; thus a decision about the treatment can feel overwhelming. It is important for the patient to work closely with medical doctors to determine the best treatment option, taking into account the type, size, and

location of the diseased tissues as well as the age and overall health condition of the patient. Currently, clinics have a number of options to treat brain disorders. These include surgery, radiation therapy, and chemotherapy. Each option has its own advantages and disadvantages as we can see from the following discussion.

Surgery, according to American Brain Tumor Association (ABTA), is the initial approach in the treatment of brain disorders including tumors. Even though brain surgery is a critical and complicated process, it is usually the selected treatment option when diseased brain tissues can be removed without the risk of severe harming of any parts of the nervous system. The approach is typically associated with craniotomy in order to remove a portion of the skull to obtain access to brain tissues as illustrated in Figure 1.3. There are several types of brain surgery that can be used depending on the targeted region in the brain and the condition being treated. The types include, but are not limited to, the following:

- Biopsy: A procedure used to extract a sample of brain tissues in order to examine it under a microscope. The procedure involves a small incision and a hole in the skull.

- Deep brain stimulation: This procedure is similar to the biopsy procedure in making a hole in the skull. However, instead of extracting a brain tissue sample, the surgeon inserts an electrode into the targeted region. Afterwards, he/she applies electrical signals to help mitigating some brain conditions, including Parkinsons disease.

- Endoscopic endonasal surgery: A minimally invasive procedure involves the use of endoscope. It allows the surgeon to insert the endoscope through the nose to access deficit brain tissues on and around the skull base.

As with any serious invasive surgical procedure, brain surgery is associated with some complications and life-threatening risks. However, different procedures, different targeted regions within the brain, and different patients have different forms of risk and side effects. Possible complications and side effects that might

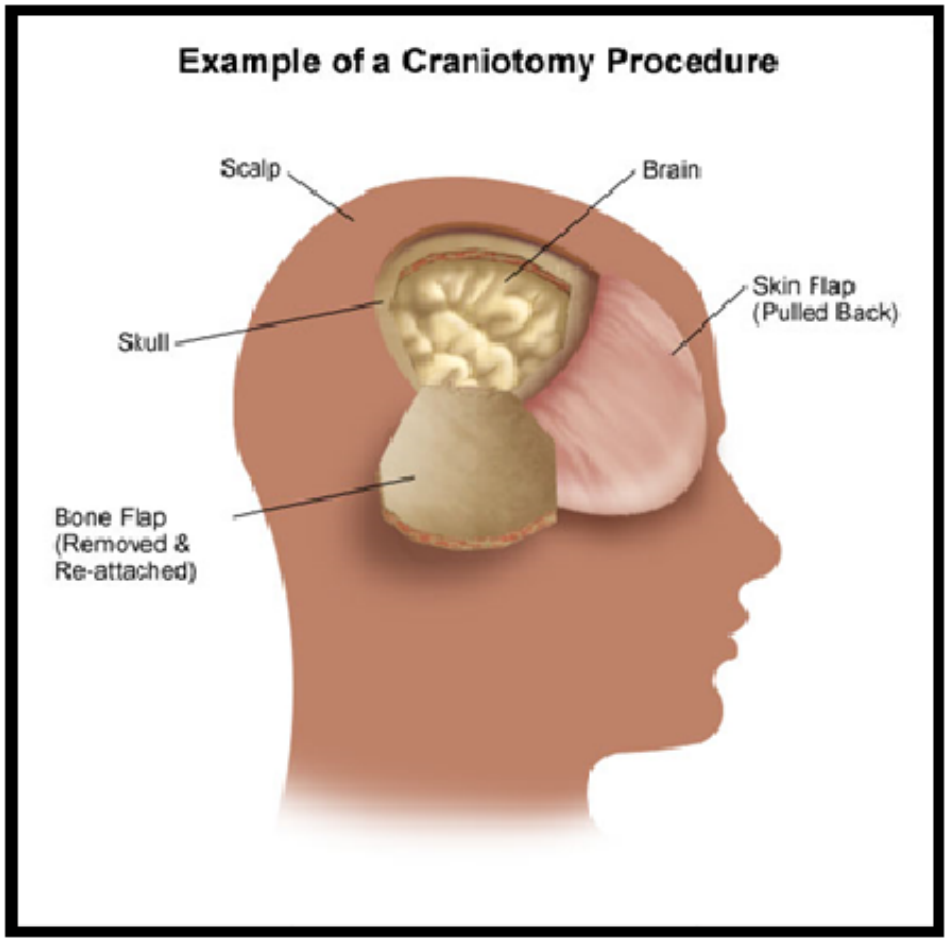

Figure 1.3: A schematic diagram illustrating the craniotomy procedure of brain surgery. Image courtesy of www.hopkinsmedicine.org

occur during and after brain surgery include the following: brain swelling, speech difficulty, memory problems, bleeding, blood clot, stroke and slow recovery.

In Radiation Therapy, high-energy electromagnetic radiations, including X-rays and gamma rays, are used to treat diseased brain cells. This type of therapy is utilized to target multiple tumors spread over different regions in the brain. This is because it is possible to subject the whole brain or specific part of it to the high-energy radiations. In addition, the therapy can be used alone or in combination with other treatment modalities to control the growth of cancer cells and shrink affected volumes. Based on the method used to deliver the radiations into the body, radiation therapy can be classified into many types, including, but is not limited to, the following:

- External beam radiation therapy (EBRT): EBRT represents the most common type of radiation therapy. It involves directing radiations into the tumor volume inside the body using a source from outside the body.

- Internal radiation therapy (IRT), also known as brachytherapy: IRT involves placing radioactive implant into or near the tumor volume inside the body. Consequently, the precise tumor location receives significantly high intense radiations and the amount of normal brain tissue damage reduced.

- Systematic radiation therapy, also known as radiopharmaceuticals: In this therapy type, a patient receives radioactive drugs orally or through an injection. The drugs travel in the blood throughout the body to locate and damage cancerous cells.

Radiation therapy, due to the nature of the ionizing radiations, has remarkable side effects even though they may not occur until two to three weeks after receiving the treatment. General side effects associated with the therapy includes hair loss, skin irritation, brain swelling, hearing problems, memory problems, and appetite changes. However, the severity of these effects may vary form one patient to another.

In Chemotherapy, patients take powerful drugs by mouth, injection into a vein, or directly into the brain during surgery to damage cancer cells. Temozolomide, procarbazine, and carmustine are among the most commonly used drugs to treat brain tumors. Chemotherapy can be used in conjunction with other brain treatment types, for example, it can be used after a surgery or radiotherapy to destroy remaining tumor cells. The main challenge of using this type of treatment for brain disorders is the presence of blood-brain barriers (BBB) that prevent drug passing into diseased cells.

Patients receive chemotherapy may have severe side effects and complications. Side effects depend on the drug type, drug used amount, and how patients' bodies react. Most common side effects associated with the therapy are hair loss, weight loss, fatigue, vomiting, and nausea.

1.3.2 Transcranial Focused Ultrasound

Transcranial focused ultrasound (tFUS), as the name implies, is utilizing FUS beams through the skull to target specific locations in the brain. Transcranial FUS modality is gaining wider acceptance in a range of therapeutic applications for the treatment of brain disorders. Advances in FUS monitoring and image guidance methods have encouraged researchers to investigate the biological effects of ultrasound in brain tissues transcranially [18] [21].

This modality confers advantages over currently existed clinical brain treatment tools including surgery, radiation therapy, and chemotherapy. It represents a promising nonionizing and noninvasive option for providing therapeutic and subtherapeutic (neuromodulation) treatments [22][23][24][25][26][27][28][29]. Essential tremor, brain tumors, Parkinsons disease and epilepsy are some of brain disorders that can be targeted by tFUS. For example, essential tremor (ET) which affects almost 10 million people in the United States according to Focused Ultrasound Foundation might be mitigated using FUS. ET is a neurological disorder that causes uncontrolled movements in different parts of the body, including arms,

hands, head, chin, and tongue. Several researchers have used MRgFUS to treat ET symptoms noninvasively [30][31][32][33]. Elias et al. [30] utilized MRgFUS to relieve ET symptoms in patient hands. Patients who experienced the treatment noticed that their tremor lessened by 47% and as a consequence their life quality improved. In addition to the aforementioned advantages, tFUS significantly limits the treatment morbidity and the recovery time as well as the financial cost of the treatment as compared to other treatment options.

The main challenge of targeting deep brain tissues transcranially using ultrasound beams and maintaining precise delivery of localized tFUS is the complex structure of the skull [34]. It is a complex propagation medium with nonuniform geometry and acoustic properties [35]. In addition, interfaces between soft tissues and skull as well as between cortical and trabecular skull layers are highly heterogeneous. This heterogeneity affects the transmitted and reflected acoustic energies of tFUS beam as it propagates through the interfaces. On average, skull tissues have a density of about 1807 kg/m^3 and speed of sound about 3000 m/s, whereas the density and speed of sound in soft brain tissues are about 1081 kg/m^3 and 1500 m/s [36], respectively. The high acoustic impedance mismatch between skull layers as well as between scalp/bone and bone/dura mater interfaces (Figure 1.4) shifts the acoustic focus and significantly distorts the FUS waveforms. Distortions lead to a severe loss in the acoustic power deposition of tFUS beams in the targeted volume deep in the brain. However, several research groups have developed and examined a variety of ultrasound aberration correction methods to compensate for distortions and achieve the highest possible focusing gain at targeted volumes [37],[38]. In this thesis, we developed and implemented a tFUS refocusing algorithm that improves the safety and efficacy of using the ultrasound as a treatment tool.

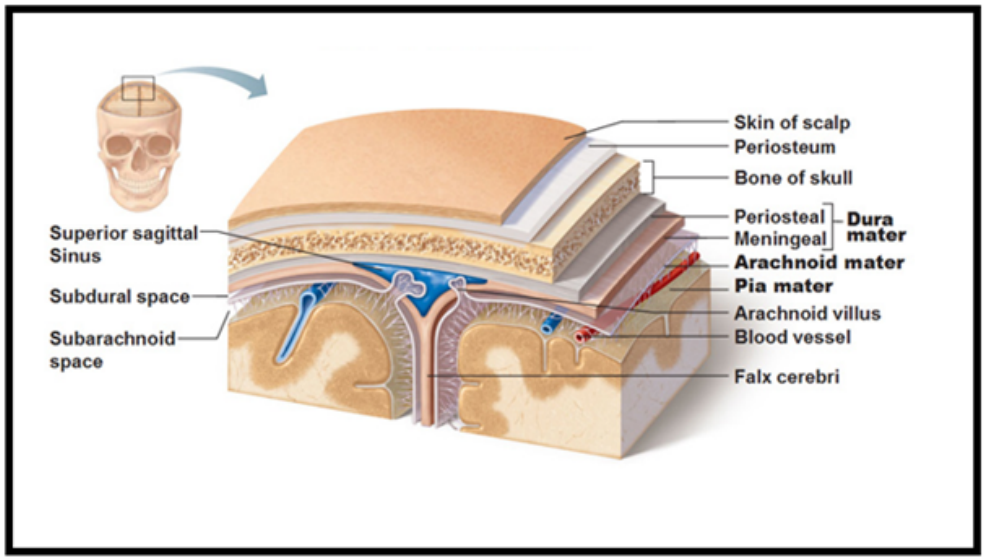

Figure 1.4: Cross section of human skull anatomy. Image courtesy of www.antranik.org.

1.4 Contribution of this Dissertation

This dissertation builds on the image-based refocusing algorithm described in [39] in the context of adaptive transthoracic targeting of liver tumors. It extends the optimal refocusing problem to targeting specific locations in the brain using DMUAs. The main goal of the refocusing algorithm is to optimally deliver tFUS beams at a target location behind the skull while minimizing direct incidence of the beams over a specific location of the skull. The algorithm benefits from some of the DMUAs advantages of operating in imaging and therapy modes in real-time and providing access to the pre- and beamformed imaging data. The algorithm utilizes the channel echo data of synthetic aperture (SA) imaging mode to find an improved estimate of propagation operators from the DMUA transducer elements to the selected target and critical points. The experimental validation of using pre-beamformed SA data in deriving the propagation operators is the main contribution of this thesis research.

Another important contribution of this thesis is the use of realistic *ex vivo*

experiment setup for demonstrating the feasibility of the proposed image-based refocusing algorithm. In particular, *ex vivo* skull samples were positioned in the path of the DMUA FUS beam to emulate the *in vivo* experiment setup [18]. Transskull FUS propagation was characterized using hydrophone measurements in water tank with reference to water-only measurements. In addition, *ex vivo* skull samples were embedded within tissue mimicking phantoms to demonstrate the effect of refocusing through heating. DMUA imaging and therapy modes of operation have been used to validate the tFUS beams refocusing effects. In imaging mode, the increase in echogenicity at the target location and the decrease in echogenicity value at the critical location over the skull were used as an indication of improving the focusing gain due to refocusing. In the DMUA therapy mode, direct temperature measurements along with heating rate computations were used to demonstrate the enhancement of focusing gain upon refocusing.

An experimental investigation of the transmission characteristics of *ex vivo* skull samples over a frequency range of 1.9 - 5.0 MHz was also conducted. The study was designed to confirm the nonmonotonic nature of the transmission as a function of frequency and the site-specific nature of the transmission loss. A grid of single point and planar acoustic hydrophone scan measurements with and without the skull have been performed to characterize the loss and distortion of tFUS beams. We have documented a range of tFUS beam distortions from mild shifting to complete splitting of the beam focal spot especially when the beam traversed portions of the skull containing suture lines such as the bregma. The acoustic measurements have been performed at a variety of target locations and access angles using a wideband needle hydrophone. The characterization measurements were also performed for refocused tFUS wavefronts at each frequency to quantify the improvement in focusing gain upon refocusing. To the best of our knowledge, this is the first study of its kind and it paves the way to the implementation of wideband refocusing of tFUS beams to optimize the specificity of their bioeffects in therapeutic applications, including thermal therapy and neuromodulation.

1.5 Dissertation Organization

This thesis includes this introduction and five additional chapters, which are organized as follows:

- Chapter 2 introduces the DMUA systems and their imaging capabilities. It provides a description of the DMUA imaging modes such as the synthetic aperture, single transmit focus, and 3D imaging. In addition, it provides a brief introduction of beamforming and image formation.

- Chapter 3 addresses the nature of tFUS beam distortions using an *ex vivo* experiment setup. In particular, it presents quantitative hydrophone measurements of FUS beams in water with the *ex vivo* skull in the path of the beam. These are compared with the reference water-only measurements to illustrate the loss in focusing gain as well as beam distortion.

- Chapter 4 introduces a real-time image-based transcranial refocusing algorithm capable of generating an optimal array excitation vector. The optimal refocusing algorithm minimizes direct acoustic incidence over specific skull location(s) while achieving a desired acoustic power deposition at a specified target point behind the skull.

- Chapter 5 describes an important extension to the research described in chapters 3 and 4. Specifically, it provides wideband transskull ultrasound transmission characteristics and refocusing results. It shows the results generated during *ex vivo* water tank and tissue-mimicking phantom experiments.

- Chapter 6 draws conclusions from the research results and provides suggested future directions for the current work.

Chapter 2

Dual-Mode Ultrasound Array System and Applications

2.1 Introduction

Image-guided noninvasive and minimally invasive surgeries are typically performed using an integration of two subsystems for imaging and therapy. For instance, the surgeries can be performed using MRI or ultrasound diagnostic imaging systems in conjunction with the therapeutic system. However, the advent of piezocomposite technology has offered a new paradigm in image guided FUS-based therapy. Piezocomposite materials are made of piezoelectric ceramic micro-rods embedded in a polymer matrix [40]. The availability of the technology makes it possible to have ultrasound array transducers with low cross coupling between the elements and an enhanced electroacoustic efficiency in terms of transducer sensitivities and signal to noise ratio. Additionally, it offers transducers of high operating fractional bandwidth of about 50% to 90% [41]. These features, specially the last one, enable therapeutic ultrasound transducers to operate in pulse-echo imaging mode. As a result, high-power dual-mode ultrasound array (DMUA) transducers have been designed and manufactured. DMUA transducers have the capability of switching between imaging and therapy modes intermittently; thus, they are able

to provide a continuous feedback before, during, and after therapy application.

2.2 DMUA System

The experimental results presented in this thesis were all based on the use of the DMUA illustrated in Figure 2.1(a). The DMUA prototype has been designed and manufactured using HI-1 piezocomposite technology (Imasonic, France) for tFUS applications. It has 64 element transducers and a concave shape of 40-mm radius of curvature. The prototype has a relatively low f_{number} of $\sim$0.89 in the lateral direction and $\sim$1.41 in the elevation direction. Together with the spherical concave geometry, these values yield a focusing gain of 4300 at its geometric center in water. In some experiments, during imaging and therapy applications, the DMUA was operating at a frequency of 3.2 MHz, while it was operating at its full bandwidth in other experiments. The DMUA elements are aligned in two rows of 32 elements per row, each element has a width of 1.3 mm and a height of 14.5 mm with inter-element spacing of 0.2 mm [42]. The element size and the sampling geometry of the concave spherical surface define the therapeutic operating field (ThxOF) for this DMUA prototype. The ThxOF is defined as the region around the geometric center where the focusing gain does not drop by more than 3 dB from the maximum value at (or very near) the geometric center. This is an important characteristic of a DMUA design. For this array, the ThxOF is elliptical with a major axis of 10 mm along the lateral direction and a minor axis of 5.4 mm in the axial direction.

The aforementioned DMUA specifications are well suited for the treatments of peripheral vessels in humans or large animals, which motivated the original design of the array. The dimensions of the ThxOF were also found useful for targeting brain tissues in small animals using focused ultrasound (FUS). Figure 2.1(b)shows the geometry of the DMUA prototype used in the refocusing experiments. The ring shown represents a target region around the geometric center, which fits within the ThxOF for this DMUA. In addition, some of the DMUA systems

that are available in our laboratory have an opening in its center, as illustrated in Figure 2.2(a). This opening allows the DMUA systems to be integrated with other systems including Sonix RP ultrasound scanner, manufactured by Ultrasonix Medical Corporation, British Columbia, Canada. The DMUA hole accommodates the Sonix RP HST15-8/20 probe as demonstrated in Figure 2.2(b). According to the probe specification sheet, the probe is a linear array with 128 elements and a geometric focus at 16 mm form the surface of the array. Moreover, it has an operating bandwidth of 7 MHz that covers the frequency range from 8 - 15 MHz. The scanner has the capability of performing real-time beamforming for conventional ultrasound imaging methods such as B-mode and M-mode imaging using various types of probes.

2.3 Overview of Beamforming Process

Ultrasound imaging systems support high imaging frame rates capable of displaying images in real time due to the nature of ultrasound image creation and the efficiently utilized beamforming techniques. Typically, an ultrasonic transducer has a number of piezoelectric elements that convert electrical pulses from the transmitters into acoustic waves. These waves travel into the body and hit boundaries as well as interfaces between tissues of different acoustic impedances. As a result, acoustic echoes are generated and reflected back to the transducer elements which convert the received echoes into electrical signals. On the receive side, each element of the transducer is connected to an analog to digital (A/D) converter which converts the received analog electrical signal into the digital domain to start the beamforming process.

A conventional beamforming process includes two main steps which are *delay and sum* [43]. Since transducer elements receive echoes at different time instances, depending on element distributions on the transducer surface and the location of the imaged point, appropriate time delays to align the echo signals are required.

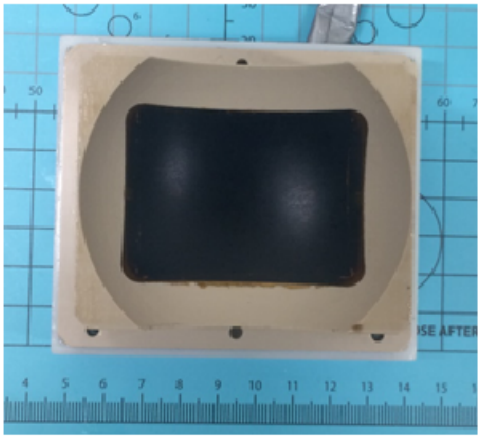

(a)

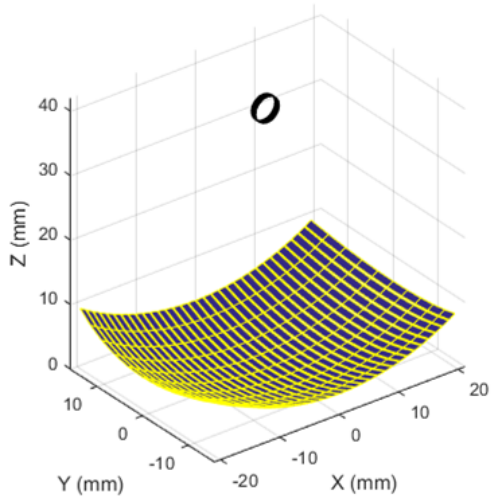

(b)

Figure 2.1: (a) Dual Mode Ultrasound Array prototype and (b) Rendering of the active surface area of the DMUA transducer. Segmentation in the elevation (Y) direction is for computational purposes.

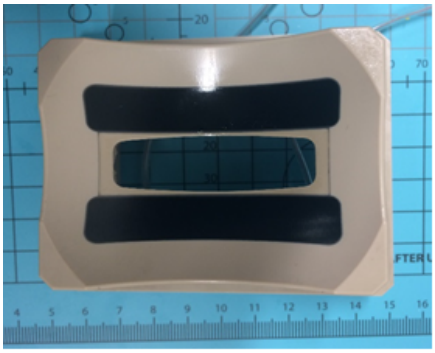

(a)

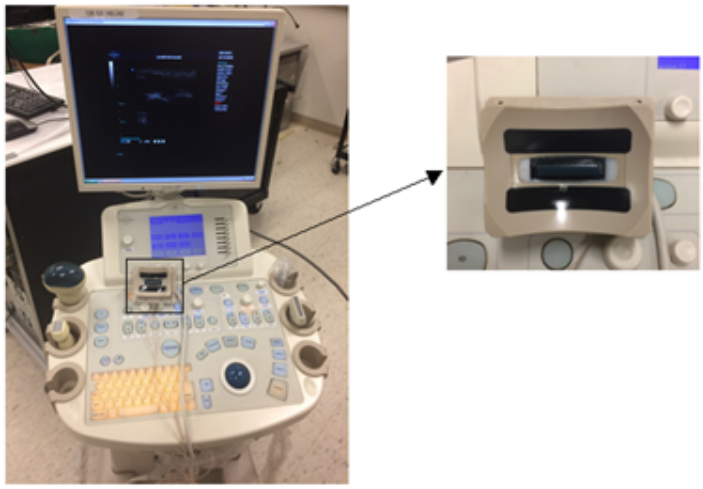

(b)

Figure 2.2: (a) Fenestrated DMUA prototype described in [64] and (b) Fenestrated DMUA integrated with Sonix RP ultrasound scanner.

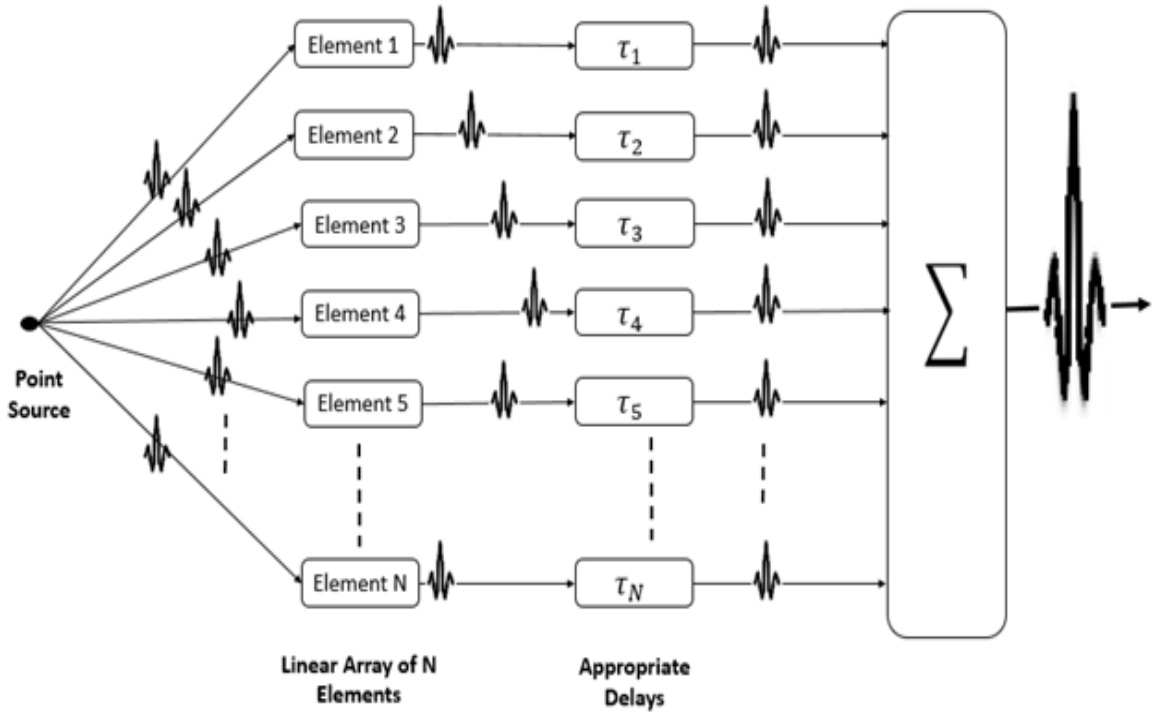

Figure 2.3: Basic principle of delay and sum beamforming.

Once the signals are aligned, they can be summed coherently to achieve better spatial resolution and higher SNR, which result in a better image quality. Figure 2.3 is a schematic diagram illustrating the *delay-and-sum* ultrasound beamforming. The figure shows that element 4 is the closest transducer element to the source point; hence, it receives the echo from the point source earlier than other elements. Therefore, a larger time delay is applied to channel 4 data compared to other channels to achieve echo alignment before summing the echoes for an estimate of the signal at the source.

High frequency A/D converter is required in order to form ultrasound images with high spatial resolution. The use of such an A/D converter makes it possible to collect ultrasound raw data with fine temporal resolution. For instance, a 1 ns time resolution requires a 1 GHz A/D converter. However, the use

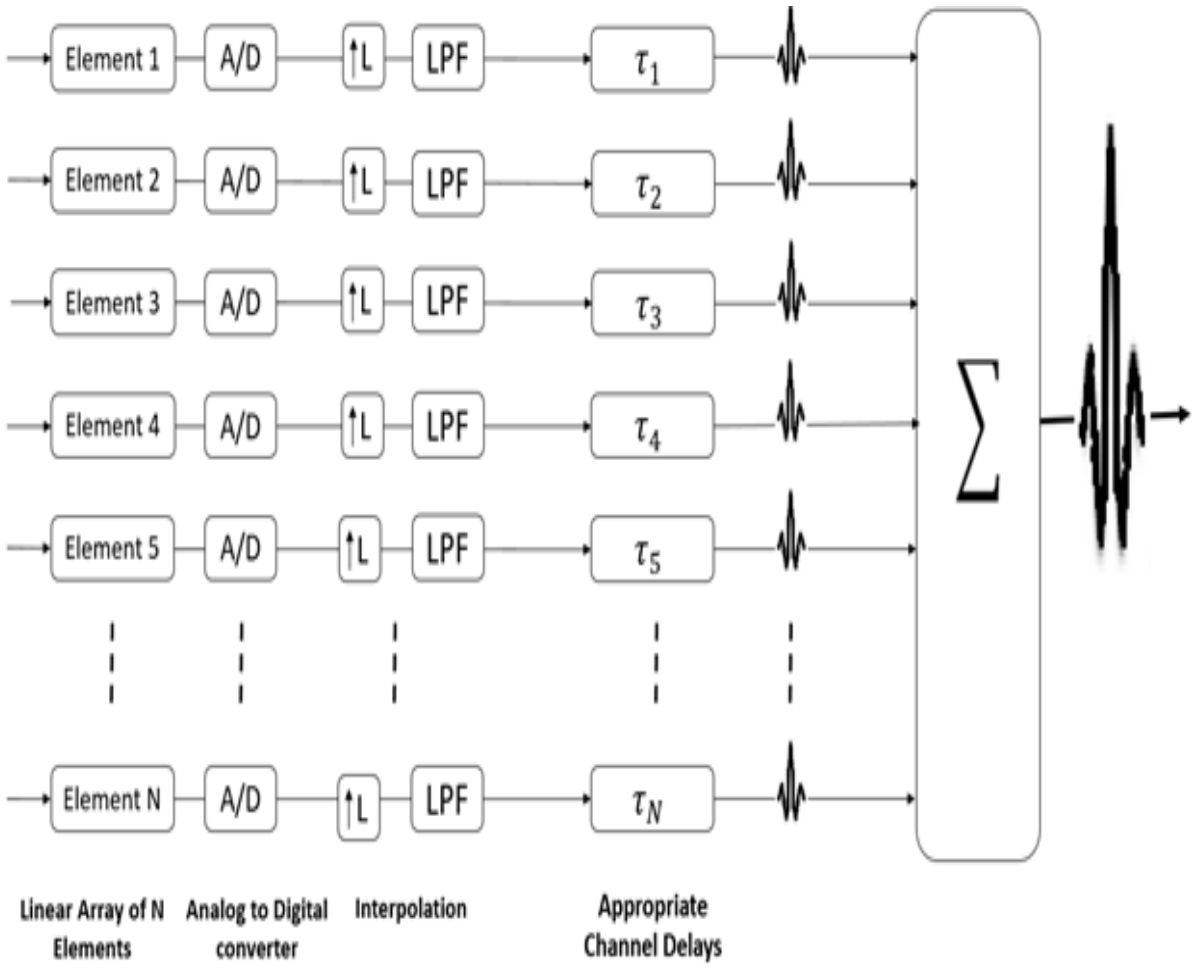

Figure 2.4: Block diagram of beamforming with interpolation.

of a very high frequency A/D converter is an impractical requirement. Therefore, most beamforming techniques perform interpolation process to substantially increase the sampling rate of ultrasound data that is sampled at lower clock frequency [43],[44],[45]. Interpolation is a signal processing technique composed of up sampling followed by low pass filtering [46]. Interpolation process is implemented before summing up echo signals from all transducer elements as illustrated in Figure 2.4.

In the following section, we discuss some of the DMUA imaging capabilities

that were used during the experimental studies of the thesis. The section demonstrates the basic principle of beamforming operation utilized by the DMUA system to create ultrasound images.

2.4 Overview of DMUA Pulse-Echo Imaging Modes

2.4.1 Synthetic Aperture Imaging

In the synthetic aperture (SA) imaging mode, images are formed using a full synthetic aperture technique with two-way (transmit-receive) dynamic focusing [42][47][48]. In this mode, the array elements are used as transmitters one at a time and echoes are recorded simultaneously on all receiving channels. For an N-element array, the imaging equation can be implemented by a delay-and-sum beamforming operation:

$$I(x_o, z_o) = \sum_{t=1}^{N} \sum_{r=1}^{N} A_t \cdot B_r \cdot S_{t,r}\left(\frac{R_{t,o} + R_{r,o}}{c}\right) D(\theta_t) D(\theta_r), \tag{2.1}$$

where A_t, B_r, c are the apodization weights for the transmitting and receiving elements, respectively. $S_{t,r}(\cdot)$ contains the channel data received by element r when t was the transmitter and c is the speed of sound (assumed constant). $R_{t,o}$ and $R_{r,o}$ represent the distances between the transmit and receive elements to the image pixel location (x_o, z_o) as illustrated in Figure 2.5.

$$\begin{aligned} R_{t,o} &= \sqrt{(x_o - x_t)^2 + (z_o - z_t)^2} \\ & \\ R_{r,o} &= \sqrt{(x_o - x_r)^2 + (z_o - z_r)^2} \end{aligned} \quad . \tag{2.2}$$

$D(\theta_t)$ and $D(\theta_r)$ are the transmit and receive element directivity weighting functions. Accounting for DMUA element directivities reduces the grating lobes and affects the SNR of the generated beam formed image. The directivity weighting function is defined as follows [42][17]:

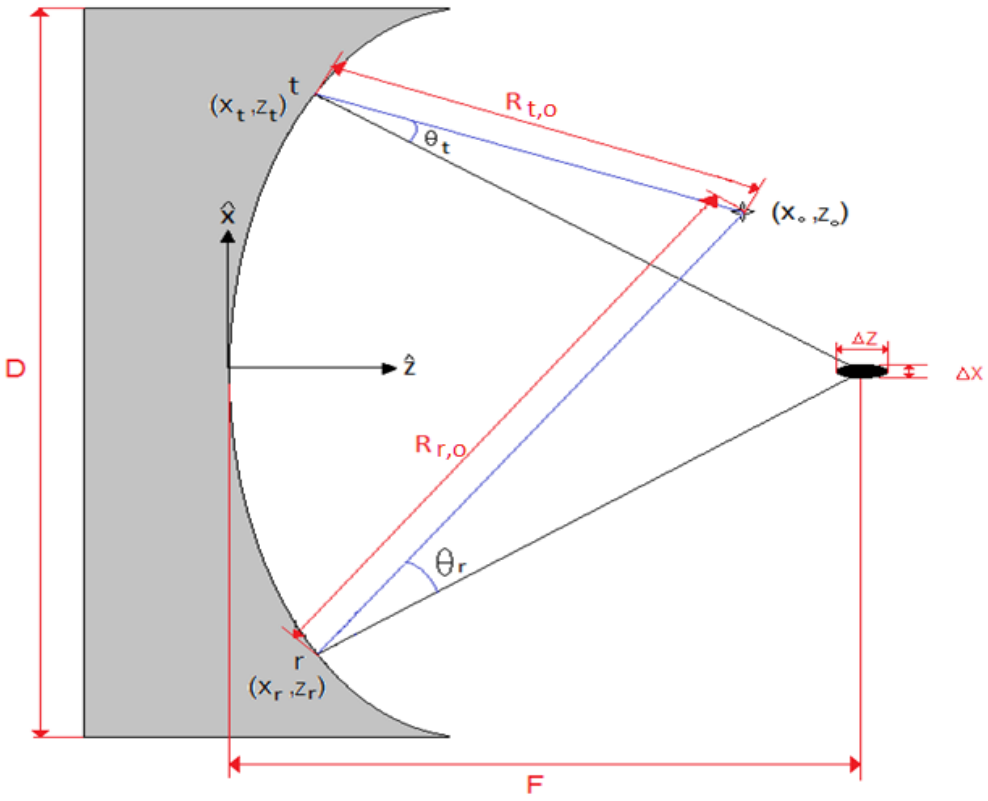

Figure 2.5: Schematic diagram shows the coordinate system of SA imaging.

$$D(\theta) = \frac{\sin[kd\sin(\theta)/2]}{kd\sin(\theta)/2}, \tag{2.3}$$

where k is the wave number ($k = 2\pi/\lambda$, λ is the wavelength), d is the width of each DMUA element and θ is the angle between the vector from the element to the image pixel (x_o, z_o) and the vector from the element to the DMUA geometric center.

There are some implications associated with Equation 2.1. This includes:

- At each pixel location, the image formation is equivalent to focusing the array on both transmit and receive. This represents a spatial matched filtering operation, which maximizes the SNR at each pixel location.

- In its current form, Equation 2.1 oversimplifies both wave propagation and scattering aspects of the imaging problem. For example, it ignores the heterogeneity of the propagation medium, the frequency dependence of the scatterer and multiple scattering.

- In soft-tissue media, acceptable image quality can still be obtained despite the oversimplifications. When the imaging beams have to traverse strongly-scattering obstacles, significant degradations are encountered.

- In modern imaging systems, which allow access to receive channel data from all transmissions, SA data provide the opportunity to improve the image reconstruction quality. This could be achieved by considering Equation 2.1 as a first approximation in an iterative refocusing based on the updated channel data from multiple transmissions.

- SA channel data is a valuable resource for defining optimal focusing on both transmit and receive. When combined with the DMUA concept, SA data could be used to improve the quality of tFUS beams generated by the same array. This is a unique advantage over any other refocusing method based on a separate image guidance system, including a different diagnostic ultrasound array.

We took advantage of the availability of SA imaging mode in every experiment related to this thesis. Figure 2.6(a) shows a 40-dB grayscale SA image of a needle hydrophone formed by Equation 2.1. The hydrophone tip was located at the geometric center (0mm in lateral direction and 40mm in the axial direction) of the DMUA. It is clear from the image that the hydrophone is correctly registered with maximum intensity at the geometric center. The DMUA system designed and implemented in our laboratory supports simultaneous therapy and monitoring using SA imaging mode at a frame rate of 30 frame per second.

2.4.2 Single Transmit Focus Imaging

One major advantage of the DMUA approach is the use of the same beamforming parameters for transmit focus patterns in both imaging and therapy modes. This has led to a unique imaging mode referred to as single transmit focus (STF) imaging [17]. In this mode, the array excitation waveforms are waveforms of μsec durations, but otherwise mimic the characteristics of the therapeutic beams excitation waveforms (much longer in duration and/or higher amplitudes). Mathematically, STF imaging produces high frame rates (one frame per transmission) according to the delay-and-sum beamforming equation:

$$I(x_o, z_o) = \sum_{r=1}^{N} B_r \cdot S_r\left(\frac{R_o + R_{r,o}}{c}\right), \tag{2.4}$$

with the same parameter definition as in Equation 2.1. $S_r(\cdot)$ is the received echo at DMUA element r in response to the transmit beam. R_o is computed based on the average distance between the large transmit aperture and the image pixel at location (x_o, z_o). STF imaging has important advantages in image-guided therapies employing FUS:

- At or near the intended focus, STF achieves the same levels of SNR and spatial specificity as SA. Therefore, STF imaging provides high SNR echo

data from the focal region of a FUS beam with the same beamforming characteristics.

- Outside the focal region, STF imaging is less sensitive and suffers some geometric distortion due to the use of fixed transmit delay R_0/c. Despite these limitations, however, STF imaging gives feedback about the nature of interactions between the FUS beam and the tissue volume it traverses. This includes possible obstacles in prefocal regions and other significant structures distal to the focus.

- In the context of transcranial FUS, STF images (approximately) show the intersection of the tFUS beam with the portion of the skull in its path. They also show the intersection of the diverging beam with the opposite side of the skull.

- Combining STF with the more spatially accurate SA imaging allows for the identification of any critical structures in the path of the tFUS beam.

Echogenicity of STF images provides a method to characterize the feasibility of the developed refocusing algorithm. Increasing the echogenicity at a target location is an indication of increasing the acoustic power deposition at that location. On the other hand, decreasing the echogenicity at a critical location is an indication of reducing the acoustic power deposition at the selected critical location. Figure 2.6(b) shows a 40-dB grayscale STF image of a needle hydrophone formed by Equation 2.4. The hydrophone tip was located at the geometric center of the DMUA. It is clear from the image that the hydrophone is correctly registered with maximum intensity at the geometric center. The DMUA system that we have in our laboratory supports a frame rate of 500 fps in STF imaging mode.

According to [42],[49], there is more than one method to assess the ultrasound imaging system performance based on spatial resolution. This includes the 6-dB value of the axial and lateral envelope traces that pass through the maxima of wire target images. In addition, the spatial resolution (the lateral and axial

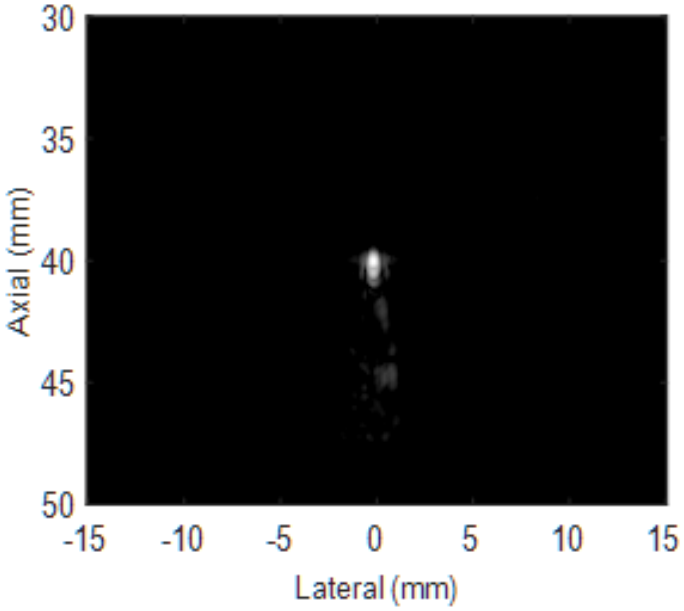

(a)

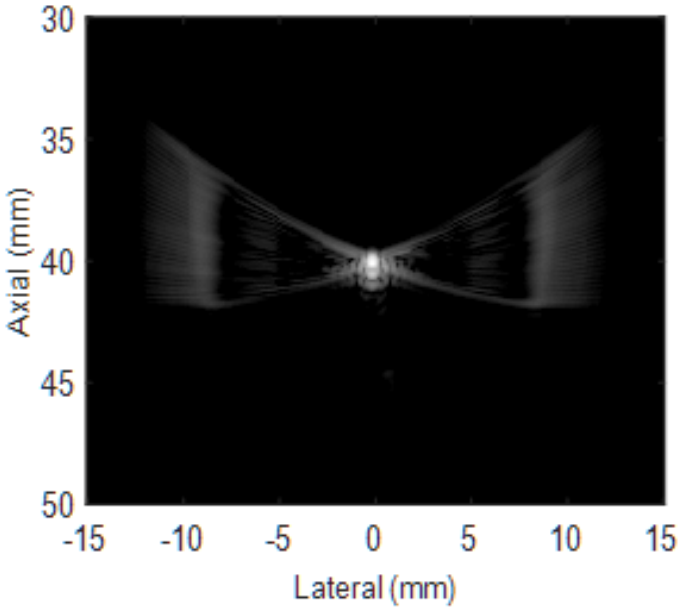

(b)

Figure 2.6: Grayscale (40 dB) Images generated using the DMUA shown in Figure 2.1: (a) SA and (b) STF.

resolutions) can be assessed based on second order statistics. This is performed by selecting uniform speckle regions from the target volume on the image and then calculating the speckle correlation cell size.

2.4.3 Three-Dimensional Imaging

DMUA systems are capable of generating 3D images to guide the application of tFUS beam to specific locations within the brain defined with reference to the skull medial suture lines [50]. The 3D images clearly resolve the dorsal aspect of the skull, including bregma, lambda and medial suture lines. This allows for an accurate placement of the DMUA focal spot at the intended target volume. In addition, the 3D images provide the capability of localizing the target volume in a repeatedly manner within a single experiment and from one experiment to another. This is important for conditions that require targeting the same location using tFUS beam multiple times during different experiments, including temporal lobe epilepsy.

Figure 2.7 shows an example of a 3D volume scan of a rat skull and an axial-lateral view of it. From the 3D volume scan image, one can clearly identify the bregma, lambda and medial suture lines of the skull as well as important skull components including occipital, parietal and frontal bones. The image is created using the DMUA system that we have in our laboratory according to the following procedure:

1. Locating the DMUA imaging slice at the starting scan position using SA imaging mode.

2. Moving the DMUA at a speed of 0.5 mm/sec from the caudal to rostral direction to cover the skull while collecting SA imaging data (approximately 60 frame/mm). The DMUA is moved by a 3-stage motor synchronized with the transmit frame trigger of SA imaging mode.

3. Rendering the 3D collected data directly after covering the skull (about 18

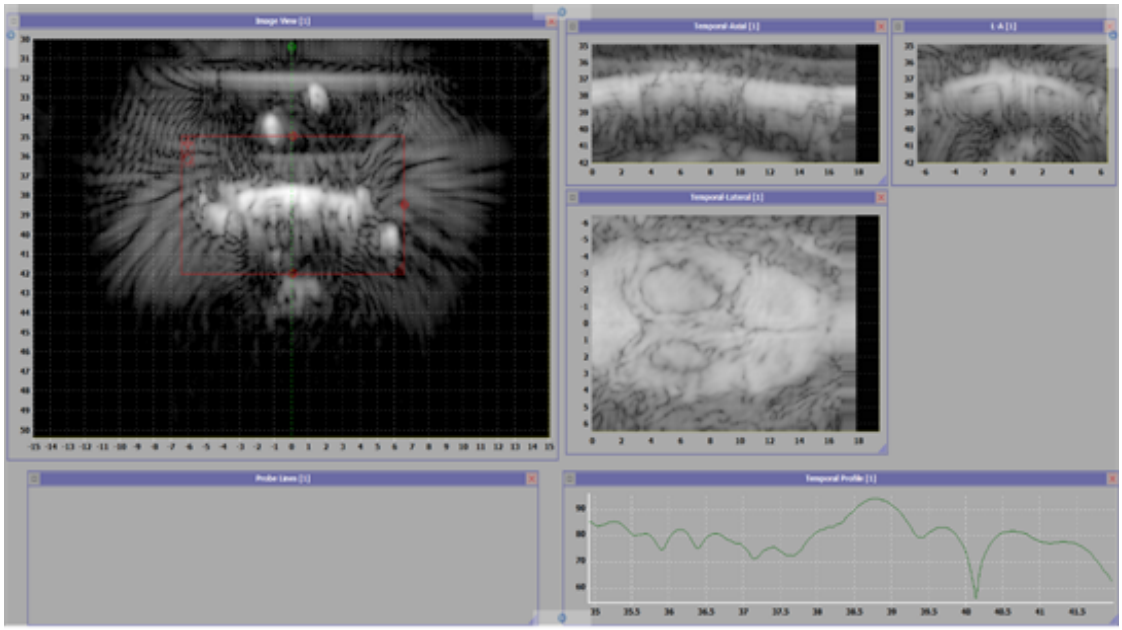

Figure 2.7: Skull geometry demonstration after rendering the 3D volume scan collected data.

mm) using the DMUA render engine.

Chapter 3

Characterization of tFUS Beam Transmission

3.1 Introduction

Several research groups have investigated the use of focused ultrasound (FUS) to target specific locations in the brain noninvasively. However, the presence of the skull in the path of the FUS beam represents a significant challenge. The FUS wavefront traversing the skull suffers potentially severe attenuation and significant distortion. This could compromise the focusing intensity gain at the target in addition to dispersing the energy in a larger volume, which could reduce the specificity.

In addition to the skull irregular shape and nonuniform thickness, the skull itself has several bone layers. For example, the human skull is composed of three layers of different levels of porosity. It has a trabecular porous volume surrounded by two cortical dense bones. The trabecular porous volume is called diploë and the cortical bones are called outer and inner tables. The speed of sound as it propagates through different layers of the skull varies approximately from 3100 m/s in the cortical dense regions (outer and inner tables) to 1500 m/s in the porous volume (diploë) [51]. In addition, skull tissue density varies significantly

from one region to another. In the cortical dense region the density is almost 2200 kg/m^3 while it is around 1000 kg/m^3 in the porous region. These values are spatially heterogeneous with large level of variability from subject to subject. Combined with the irregular curvature of the skull bone(s) intercepting the FUS wavefront, the severity of the distortions become more significant when targeting deep structures within the brain. In spite of the aforementioned obstacles, some research groups have investigated the use of ultrasound through the skull to form trackless lesions in brain tissues of animal models noninvasively. This was based on the fact that some of the ultrasound energy can propagate through the complex structure of the skull [51],[52],[53].

In this chapter, we present results from *ex vivo* studies to characterize the distortions of the FUS intensity profiles at the target due to the presence of the skull in the path of the beam. Planar acoustic intensity measurements in water using a hydrophone with and without *ex vivo* skull samples are performed for a variety of target points.

In addition, the variation in ultrasound acoustic energy at several selected points after different skull samples has been investigated and will be shown throughout the chapter.

3.2 Methods

Ultrasound beam deformations due to the presence of the skull were characterized using a dual-mode ultrasound array (DMUA) prototype and a wideband 200 μm needle hydrophone (Onda Corporation, Sunnyvale, CA). A wideband DMUA (64 elements, concave with 40-mm radius of curvature) was used to image and generate therapeutic focused ultrasound beams through water and rodent skull samples *ex vivo*.

The DMUA was first securely fixed in a tank filled with a degassed/deionized water and then the hydrophone was immersed in the water tank with the help of a 3-stage motor (Parker Daedal Division). Each stage is connected to a separate

controller (Quicksilver Controls Inc.) which is controlled remotely by a custom designed software embedded in the ultrasound system. The hydrophone shaft was horizontally localized with the DMUA imaging slice and its tip was positioned at the geometric focal point of the DMUA (0 mm in the lateral direction and 40 mm in the axial direction from the DMUA apex) with the guidance of SA imaging mode. Afterwards, lateral-elevation focal plane scans cover a distance of 10 mm in the lateral direction and 10 mm in the elevation direction were performed using the hydrophone.

In addition, we designed and generated multiple-frequency waveforms to perform planar acoustic hydrophone scans with and without the presence of rodent skull samples. All of the considered frequencies were within the DMUA transducer bandwidth. Each waveform was composed of several frequencies separated in time, this will be demonstrated in the next section. To perform the acoustic scans, we first pushed the generated waveforms into the ultrasound system, and then utilized the availability of arbitrary waveform settings in the hydrophone scan control architecture to use the generated waveforms in producing tFUS beams.

During the scans, the DMUA was transmitting focused ultrasound beams into the water medium and the hydrophone was programed to capture the ultrasound pressure signals at resolutions of 0.05 mm and 0.1 mm in the lateral and elevation directions, respectively. The captured signals were amplified using an AH2010 preamplifier and acquired by a Tektronix oscilloscope at a 50 MHz sampling rate. Then, the data transferred to a computer via an Ethernet cable and saved automatically.

In addition to the planar acoustic hydrophone scans, a grid of single-point hydrophone measurements have been performed. The points were selected within the therapeutic operating field (ThxOF) of the DMUA to characterize the acoustic transmission characteristics after different locations of the skull. In particular, we selected five different points to position the hydrophone tip with the help of the 3D-stage motor and the SA imaging guidance. The points were selected at the DMUA geometric focus and ± 2 mm in each of the lateral and axial directions away

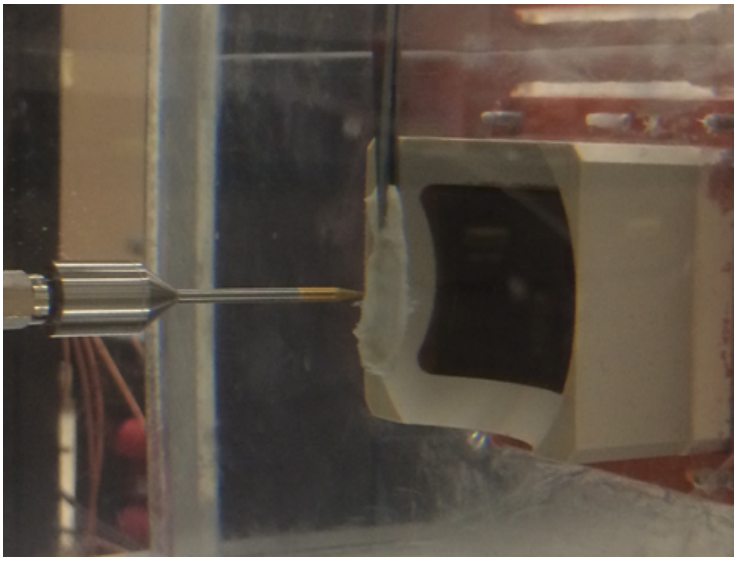

Figure 3.1: Water tank experimental setup showing the DMUA attached to the tank, the hydrophone location, and the skull.

from the geometric focus. At every point location, the DMUA was operated using the arbitrary waveform settings of SA imaging mode where a user can design a waveform and push it into the ultrasound system. The DMUA transducer elements were excited by a 3.2 MHz, sinusoidal, raised cosine weighted waveforms of 5 μs duration.

Both the focal plane hydrophone scans and the single-point hydrophone measurements were repeated after introducing a rat skull between the DMUA and the hydrophone tip. The skull was positioned at a distance of approximately 32-mm from the apex of the DMUA, such that the focal point was 8 mm behind the skull surface. This location is corresponding to the skull position during the in vivo experiments that we run in our laboratory. The skull was hold in the water tank with the help of forceps as illustrated in the experimental setup figure (Figure 3.1) which shows the DMUA, the hydrophone and the skull location.

The scans and single point measurements were performed to characterize and quantify the loss and distortion in ultrasonic acoustic energy due to presence of

the skull. The same experimental procedures that were used before introducing the skull in the water tank were followed after skull insertion. However, a three-dimensional volume scan of the inserted skull was added to the procedure in order to identify important landmarks over the skull and specify the exact portion of the skull being traversed by the ultrasound beam.

3.3 Results

We present the findings of *ex vivo* experimental studies that are performed to characterize and provide quantitative measurements of the loss and distortion in tFUS beams as they propagate through the skull. This section addresses the following aspects of the carried studies: 1) DMUA imaging capability of localizing the hydrophone tip at the geometric focus of the DMUA and identifying the dorsal aspect of the skull to guide the tFUS application, 2) planar acoustic pressure measurements with and without skull samples at a range of operating frequencies, and 3) a grid of single-point hydrophone measurements that characterize the transmission efficiency of the tFUS beam over different locations of the same skull.

3.3.1 DMUA Imaging Guidance

Synthetic aperture (SA) imaging mode of the DMUA was used to guide the placement of the hydrophone inside the deionized/degassed water tank. The needle tip of the hydrophone was exactly localized at the geometric focus of the DMUA. Figure 3.2(a) shows an SA image data collected experimentally using the setup described in the previous section before introducing the skull. The figure clearly demonstrates that the hydrophone is correctly registered with maximum intensity at the geometric focus. After inserting the skull between the DMUA and the hydrophone tip, the tip could still be visualized, however, with a degraded resolution as can be depicted in Figure 3.2(b).

The 3D imaging capability of the DMUA technology was used to identify

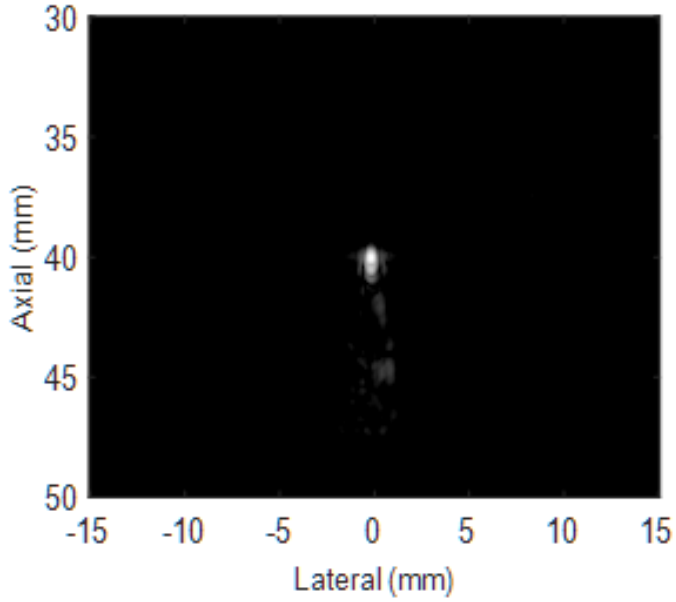

(a)

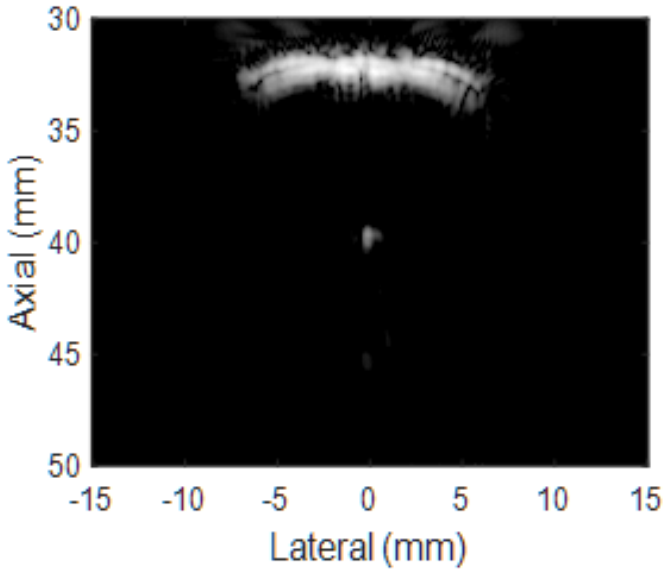

(b)

Figure 3.2: Grayscale (40 dB) SA images of the needle hydrophone at the DMUA geometric focus: (a) before introducing the skull and (b) after introducing the skull.

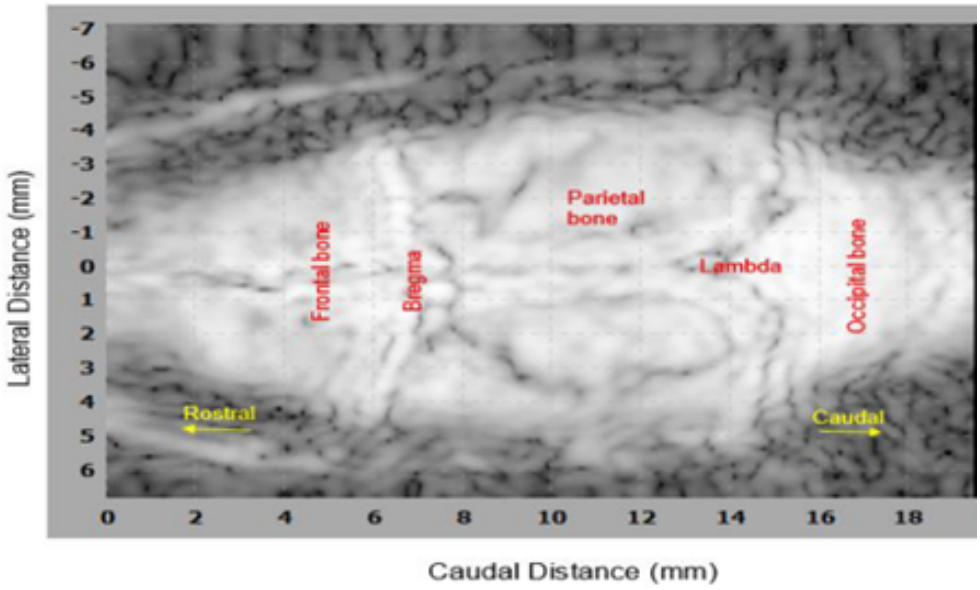

Figure 3.3: Three-dimensional volume scan of the skull demonstrates the dorsal aspect of the skull.

important landmarks over the skull. Figure 3.3 is a 3D volume scan image of the skull shown in the experimental setup. As we can see from the figure, the dorsal aspect and the complex structure of the skull, including the frontal, parietal, and occipital bones as well as the suture lines, are clearly visible. Results in the next subsections show a clear correlation between the selected DMUA imaging slice through the skull and the distortion as well as the loss in acoustic power deposition behind the skull. In most of the transcranial experiments that we ran, the application of tFUS was kept between the bregma and lambda suture lines.

3.3.2 Characterization of Transskull FUS Beam Distortion

Extensive hydrophone scans were performed to visualize the DMUA ultrasonic beams in a deionized/degassed water tank with and without the presence of rodent skull samples. The planar scans were coincide with the DMUA focal plane in the elevation and lateral directions. Several skulls have been tested to characterize the

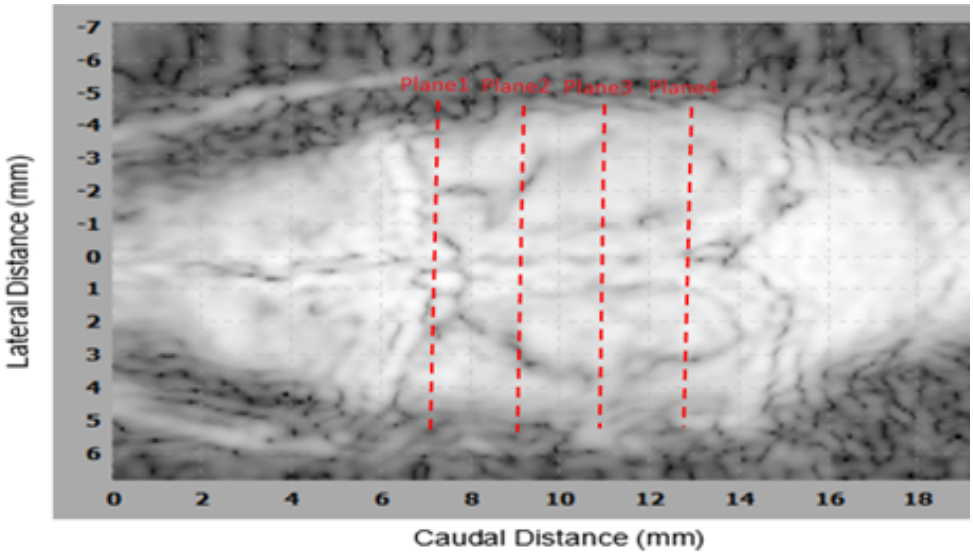

Figure 3.4: Locations of planes selected over the skull through hydrophone scan experiments.

distortion and transmission efficiency of tFUS beam as it propagates through the bone. Moreover, different locations over the same skull have been investigated. In all tested skulls, the tFUS beam was experiencing distortions and loss in acoustic energy at the focal plane.

In our *ex vivo* experiments, we used the bregma and lambda suture lines as a reference to specify the scan planes. The planes were selected to be at distances of 0.5, 2.5 4.5, and 6.5-mm away from bregma towards lambda, respectively. These selection were made possible by the help of the 3D volume scan of the skull as demonstrated in Figure 3.4.

Hydrophone scan example results in the water tank before and after introducing the skull are shown in Figure 3.5. The tFUS beam was generated at an operating frequency of 3.2 MHz. The ultrasound intensity was scanned in the focal lateral-elevation plane, which is normal to the transducer surface, using the needle hydrophone. The acoustic intensity amplitudes shown in the figure are normalized with respect to the maximum intensity measurement achieved in water without the skull. Figure 3.5(a) illustrates the water scan results without the skull. It is clear from the figure that the ultrasound intensity is well localized at the focal region with almost no distortion. Figures 3.5(b), 3.5(c), 3.5(d), and 3.5(e) show the acoustic intensity amplitudes after skull insertion. The Figures (3.5(b), 3.5(c), 3.5(d), and 3.5(e)) demonstrate the scan results when plane one (bregma -0.5), plane two (bregma -2.5), plane three (bregma -4.5), and plane four (bregma -6.5) were selected respectively.

Compared to the water scan (Figure 3.5(a)), there is a degradation in ultrasound intensity amplitude in all scanned planes of the skull. In addition, distortion and spreading in ultrasound intensity at and around the focal point due to the skull are clear in the figures. However, the severity of these complications varied from one plane to another. The variation was dependent on the selected plane locations over the skull because different plane have different bone shape and thickness.

The normalized ultrasound intensity line plots in the lateral and elevation directions with and without the skull are illustrated in Figure 3.6(a) and Figure 3.6(b). The plots are normalized with respect to the maximum ultrasound intensity of the plain water scan (without the skull). The left y-axis of the figure represents the intensity profile of a plain water scan while the right y-axis represents the intensity profiles measured behind the selected planes through the skull. The results show that there is more than a 70% reduction in the amplitude of the maximum ultrasound intensity at the geometric focus of the DMUA due to the distortion and absorption by the skull.

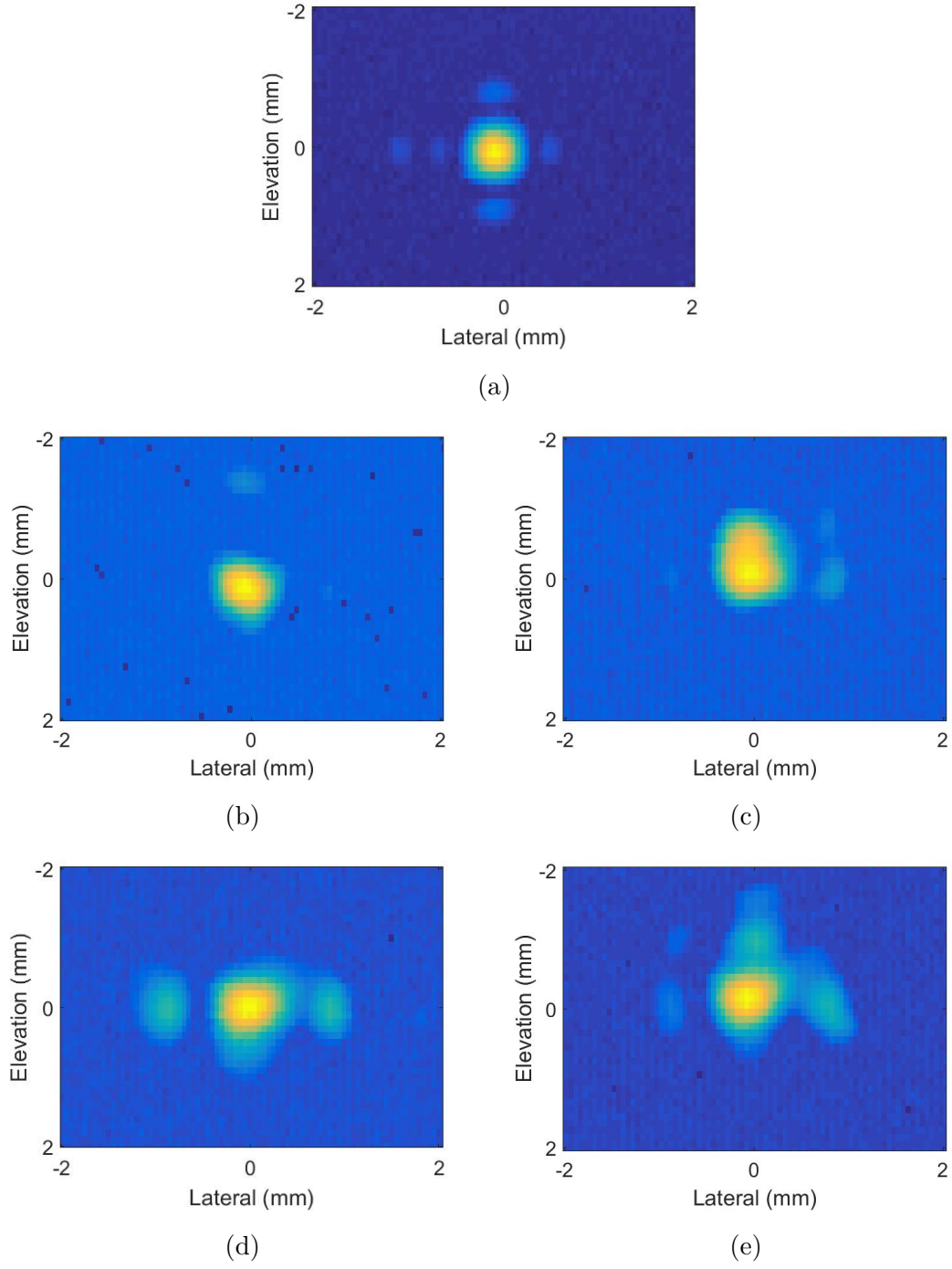

Figure 3.5: Ultrasound intensity profile measurements using a needle hydrophone: (a) Reference measurement without the skull, (b) Plane 1, (c) Plane 2, (d) Plane 3, and (e) Plane 4 (See Figure 3.4).

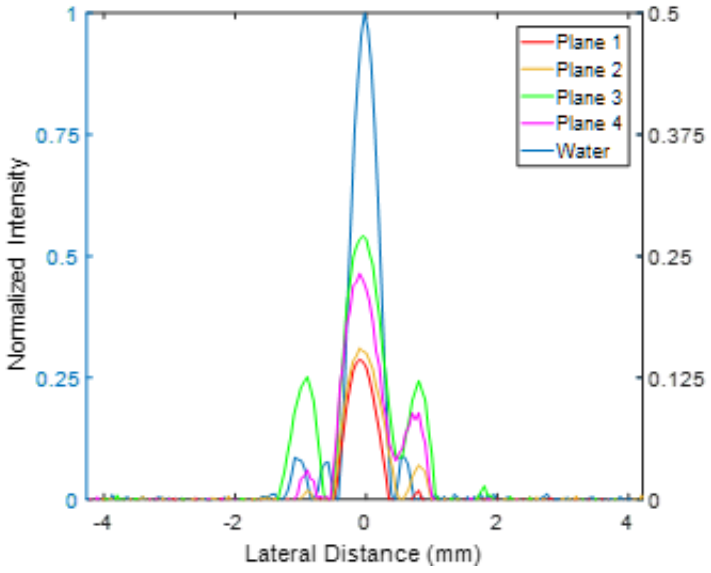

(a)

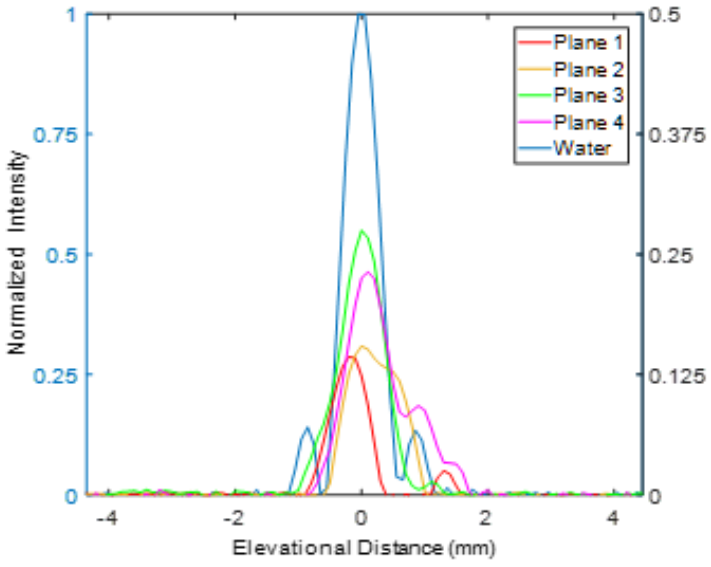

(b)

Figure 3.6: Normalized ultrasound intensity line plots: (a) Lateral Direction; (b) Elevation. Left ordinates are for the reference profiles while the right ordinates are for transskull measurements.

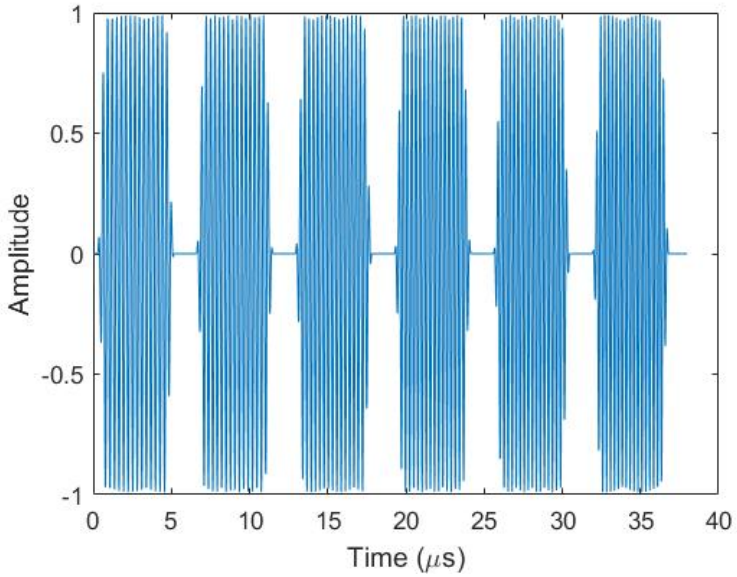

Figure 3.7: Signal composed of six narrowband pulses centered at 3.1, 3.2, 3.3, 3.4, 3.5, and 3.6 MHz.

3.3.3 Characterization of Acoustic Transskul Transmission Using Multiple Frequency Waveforms

In addition to the 3.2 MHz signals that are used to generate tFUS beams, we designed and generated multi-frequency signals to perform hydrophone scans. Each signal composed of several narrowband pulses separated in time domain. All narrowband pulses were having the same duration and gated using a raised cosine weighting function. The signal shown in Figure 3.7 consists of six consecutive narrowband pulses at frequencies 3.1, 3.2, 3.3, 3.4, 3.5, and 3.6 MHz. The signal was used to perform planar acoustic pressure measurements using the hydrophone with and without the skull presence. The availability of the 32-channels, FPGA based, arbitrary waveform generator in our laboratory makes it possible to push a custom-designed waveforms and using them in ultrasound applications.

The scan results of using the signal shown above with and without the skull are demonstrated in Figure 3.8. The hydrophone scans cover a distance of 20 mm

in the lateral direction with a resolution of 0.05 mm and a distance of 20 mm in the elevation direction with a resolution of 0.1 mm. The scanned plane of the skull was selected to be at bregma -2.5 mm, which corresponds to Plane 2 illustrated in Figure 3.4.

It is clear from Figure 3.8(a) that the multi-frequency waveform has achieved a high degree of acoustic energy localization at the DMUA geometric focus. Additionally, even after introducing the skull between the DMUA and the hydrophone tip, the acoustic energy at the geometric focus is still localized as depicted in Figure 3.8(b). However, the distortion associated with the skull is visible (e.g. spreading of acoustic energy around the focal point and increased sidelobe level).

Another signal was designed and used in performing planar hydrophone scans with and without the skull. The signal was composed of 3.7, 3.8, 3.9, 4.0, 4.1, 4.2, and 4.3 MHz narrowband pulses separated in the time domain as depicted in Figure 3.9. Intensity profiles were measured with and without the skull in a lateral-elevation plane corresponding to Plane 2 illustrated in Figure 3.4. As expected, high degree of acoustic energy localization with almost no distortion has been achieved through the plain water scan (Figure 3.10(a)). Figure 3.10(b) shows the measured transskull intensity profile for the multiple-frequency driving signal. The differences between this result and the result shown in Figure 3.8 are subtle, but demonstrate the effects of using higher frequency components. For example, lateral grating lobes are clearly visible at $\pm$9mm in Figure 3.9 (b).For both multiple-frequency driving signals, well-defined focal spots were formed despite the visible distortions due to the propagation of the FUS wavefront through the skull.

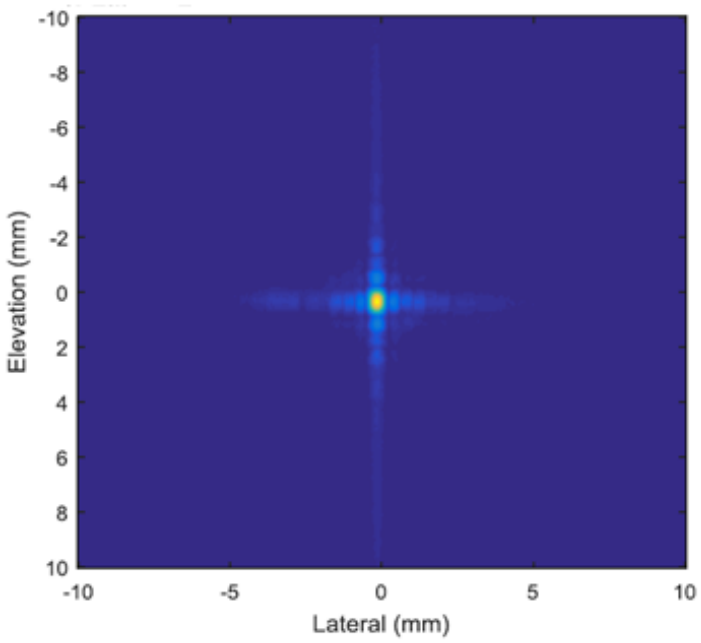

(a)

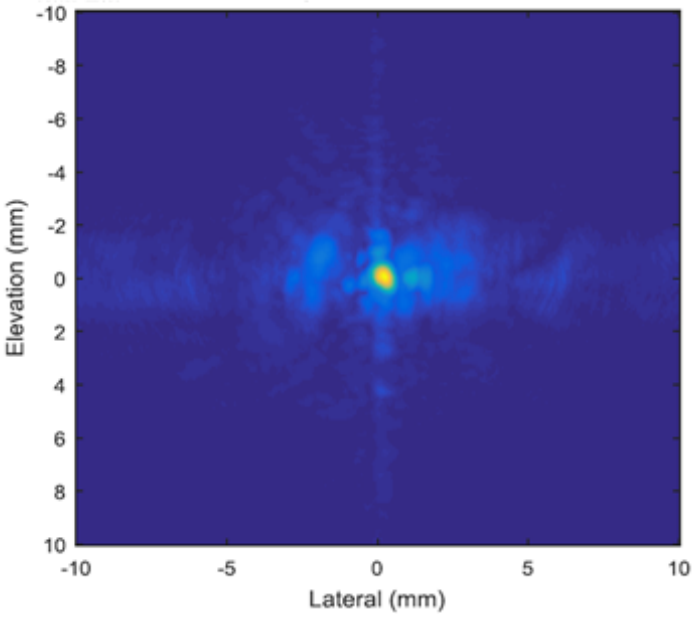

(b)

Figure 3.8: Ultrasound intensity profile measurements using a needle hydrophone: (a) Reference measurement without the skull; (b) Transskull measurement.

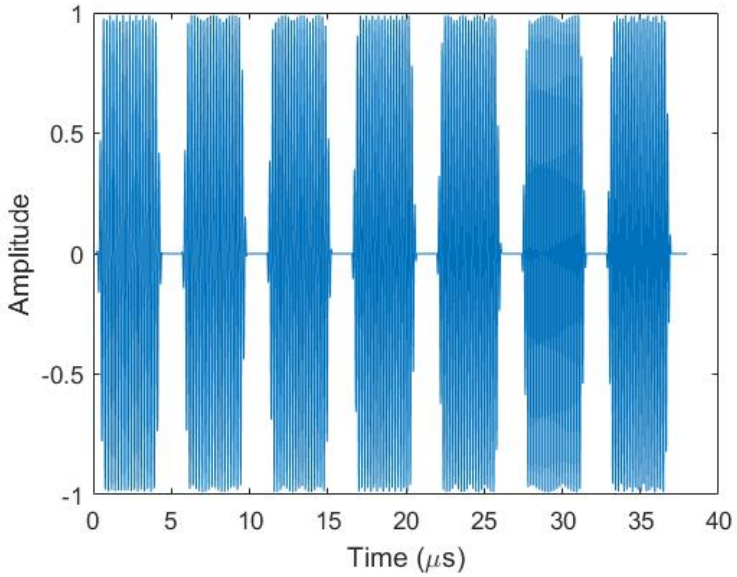

Figure 3.9: Signal composed of seven narrowband pulses centered at 3.7, 3.8, 3.9, 4.0, 4.1, 4.2, and 4.3 MHz.

3.3.4 Characterization of Focusing Gain Loss

Acoustic energy at five different points within the therapeutic operating field (ThxOF) of the DMUA have been recorded with and without the skull. At each point the hydrophone tip was positioned with the guidance of SA imaging mode and used to capture the ultrasound signals. For every point measurement, 20 frames of data sets were collected, averaged, and filtered. Figure 3.11 shows SA images of the hydrophone tip location at each selected point behind the skull. The locations were at the geometric focus of the DMUA (0 mm, 40 mm), two millimeter to the right of the geometric focus (2 mm, 40 mm), two millimeter to the left of the geometric focus (-2 mm, 40 mm), two millimeter form the geometric focus towards the DMUA apex (0 mm, 38 mm), and two millimeter form the geometric focus away from the DMUA apex (0 mm, 42 mm). The skull was placed approximately 32 mm from the apex of the DMUA. This location corresponds to our *in vivo* experiment set up described in [18]. In addition, skull was positioned in the

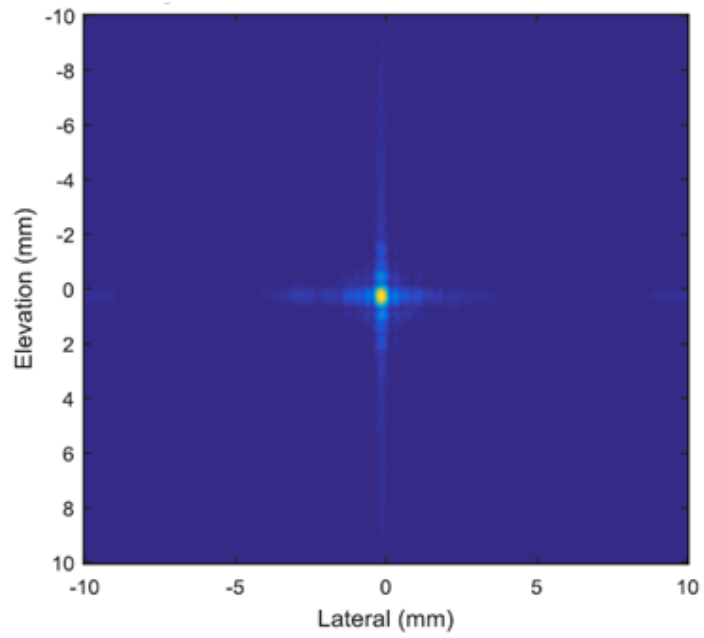

(a)

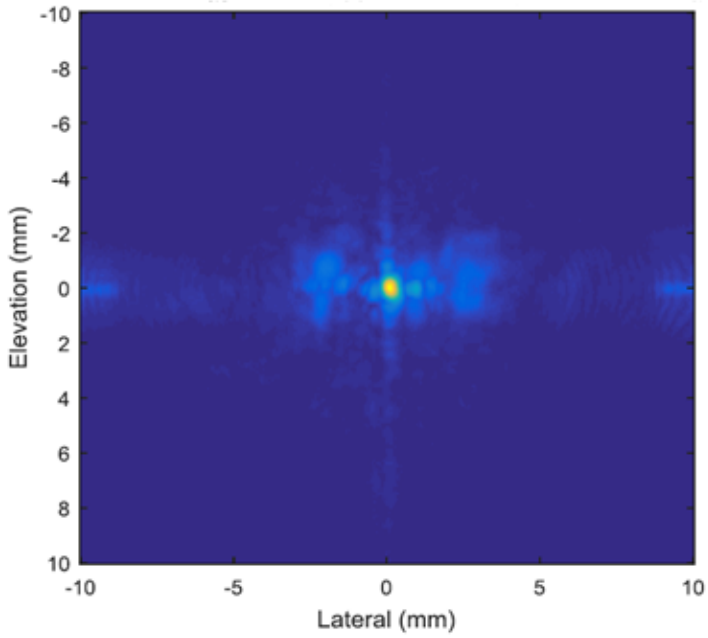

(b)

Figure 3.10: Ultrasound intensity profile measurements using a needle hydrophone: (a) Reference measurement without the skull; (b) Transskull measurement.

elevation direction such that the treatment plane (See Figure 3.4) is defined with respect to bregma. For this set of experiments, measurements were performed assuming the target focus is within the bregma -0.5mm and bregma -2.5mm planes.

Table 3.1 gives the transskull transmitted energy values in dB with reference to the water-only measurement using the needle hydrophone. These values represent the loss in focusing gain due to the through-skull propagation. Based on these measurements, one can see that the skull produces larger loss in focusing gain for the bregma -0.5mm treatment plane compared to the bregma -2.5mm plane. These results are typical and they demonstrate some important aspects of transcranial focusing:

1. For a fixed treatment plane and skull location, focusing gain depends on the target location within the plane.

2. For a fixed target location with respect to the transmitting array, focusing gain depends on the portion of the skull interacting with the FUS wavefront.

The measurements shown in Table 3.1

3.4 Conclusion

Hydrophone measurements of transskull FUS beam profiles were used to characterize the nature of spatial distortions with reference to water-only measurements. The measurements confirmed that the spatial heterogeneity of the skull as an obstacle degrade the measured beam profile and the focusing intensity gain at the target. Furthermore, this degradation is a function of the region of interaction between the skull and the FUS wavefront. The loss in focusing gain is more pronounced when the FUS wavefront interacts with thicker, nonuniform portions of the skull. For example, in the bregma -0.5mm case, the FUS wavefront goes through the thicker bone structure near the suture line, which results in $\approx$7 dB loss in intensity gain near the DMUA geometric center compared to $\approx$ 5.5 dB for the bregma -2.5mm case. In the latter case, the FUS wavefront interacts with

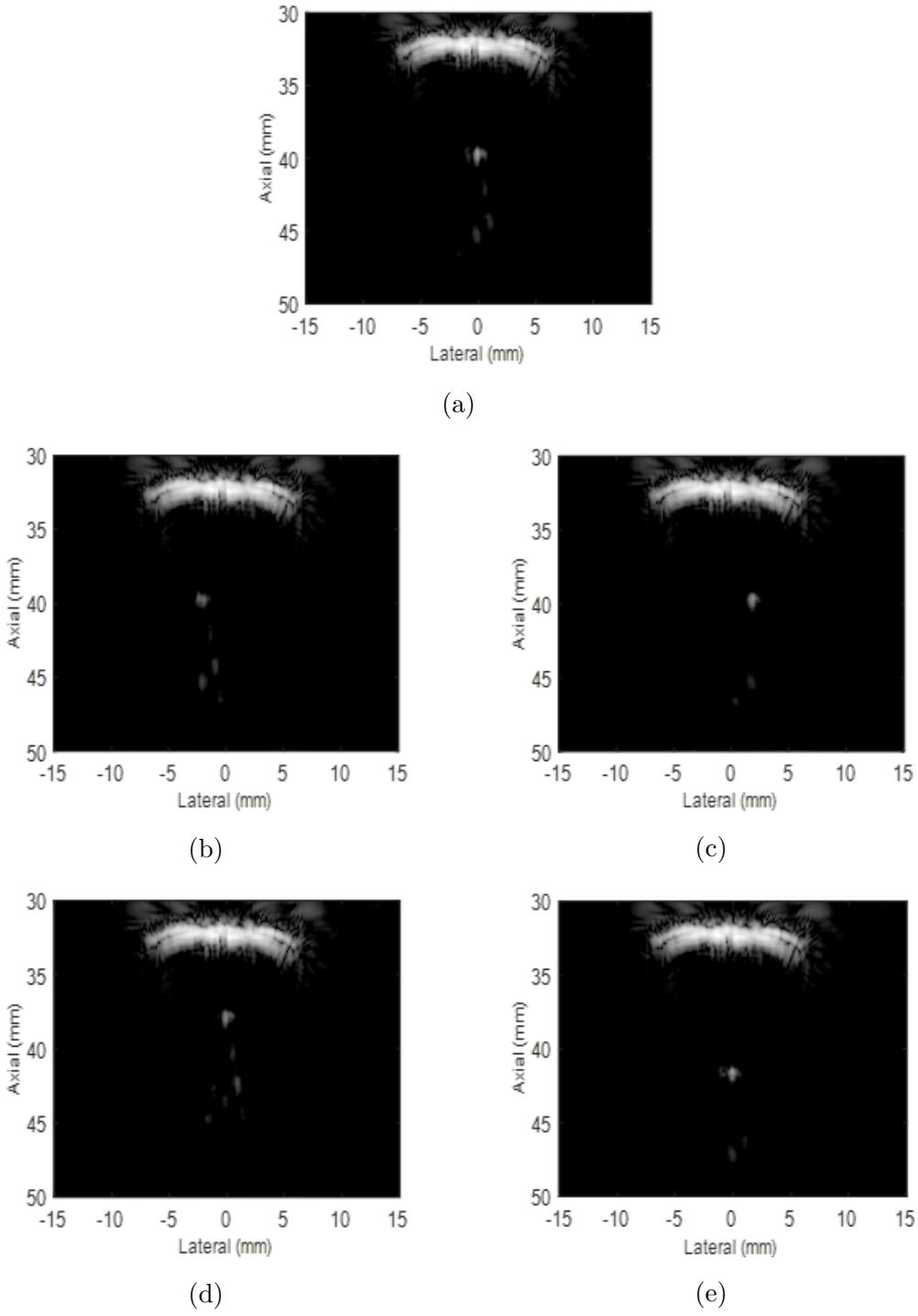

Figure 3.11: 40-dB grayscale SA images of the skull in front of a needle hydrophone in water tank at (a) the DMUA geometric center (0, 40), (b) (-2, 40), (c) (2, 40), (d) (0, 38), and (e) (0, 42) mm.

Table 3.1: Normalized transskull measurements of acoustic received energy values in two different treatment planes.

Hydrophone tip location (mm)	**Transskull Energy (dB) bregma -0.5mm**	**Transskull Energy (dB) bregma -2.5mm**
(0, 40)	-6.94	-6.08
(2, 40)	-7.07	-5.42
(-2, 40)	-6.70	-5.30
(0, 38)	-6.82	-3.47
(0, 42)	-4.02	-3.77

the parietal bone at it traverses the skull. This explains the lower levels of loss in focusing gain given in Table 3.1. In both cases, distortions were observed, but focusing was achieved albeit with reduction in focusing gain. This loss can be recovered, in part, by refocusing the transmitting array according to previously described methods [54, 37, 52].

The results shown herein are typical of numerous measurements performed since 2014 using *ex vivo* samples of the animal model used in our *in vivo* research [18]. They serve as the basis of the refocusing method described in the next chapter, which employs the following features of our DMUA system:

1. Three-dimensional SA imaging used to define target treatment plane (See Figure 3.4).

2. Two-dimensional SA imaging of the target plane is used to identify the target point(s) and any critical point(s), where FUS energy is to be minimized. This is an application of the refocusing algorithm described in [39] based on

the theoretical work described in [55].

3. Unlike the image-based refocusing method described in [39], the channel echo data acquired during SA imaging of the treatment plane is used to form focusing data matrix (FDM). The FDM is used in solving and eigenvalue problem to find the optimal driving vector. *The validation of the FDM approach to refocusing is the main contribution of this thesis research.*

4. STF imaging is used before and after refocusing to evaluate the relative focusing gain at the target(s) and incident energy at the critical point(s).

Chapter 4

Real-Time Image-Based Refocusing of tFUS Beams Using DMUAs

4.1 Introduction

Transcranial focused ultrasound (tFUS) is gaining wider acceptance in a range of therapeutic applications for the treatment of brain disorders. It represents a promising noninvasive modality for providing therapeutic ablative treatments as well as subtherapeutic (neuromodulation) treatments for brain conditions [22]. Advances in image guidance, especially using MRI, have impacted progress and led to increased interest in tFUS-based therapies ranging from ablation to neuromodulation.

The early efforts of targeting brain tissues using ultrasound were made with the skull removed. This was performed due to uncertainties bout ultrasound wave propagation through the complex structure of the skull. Skull-induced FUS aberration dilemma was first addressed by White et al. [56],[57] during their investigation of B- and C-scan images of brain tissues. This dilemma has hindered the progress of utilizing the tFUS beam in clinics.

Ultrasound beam distortions due to the presence of strongly scattering obstacles in the path of the wavefront have been studied by several investigators. This has led to the development of a variety of ultrasound aberration correction methods to minimize the distortion and achieve the highest possible focusing gain at targeted locations. Ebbini and coworkers [55] have introduced a two-step hybrid virtual array-ray (VAR) technique to optimally synthesize the high-intensity focused ultrasound (HIFU) beams through the ribcage. In addition, they provided example results that validated the VAR technique feasibility in directing the acoustic energy through the intercostals between the solid ribs and minimizing the exposure over the ribs. The VAR technique is composed of two steps: 1) introducing a virtual array along the intercostals to generate a pre-specified acoustic energy levels at a set of control points within the ribcage, and 2) designing the actual array that induces the virtual array while minimizing the direct incidence of ultrasound over the ribs. The array directivity vectors from the transducer elements to the selected control points at the intercostals and ribs were a key in formalizing the technique.

Another method for ultrasound aberration correction was proposed by Fink and coworkers [58]. They have proposed a time reversal method to focus ultrasound beams on a reflective target in an inhomogeneous medium. The method is based on the reciprocity principle of the wave equation. According to the principle, if an acoustic point source and an ultrasonic receiver are interchanged, the acoustic received field will not be changed. The group published several studies illustrating the use of the time reversal method along with experimental demonstrations. Some of the studies were based on an iterative scheme to refocus on the most reflective target in the ultrasound field [59]. Other studies were based on the decomposition of the time reversal operator, which is called the DORT method [60][1] . The DORT method is a selective detection refocusing method which can be used to refocus on any of the targets within the insonified medium (i.e. not necessarily the most reflective target in the medium). It is based on

[1] DORT is the French acronym for décomposition de l'opérateur de retournement temporel

the decomposition of the time reversal operator and finding the eigenvalue and eigenvector of every resolved scatterer of different reflectivity. The eigenvector of each different scatterer provides the phase profile of the ultrasonic array excitation vector to refocus at that scatterer. Furthermore, the group provided analytical and experimental results to refocus on one of two identical targets with symmetric spatial distribution with respect to the array. This was achieved by using a linear combination of the eigenvectors related to each target. The acoustic field generated in the plane of the two symmetric targets was refocused at one of the targets when the two eigenvectors were summed up and refocused on the other target when they were subtracted from each other.

Hynynen and coworkers [61, 62], [38] have carried out theoretical and experimental studies to investigate the feasibility of producing refocused ultrasound beams through the skull. The studies relied on the availability of pretreatment computed tomography (CT) and MRI imaging data of the skull to correct for ultrasound aberration. They used the data to extract the skull profile and model local acoustic properties of the treatment volume, including density, speed of sound, and ultrasound absorption. Then, they substituted the derived parameters in a theoretical model of wave propagation to calculate an appropriate phase distribution profile capable of refocusing the ultrasound beam.

Other groups have used customized silicone acoustic lenses to correct for skull-induced aberration. Aubry et al. [63] provided experimental results demonstrating the feasibility of correcting ultrasound aberration using a single-element transducer coupled with an optimized-thickness acoustic lens. The lens thickness was determined based on numerical modeling and simulation results of the targeted brain region. According to this method, every different location over the same skull requires a specific acoustic lens of tailored thickness. In addition, higher-amplitude transducer excitation signals are needed in order to compensate for the acoustic energy absorption due to the introduced lens.

The DMUA technology was introduced in the late 1990s [17] and its real-time implementation was described in [64]. Utilizing the DMUA imaging for guidance

and feedback, Ebbini et al. [39] have demonstrated an optimal refocusing algorithm in the context of transthoracic targeting of liver tumors. The optimization achieved specified intensity level(s) at target point(s) while minimizing the exposure to the ribs in the path of the focused wavefront. DMUA image guidance was used to identify the target point(s) and the ribs in the path of the beam. The DMUA imaging beamforming parameters were used to derive propagation operators, $\boldsymbol{H}_t$ and $\boldsymbol{H}_c$ from the DMUA to the target(s) and ribs, respectively. The ropagation operators were used to solve a constrained weighted optimization problem described in [55].

It should be noted that the image-based refocusing algorithm demonstrated in [39] accounted for the diffraction effects fully by incorporating the array element directivity at the target and critical point(s). However, the effects of the ribs as aberration were ignored. The main objective was to reshape the wavefront in order to minimize direct exposure to the ribs and direct the energy flow through the intercostals. That is, it was not an aberration correction algorithm.

In this chapter, we introduce a refocusing algorithm that utilizes the DMUA imaging guidance and feedback as was described in [39]. In particular, SA imaging is used to obtain the propagation operators $\boldsymbol{H}_t$ and $\boldsymbol{H}_c$ in the context of transcranial focusing. However, the new algorithm implements an important aberration correction component. This component is derived from SA pre-beamforming echo data by a forming focused data matrix (FDM) associated with each target or critical point. An eigenvalue decomposition of the FDM is used to obtain an aberration correction term to the beamforming-based array excitation vector needed to focus at the target or critical point associated with the matrix.

The experimental demonstration of the transcranial refocusing algorithm is the main contribution of this thesis research. We present *ex vivo* results demonstrating the feasibility of the refocusing algorithm to regain the focusing gain after penetration through skull samples. Our algorithm is anchored to the real-time imaging capabilities of DMUAs [64], which are one of the promising technologies for widespread use of tFUS. The algorithm exploits the availability of channel echo

data of the synthetic aperture (SA) imaging mode of the DMUA to calculate an improved estimate of propagation operators by solving eigenvalue decomposition problems. In addition, the algorithm benefits from some of the DMUAs advantages of operating in imaging and therapy modes in real-time. The excitation waveforms of the DMUA imaging and therapy modes of operation share the same parameters although with different duration and/or excitation levels. Therefore, it is possible to perform instantaneous feedback on tFUS-tissue interaction at a specific target volume in the brain as well as the intervening and surrounding tissues.

4.2 Mathematical Formulation

4.2.1 Optimal Multiple-Focus Synthesis

The proposed ultrasound refocusing algorithm builds on the concept of array pattern synthesis introduced in [65]. A continuous wave (CW) propagation operator $\boldsymbol{H}$ describing the transfer characteristics between an aperture and a finite set of control points was defined. When the aperture is discretized by using a set of array elements with arbitrary distribution, the propagation operator is reduced to a matrix operator of size $M \times N$, where M is the number of control points and N is the number of array elements. The complex pressures generated by the array elements at the control points are given by Equation 4.1

$$\boldsymbol{p} = \boldsymbol{H}\boldsymbol{u}, \tag{4.1}$$

where $\boldsymbol{u}$ is the complex array excitation vector. The propagation operator ($\boldsymbol{H}$) used in Equation 4.1 represents the basis for the synthesis problem. Its entries are estimated from the array transducer element directivities at the specified control points.

The operator $\boldsymbol{H}$ can be computed from a propagation model of the medium

between the aperture and the control points, for example, using the Rayleigh-Sommerfeld integral in a homogeneous, possibly absorbing half space. More sophisticated modeling was also used to compute $\boldsymbol{H}$ in the presence of strongly scattering targets [55]. Alternatively, the propagation operator matrix $\boldsymbol{H}$ could be directly measured using a hydrophone [54]. For instance, to measure the propagation operator matrix entry $h(m,n)$ (i.e. at control point m due to transducer element n), the hydrophone tip needs to be located at location m and record the complex pressure value produced by the element n when it is excited by a unit amplitude signal. This process needs to be repeated for all transducer elements ($n = 1, 2, \cdots, N$) while the hydrophone is sitting at the same location.

With the propagation operator in hand, an optimal solution to the pattern synthesis problem could be evaluated using a variety of mathematical methods. Obviously, Equation 4.1 provides a basis for a constrained optimization problem. Furthermore, in imaging and therapeutic applications of focused ultrasound, $M < N$ and Equation 4.1 has an infinite number of solutions (under determined system). In this case, the More-Penrose pseudoinverse provides the optimal minimum-norm least squares solution

$$\hat{\boldsymbol{u}} = \boldsymbol{H}^* \left(\boldsymbol{H}\boldsymbol{H}^*\right)^{-1} \boldsymbol{p}, \tag{4.2}$$

when $\boldsymbol{H}$ is full rank. Mathematically, the operator $\boldsymbol{H}^*$ is the adjoint ($(\cdot)^*$ is the Hermitian transpose). In [65], this operator was interpreted as a *backpropagation operator* from the control points to the discretized aperture. With this interpretation, the mathematical solution given in Equation (4.2) can be explained physically as a cascade of inverse filtering and backpropagation operations.

4.2.2 Focusing Gain

The focusing gain in terms of the optimal *pseudoinverse* solution is defined as

$$G_t = \frac{|\boldsymbol{p}|^2}{|\boldsymbol{u}|^2} = \frac{\boldsymbol{u}^*\boldsymbol{H}^*\boldsymbol{H}\boldsymbol{u}}{\boldsymbol{u}^*\boldsymbol{u}}, \tag{4.3}$$

where we have used Equation (4.1) to substitute for $\boldsymbol{p}$ in the numerator. The excitation vector that maximizes the *Rayleigh quotient* in Equation (4.3) is proportional to the *eigenvector* associated with maximum *eigenvalue* of the Hermitian matrix operator $\boldsymbol{H}^*\boldsymbol{H}$. Alternatively, in terms of the *singular value decomposition* of the propagation operator, the maximizing excitation vector is proportional to the right singular vector associated with the maximum singular value of $\boldsymbol{H}$.

In terms of the *pseudoinverse* solution, the focusing gain can be expressed as

$$G_t = \frac{|\boldsymbol{p}|^2}{|\boldsymbol{u}|^2} = \frac{\boldsymbol{p}^*\boldsymbol{p}}{\boldsymbol{p}^* \left(\boldsymbol{H}\boldsymbol{H}^*\right)^{-1} \boldsymbol{p}}. \tag{4.4}$$

This form was used in optimizing the focusing gain in cases where the moduli of the complex pressures were constrained while the phases could be arbitrarily chosen [66].

4.2.3 Transcranial Focusing

The entries of propagation operators can be computed using wave propagation theory [61, 65]. The (m, n) entry of the propagation operator matrix can be written as

$$h(m,n) = \frac{j\rho\omega}{2\pi} \int_{S_n} \frac{e^{-jk|r_m - \acute{r}_n|}}{|r_m - \acute{r}_n|} dS_n, \tag{4.5}$$

where $\rho, \omega, k, |r_m - \acute{r}_n|$, and S_n are the density of the medium, angular frequency, wavenumber ($k = \frac{2\pi}{\lambda}$), distance between the point m and the DMUA element n, and element surface area, respectively. However, the entries of $\boldsymbol{H}$ can also be obtained from the beamforming parameters utilized in SA or STF imaging modes. Figure 4.1 is a schematic diagram that shows some of propagation operator entries from the array transducer elements to critical points selected along the skull surface as well as to target points around the DMUA geometric center.

In order to synthesize an array excitation vector ($\boldsymbol{u}$) that is capable of controlling the acoustic pressure at target and critical points in the imaging field of view (IxFOV) of a DMUA, we exploit the availability of channel echo data to construct focused data matrices and hence update the propagation operators as follows:

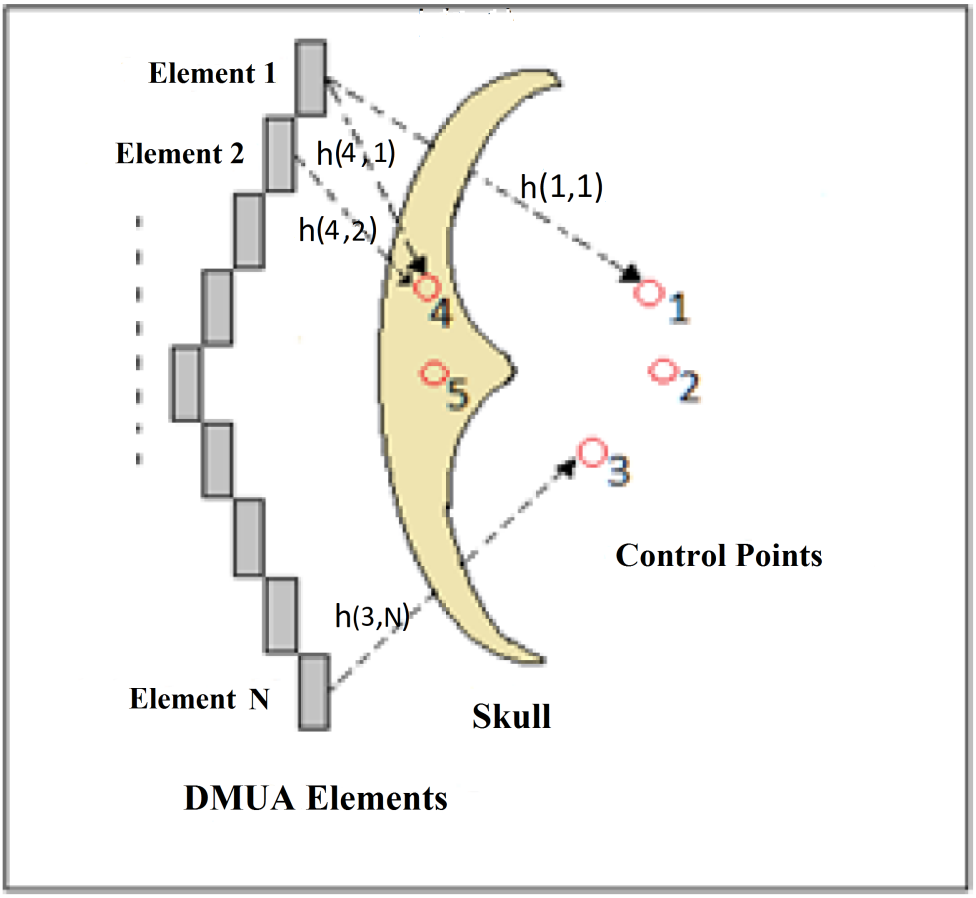

Figure 4.1: Schematic diagram depicting the location of critical points (4 and 5) as well as target points (1, 2, and 3).

Forming the Focused Data Matrix

For a given point at $\vec{r}_m$ in a DMUA IxFOV, a data matrix, $\boldsymbol{X}_{m,n}$, can be formed from channel data at a center frequency f_i according to the procedure outlined in Algorithm 1. In this procedure, we extract the RF echo data which contribute to the creation of the point in the image. Afterwords, we specify a region of interest (RoI) around the extracted data, such that the radius of the RoI (R) is larger than the expected range of variation in echo arrival time due to skull aberration. The operator $\mathcal{F}_{f_i}\{\cdot\}$ represents a set of narrow band (NB) filters with center frequencies at $\{f_i\}_{i=1}^{N_f}$. The quantities inside the $\lceil\cdot\rceil$ are given in *samples*, so that $\boldsymbol{X}_{m,n}$ is $L \times N$ matrix with L typically in 50 - 100 range. F_s and c are the sampling frequency and medium speed of sound, respectively.

Algorithm 1 Focused Data Matrix, $\boldsymbol{X}_{m,n}$

1: **procedure** DEFINING FOCUSED DATA MATRIX(DMUA Lattice and RF echo from SA(f_i), RoI $\vec{r}_m$& R,$\boldsymbol{X}_{m,n}$)

2: Define RoI $\{\vec{r} : |\vec{r} - \vec{r}_m| < R\}$

3: **for all** N DMUA elements $n = 1, 2, \cdots, N$ **do**

4: Determine $R_{m,n} = |\vec{r}_n - \vec{r}_m|$ and $R_{m,n}^{\{min,max\}} = R_{m,n} \mp R$

$$\boldsymbol{X}_{m,n}(:, f_i, n) = \mathcal{F}_{f_i}\left\{RF_n\left(\left\lceil\frac{2 \times R_{m,n}^{min} \times F_s}{c}\right\rceil : \left\lceil\frac{2 \times R_{m,n}^{max} \times F_s}{c}\right\rceil\right)\right\} \quad (4.6)$$

where $\mathcal{F}_{f_i}\{\cdot\}$ is a NB filter centered at f_i and $\lceil\cdot\rceil$ is the ceiling quantizer.

5: **end for**

6: **end procedure**

Algorithm 1 can be described visually as demonstrated in Figures 4.2 to 4.4 . Figure 4.2 shows an SA image of a rat skull introduced between the DMUA and a hydrophone tip in a degassed/deionized water tank. The rat skull was located at about 32 mm distance from the DMUA apex and the hydrophone tip at the geometric center of the DMUA (40 mm from the DMUA apex). Two control points were selected, a critical point along the medial suture line of the skull and a target

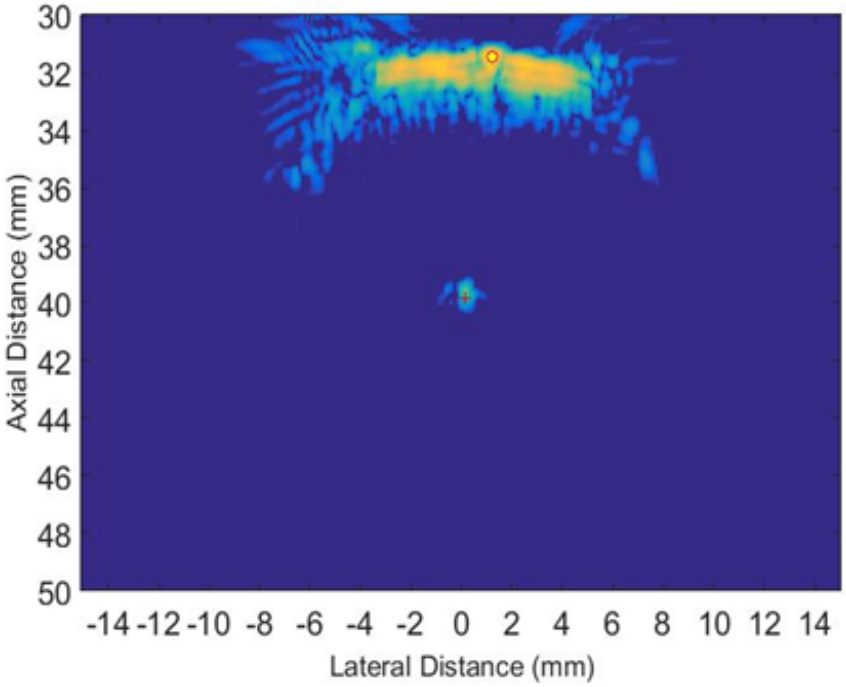

Figure 4.2: SA image of a rat skull in front of a hydrophone tip.

point at the hydrophone tip. To form the focused data matrix (FDM) of every point, we first obtained the pre-beamformed RF data of the created image from the DMUA system. Then, for each selected point we extracted the pre-beamformed RF data which contributes in creation of the point in the beamformed image. This extraction process of every point is demonstrated in Figures 4.3(a) and 4.3(b) for the critical and target points, respectively. Since the DMUA driver that we have in our laboratory is composed of 32 active channels, 32 signals were received due to each element transmission. As a result, each point in the beamformed image was composed from 32×32 RF echo data samples.

The curvature nature in the RF echo data in Figure 4.3(a) is due to the fact that each transducer element of the phased array was at a different distance from the selected point on the skull. Therefore, each transducer element received the RF echo signal from the point at a different time instant. Figure 4.3(b) shows

the RF echo data which contributed in creation of the target point selected at the hydrophone tip that was located at the DMUA geometric center. This RF echo data were supposed to arrive at all DMUA transducer elements at the same time. However, due to the presence of the skull and its aberration, there are slight variations in echo arrival time at each transducer element.

After extracting the RF echo data of selected control points, we specify a region of interest (RoI) around these data points as outlined in Algorithm 1. The RoI data are determined as

$$R_{m,n}^{\{min,max\}} = R_{m,n} \mp R, \tag{4.7}$$

where $R_{m,n}$ is the distance between the selected point m and each DMUA transducer element n $(n = 1, 2, ..., N)$ and R is the radius of the region of interest which should be larger than the expected range of variation in echo arrival time due to skull aberration.

Afterwards, we extract the RF echo data that belong to the specified RoI around each control point. This data would form a matrix of $2R+1$ rows and N^2 columns. Figure 4.4(a)and Figure 4.4(b) show the RoI RF echo data extracted for the selected control point (critical point) on the skull medial suture line and the selected control point (target point) at the hydrophone tip.

With the RoI data in hand, the focused data matrices (FDMs) can be easily extracted. Each group of 32 columns of the RoI data matrix forms a focused data matrix of each transmit. In particular, the first 32 columns of the RoI data matrix represent the FDM of the first transmit $(n = 1)$ and the second 32 columns of the RoI data matrix represent the FDM of the second transmit $(n = 2)$, and so on until the last 32 columns of the RoI data matrix which form the FDM of the last transmit $(n = N)$.

For every formed focused data matrix $(X_{m,n})$ from SA imaging data, we construct a gramian matrix (S), and then we perform an eigenvalue decomposition in

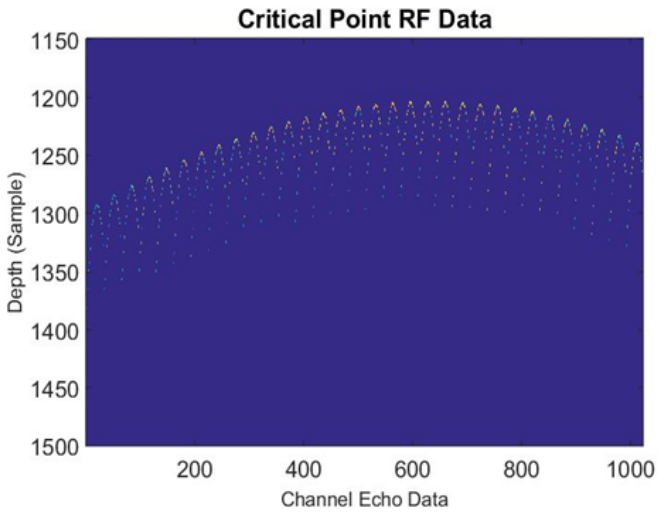

(a)

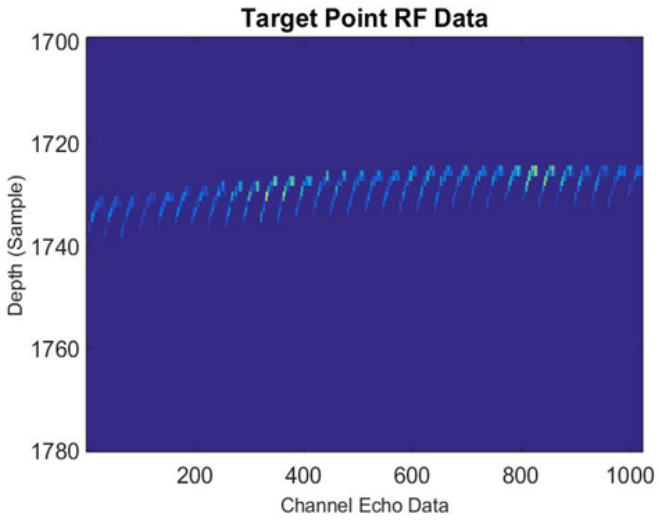

(b)

Figure 4.3: RF echo data of (a) the point selected on the skull (critical point) and (b) the point selected on the hydrophone (target point).

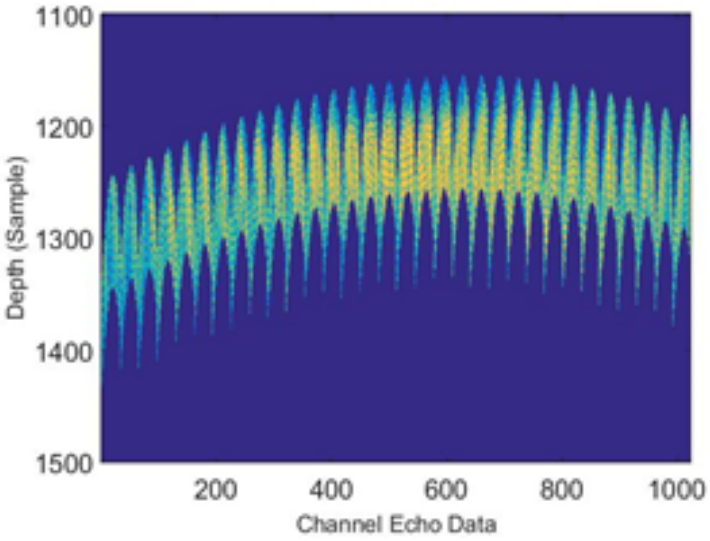

(a)

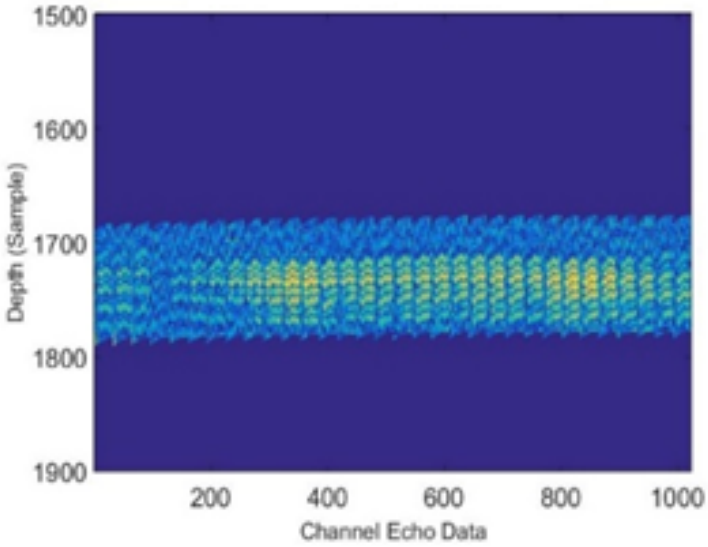

(b)

Figure 4.4: RoI RF echo data of (a) the point selected on the skull (critical point) and (b) the point selected on the hydrophone tip (target point).

order to find the eigenvalues and eigenvectors of the constructed matrix as follows:

$$\boldsymbol{S} = \boldsymbol{X}^{*}_{m,n}\boldsymbol{X}_{m,n}, \tag{4.8}$$

$$\boldsymbol{S} = \boldsymbol{E}\boldsymbol{\Lambda}\boldsymbol{E}^{-1}, \tag{4.9}$$

where $(\cdot)^*$ is the Hermitian transpose of a matrix. The eigenvectors ($\boldsymbol{E}$) and the eigenvalues ($\boldsymbol{\Lambda}$) are as follows:

$$\boldsymbol{E} = [\boldsymbol{e}_1, \boldsymbol{e}_2, \cdots, \boldsymbol{e}_N],$$

$$\boldsymbol{\Lambda} = \begin{pmatrix} \lambda_1 & 0 & \dots & 0 \\ 0 & \lambda_2 & 0 & \\ \vdots & \vdots & \ddots & \vdots \\ 0 & 0 & \dots & \lambda_N \end{pmatrix}_{N\times N} . \tag{4.10}$$

Then, we find the appropriate eigenvalues and eigenvectors to update the propagation operators. In particular, for a given control point, we use the maximum eigenvalue of every channel data matrix and the eigenvector related to the maximum among the maximum eigenvalues of the channel data matrices to update the array propagation operator at that point. The array directivity vector from all N DMUA elements to a specific control point ($\vec{r}$) before modification is defined as:

$$\boldsymbol{h}(\vec{r}) = \big[h_1(\vec{r}), h_2(\vec{r}), \cdots, h_N(\vec{r})\big], \tag{4.11}$$

which after modifications becomes as follows:

$$\boldsymbol{h}(\vec{r}) = \big[h_1(\vec{r})\lambda_1\angle e_1, h_2(\vec{r})\lambda_2\angle e_2, \cdots, h_N(\vec{r})\lambda_N\angle e_N\big]. \tag{4.12}$$

When tFUS beams refocus toward multiple points, the propagation operators become matrices instead of vectors. For T target points and C critical points, the

operators are constructed as follows [55]:

$$\begin{aligned}\boldsymbol{H}_t &= \begin{pmatrix} \boldsymbol{h}_1 \\ \boldsymbol{h}_2 \\ \vdots \\ \boldsymbol{h}_T \end{pmatrix} \\ &= \begin{pmatrix} h_1(\vec{r}_t(1)) & h_2(\vec{r}_t(1)) & \dots & h_N(\vec{r}_t(1)) \\ h_1(\vec{r}_t(2)) & h_2(\vec{r}_t(2)) & \dots & h_N(\vec{r}_t(2)) \\ \vdots & \vdots & \ddots & \vdots \\ h_1(\vec{r}_t(T)) & h_2(\vec{r}_t(T)) & \dots & h_N(\vec{r}_t(T)) \end{pmatrix}_{T\times N},\end{aligned} \tag{4.13}$$

$$\begin{aligned}\boldsymbol{H}_c &= \begin{pmatrix} \boldsymbol{h}_1 \\ \boldsymbol{h}_2 \\ \vdots \\ \boldsymbol{h}_C \end{pmatrix} \\ &= \begin{pmatrix} h_1(\vec{r}_c(1)) & h_2(\vec{r}_c(1)) & \dots & h_N(\vec{r}_c(1)) \\ h_1(\vec{r}_c(2)) & h_2(\vec{r}_c(2)) & \dots & h_N(\vec{r}_c(2)) \\ \vdots & \vdots & \ddots & \vdots \\ h_1(\vec{r}_c(C)) & h_2(\vec{r}_c(C)) & \dots & h_N(\vec{r}_c(C)) \end{pmatrix}_{C\times N}.\end{aligned} \tag{4.14}$$

By substituting the modified propagation operators, $\boldsymbol{H}_t$ and $\boldsymbol{H}_c$, in the optimization problem for refocusing [55, 39] formulated as

$$\begin{aligned} &minimize && ||\boldsymbol{H}_c\boldsymbol{u}||^2 \\ &subject\,to && \boldsymbol{H}_t\boldsymbol{u} = \boldsymbol{p}_t, \end{aligned} \tag{4.15}$$

and using the weighted minimum-norm least squares method to solve the problem, we get an optimal refocused array excitation vector ($\boldsymbol{u}_{opt}$) as follows:

$$\boldsymbol{u}_{opt} = \boldsymbol{W}_c^{-1}\boldsymbol{H}_t^*(\boldsymbol{H}_t\boldsymbol{W}_c^{-1}\boldsymbol{H}_t^*)^{-1}\boldsymbol{p}_t, \tag{4.16}$$

where

$$\boldsymbol{W}_c = (\boldsymbol{H}_c^* \boldsymbol{H}_c + \gamma \boldsymbol{I}) \tag{4.17}$$

is an invertible weighting matrix and γ is a regularization parameter. The vector $\boldsymbol{p}_t$ is the specified complex pressure at the target point(s). The optimal refocused array excitation vector ($\boldsymbol{u}_{opt}$) is capable of improving the focusing gain of tFUS beam at control locations by reducing the incident power at the critical point(s) while maintaining or increasing the exposure level at the target point(s).

The refocusing algorithm runs automatically once the user specifies the target and critical points. It is implemented on a software-defined ultrasound (SDUS) architecture allowing for real-time computation of the refocused excitation vector and immediate download to the driver within milliseconds. The real time operation has a major advantage of precise interrogation of the tissue response to the tFUS application. These tissue responses might appear in many different forms including tissue heating, cavitation, and boiling within a time of tens of microseconds.

4.3 Material and Methods

4.3.1 DMUA System

The DMUA prototype (64 element, concave with 40-mm radius of curvature) described in Section 2.2 was used to implement the image-based refocusing algorithm experimentally. In addition, it was used to image and generate therapeutic focused ultrasound beams through rodent skull samples *ex vivo*. Two imaging modes of the DMUA system were used during the experiments along with the 3D volume scan imaging. The SA imaging mode which provides a large field of view was utilized to guide the selection of the target and critical points used by the refocusing algorithm. In addition, RF echo data of SA imaging received by each array element were used to form the focused data matrices corresponding to the selected points. The STF imaging mode was used to characterize the tFUS

beam interaction with the skull and tissues in its propagation path. This was possible because of the inherent registration between the therapeutic and imaging coordinate systems of the DMUA. Finally, the 3D volume scan images were used to resolve the dorsal aspect, including bregma, lambda and medial suture lines, of the utilized skull. This allows for an accurate placement of the DMUA focal spot at the intended target behind the skull in a repeatedly manner.

4.3.2 Target Volume

We designed two different types of experiments to validate the feasibility of the refocusing algorithm as follows:

- Water Tank Experiments: Water tank measurements were performed to characterize the performance of the refocusing algorithm using the DMUA system. In some experiments, we used the needle hydrophone as an imaging target in addition to its main function of measuring the acoustic signal from SA and STF transmissions with and without the skull sample. In other experiments, we used a cone of ultrasound power meter device (Model UPM-DT 100AV, Ohmic Instruments Inc.) as an imaging target. The cone tip was located at and around the geometric center of the DMUA using SA imaging guidance. Afterwards, a rodent skull sample (rat skull) was inserted between the DMUA surface and the cone tip as demonstrated in Figure 4.5(a). The critical point was defined along the medial suture line of the skull since it represents the strongest reflector over the skull surface, while the target point was defined at the tip of the cone.

- Tissue-mimicking Phantom Experiments: We embedded rodent skull samples in a tissue-mimicking phantom to validate the feasibility of the image-based refocusing algorithm. The phantom was fabricated from graphite, gelatin, propanol, glutaraldehyde, and water, as described in [67, 68]. The embedded skulls were positioned at a distance of approximately 32 mm from the apex of the DMUA (corresponding to the skull position during *in vivo*

experiments). A thermocouple was inserted so that its junction was closest to the geometric focus and used as a point target in the imaging field of view (IxFOV) of the DMUA. A data acquisition unit (34970A, Agilent, Santa Clara, CA) was set at a rate of 100 Hz to acquire the thermocouple measurements. Figure 4.5(b) shows a schematic diagram of the experimental setup. The advantage of using the tissue-mimicking phantom is that it provides a realistic propagation medium corresponding to the small animal *in vivo* work being conducted. In addition, it provides an absorbing medium which can be used to characterize the heating efficiency of the tFUS beams with and without refocusing.

4.3.3 Assessment of Focusing Gain

To demonstrate improvement in ultrasound focusing gain due to refocusing, we have analyzed the changes in echogenicity at selected critical and target points when insonifying the medium using geometric and refocused ultrasound beams. In addition, direct temperature measurements have been recorded as another form of validation.

- Relative Echogenicity Change: The change in echogenicity value at and around selected control points (target and critical points) upon refocusing is a sign of change in power exposure level due to the tFUS beam application. The reduction of echogenicity at a critical point provides feedback on the decreased power deposition at the point, while the increase in echogenicity at a target point means an increase in power deposition at the target. One can see the changes in echogenicity around the target and critical points directly from the generated STF images with and without refocusing. This will be demonstrated in the results section.

- Temperature Measurement Using Needle Thermocouple: A 0.2-mm T-type copper-constantan thermocouple (Omega, Stamford, CT) is used to measure the temperature at the target location before, during, and after tFUS

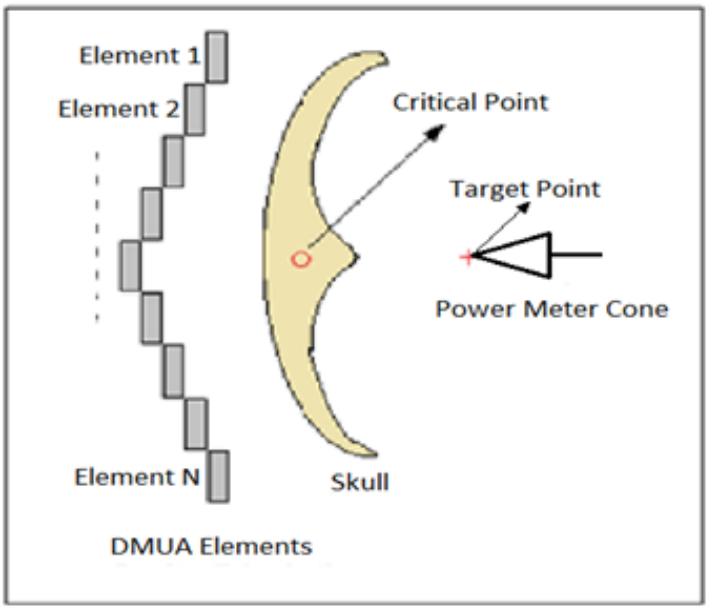

(a)

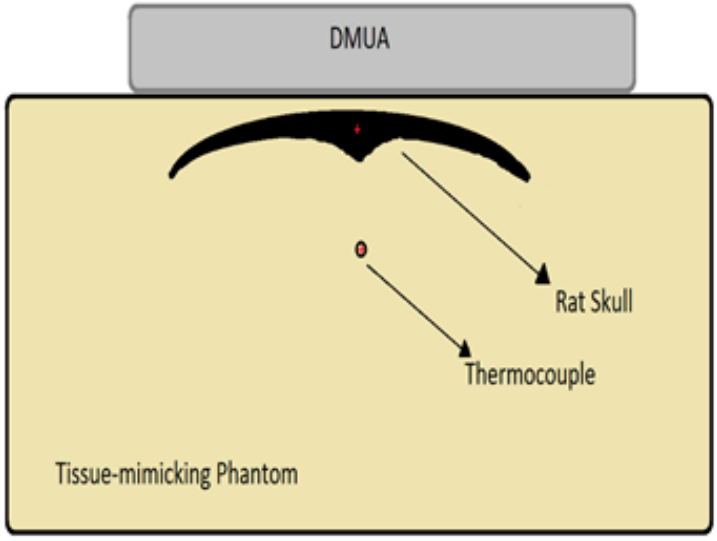

(b)

Figure 4.5: Schematic diagrams showing the experimental setups used to validate the refocusing algorithm in (a) deionized/degassed water tank and (b) tissue-mimicking phantom.

application. The measurements been have taken for both the geometric and refocused driving tFUS patterns at a rate of 100 Hz. Every time we made the measurements, we found that the temperature rise due to the application of the refocused ultrasound beam is higher than the temperature rise due to the geometrically focused beam, which is an indication of focusing gain improvement upon applying the refocusing algorithm. In addition, heat rates due to applying the tFUS beams have been calculated to show the improvement due to refocusing. The calculations have been performed by averaging the measured temeperature profiles and computing the time derivative of the averaged values [69].

4.4 Results

We present the findings of experimental studies to validate the capability of the real-time image-based refocusing algorithm to improve the ultrasound intensity at specified control points. This section mainly addresses the following aspects of the carried *ex vivo* experiments. The first is the DMUA imaging capability for generating two- and three-dimensional images to identify the dorsal aspect of the skull. This capability was extremely helpful in guiding and monitoring the tFUS application as well as selecting the appropriate imaging slice over the skull to position the DMUA and deliver the ultrasound beams. The second is demonstrating the improvement in focusing gain as a result of refocusing in imaging and therapy modes. The improvement is shown in imaging by monitoring the echogenicity at and around the control points and in therapy by direct measurements of the temperature profiles before, during, and after applying the tFUS beams.

4.4.1 Water Tank Experiments

In these experiments, we validated the improvements in focusing gain due to refocusing in terms of echogenicity. First, we located the cone tip of a power meter

device at the geometric center of the DMUA with the help of SA imaging guidance, and then a rat skull was inserted between the DMUA and the cone tip. Afterwards, a 3D volume scan of the skull was performed in order to identify important landmarks over the skull surface, including suture lines. Two planes across the skull were selected, one at bregma -0.5 mm and the other at bregma -2.5 mm. Figure 4.6 shows an SA image of the bregma -0.5 mm plane. The image was used for target and critical point selections. The target point was selected at the cone tip, while the critical point was at the medial suture line of the skull. The target point in this particular experiment was at (1, 39) mm from the apex of the DMUA and the critical point was at (1, 31) mm. The RF echo data of the image were used in the developed refocusing algorithm in order to generate a refocused ultrasound beam. Both the geometrically focused and the refocused ultrasound beams were used in the STF imaging mode of the DMUA. The generated 45 dB-grayscale STF images, with and without refocusing, validated the improvement in focusing gain at the target and critical locations in terms of echogenicity as demonstrated in Figure 4.7. From the figure, it is clear that the echogenicity at the target point was increased while it was decreased at the critical point. Figure 4.8 shows the echogenicity values in dB along an axial lines pass through the critical and target points. The red line is the echogenicity values from the STF image (Figure 4.7(a)) produced using the geometrically focused (standard focused) beam, while the blue one is the echogenicity values from the STF image (Figure 4.7(b)) produced using the refocused beam. Table 4.1 lists the average echogenicity values in dB of a 1 $\times$ 1 mm^2 areas around the target and critical points from STF images generated with and without refocusing. One can see that the refocused ultrasound beam has reduced the average echogenicity around the critical point by 7dB. This is a clear indication of reducing the acoustic power exposure level at the critical location due to refocusing. On the other hand, the average echogenicity around the target point has increased by 2.3 dB, which is also an indication of increasing the acoustic power deposition at the target point due to refocusing.

For the bregam -2.5 mm plane, we repeated the same approach of using SA

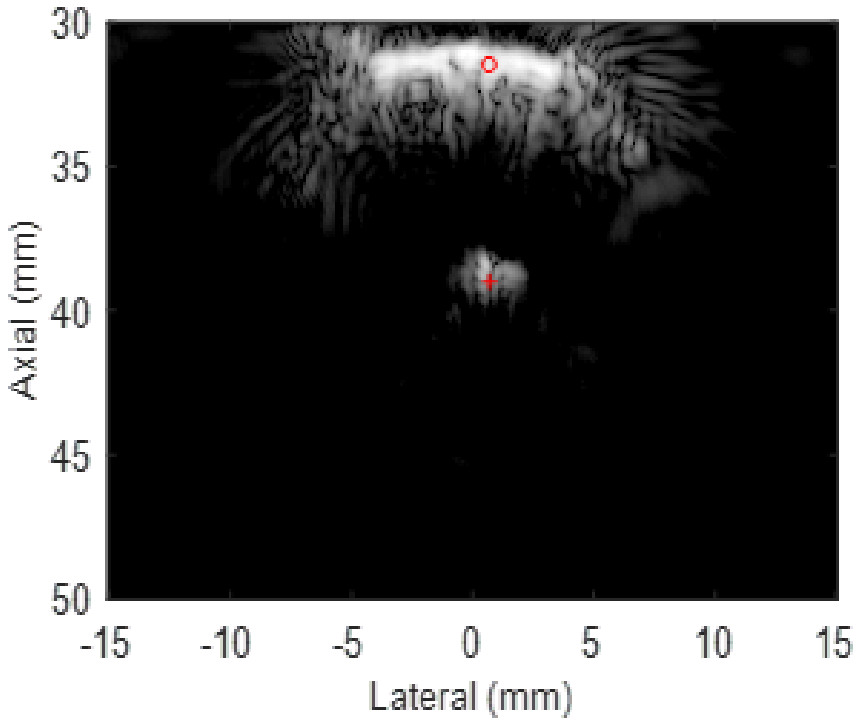

Figure 4.6: 45-dB grayscale SA image of the experiment setup in a degassed/ deionized water tank.

Table 4.1: Average echogenicity values around target and critical points with and without refocusing.

Control point	Standard STF average echogenicity (dB)	Refocused STF average echogenicity (dB)
Target point	-21.5	-19.2
Critical point	-5.5	-12.5

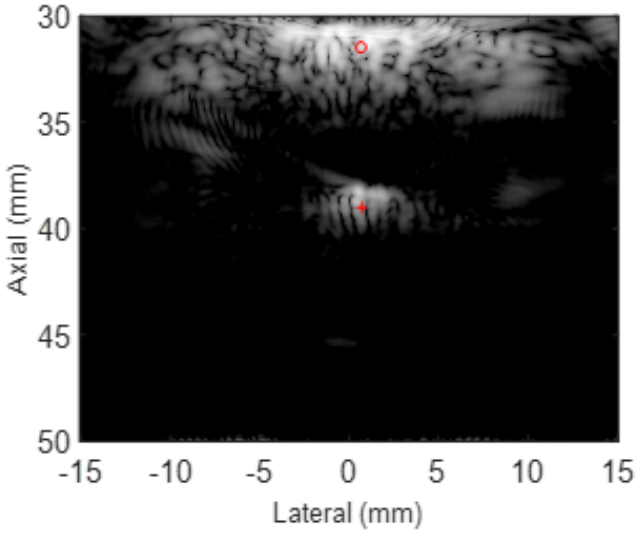

(a)

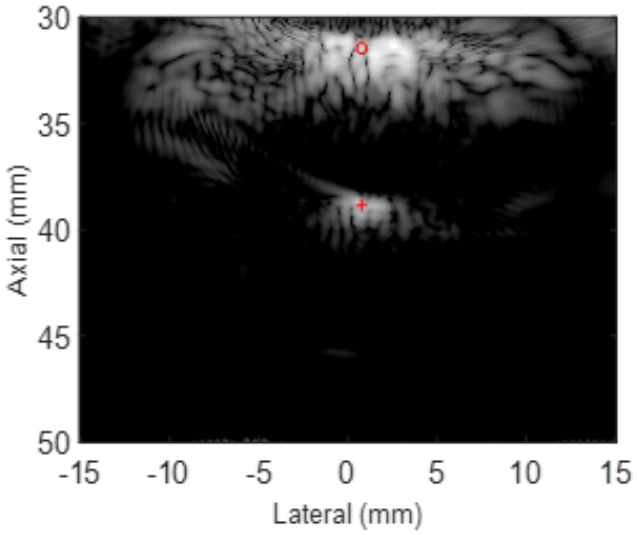

(b)

Figure 4.7: 45-dB grayscale STF images using: (a) geometrically focused and (b) optimally refocused DMUA excitation vectors.

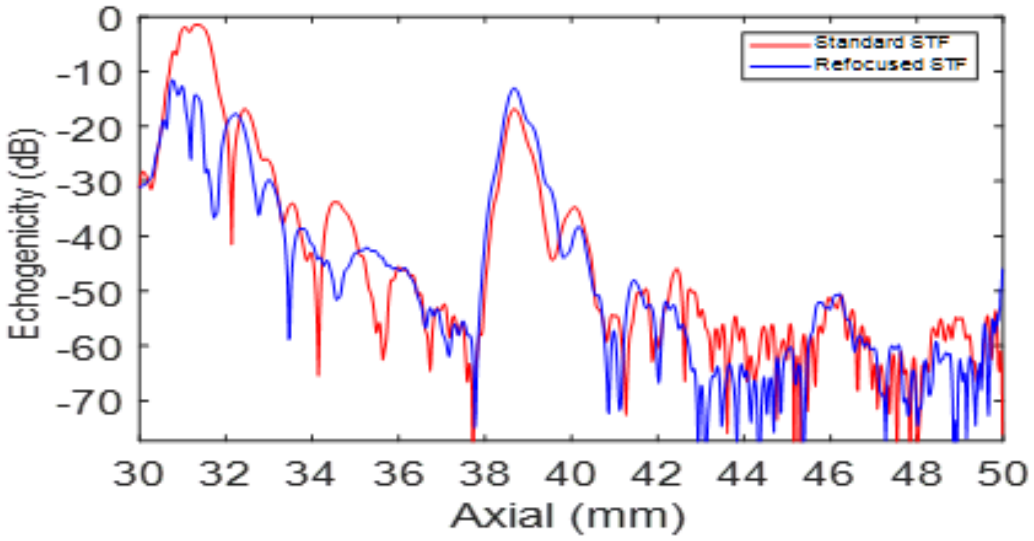

Figure 4.8: Echogenicity values of axial lines pass through the critical and target with and without refocusing.

imaging for guidance and computing a refocused array excitation vector. In addition, the refocused array excitation vector along with the geometrically focused (standard focused) vector were used to produce STF images and characterize the improvement due to refocusing. The target point was located at (0, 39) mm and the critical point at (0, 31.5) mm from the apex of the DMUA as demonstrated in Figure 4.9. The results of improved echogenicity at and around the target and critical points are demonstrated in Figures 4.10 and 4.11. The average echogenicity values around the target and critical points are listed in Table 4.2. As expected, the use of the refocused vector reduced the average echogenicity value around the critical point and increased it around the target point.

For the same skull plane (i.e. bregma -2.5 mm), we repeated the experiment; however, we changed the location of the target and critical points. The target point was selected to be at (1, 40) mm, while the critical point was at (0, 31.8) mm from the apex of the DMUA. The generated grayscale images are not shown here for the sake of avoiding repetition. Figure 4.12 shows the echogenicity line

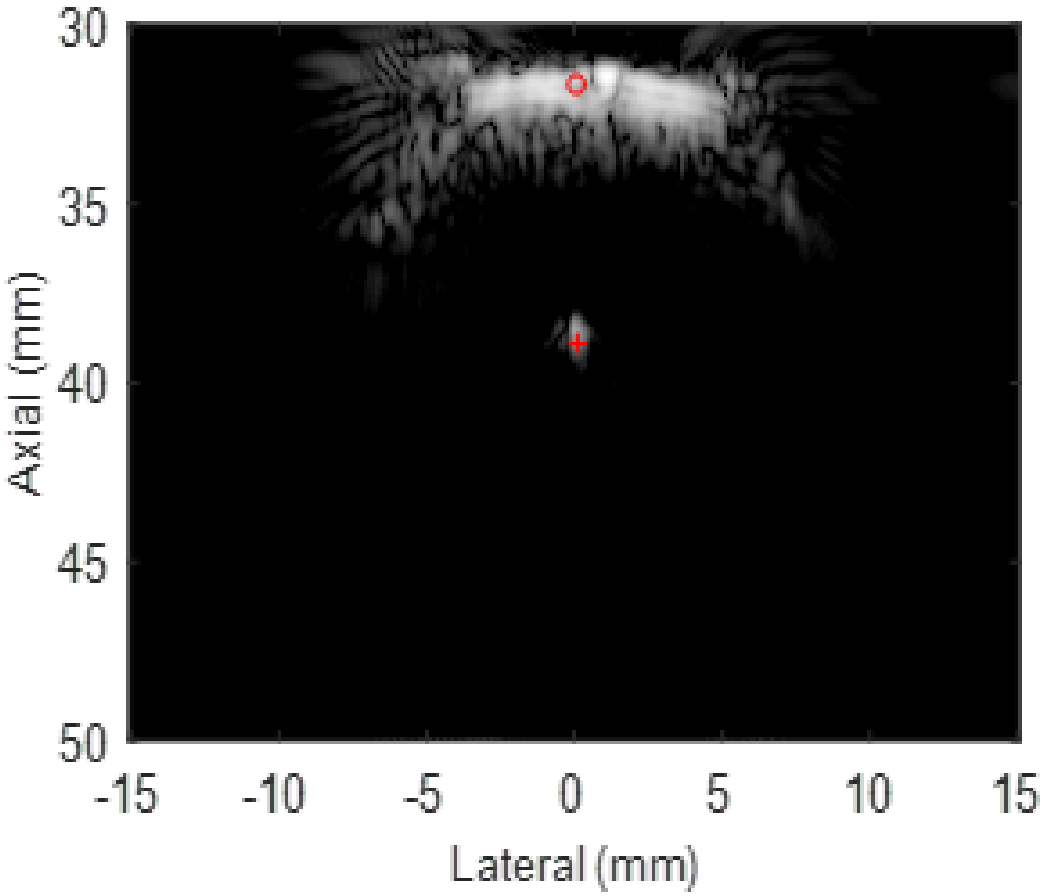

Figure 4.9: 45-dB grayscale SA image of the experiment setup in a degassed/ deionized water tank.

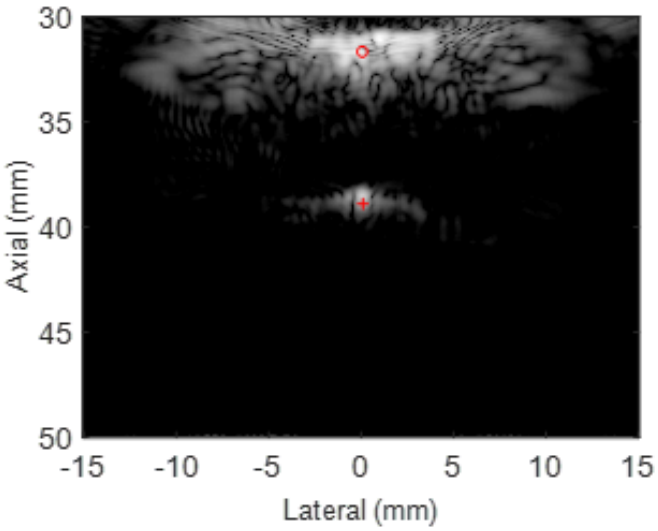

(a)

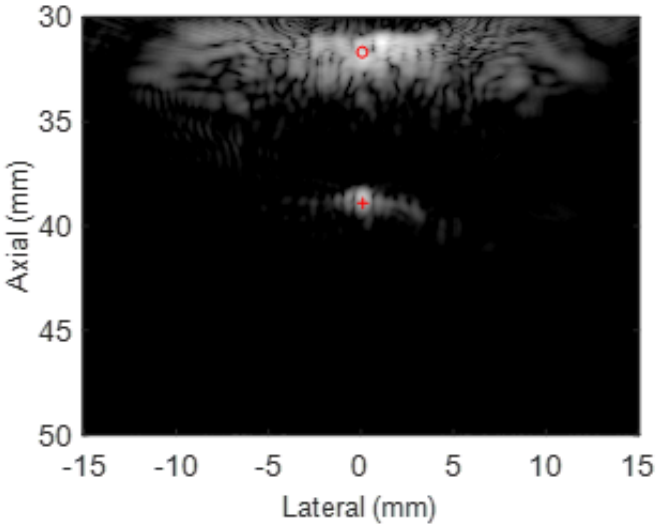

(b)

Figure 4.10: 45-dB grayscale STF images using: (a) geometrically focused and (b) optimally refocused DMUA excitation vectors.

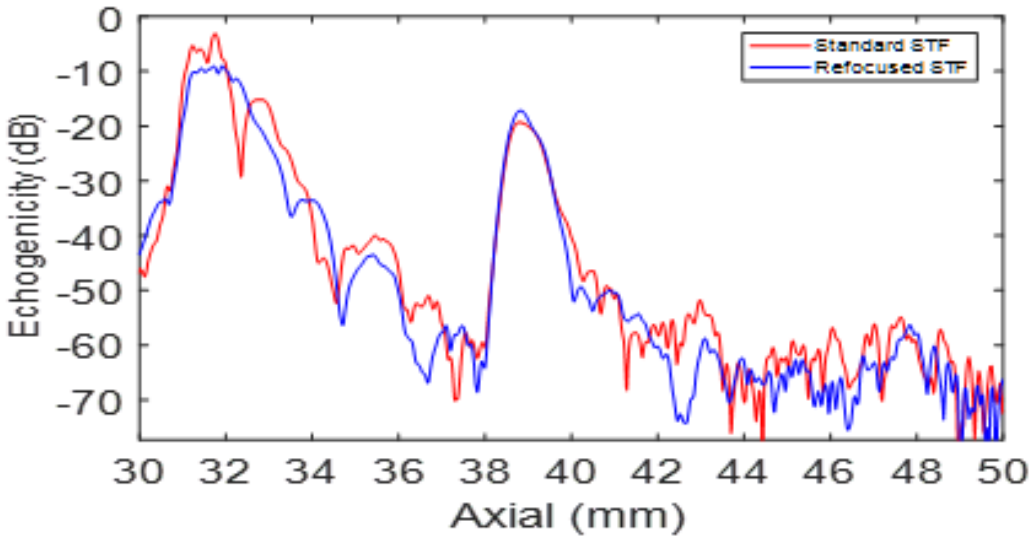

Figure 4.11: Echogenicity values of axial lines passing through the critical and target with and without refocusing.

Table 4.2: Average echogenicity values around target and critical points with and without refocusing.

Control point	Standard STF average echogenicity (dB)	Refocused STF average echogenicity (dB)
Target point	-23.3	-21.2
Critical point	-10.2	-11.6

Table 4.3: Average echogenicity values around target and critical points with and without refocusing.

Control point	Standard STF average echogenicity (dB)	Refocused STF average echogenicity (dB)
Target point	-32.1	-23.1
Critical point	-11.3	-14.9

plots in dB along segments of axial lines passing through the critical and target points with and without refocusing. Again, it is clear from the figure that the echogenicity has increased at the target point and decreased at the critical point due to refocusing. Table 4.3 summarizes the average echogenicity values of 1×1 mm^2 areas around the target and critical points with and without refocusing.

4.4.2 Tissue-Mimicking Phantom Experiments

These experiments were designed to characterize the improvement in focusing gain in terms of heating rate and echogenicity due to refocusing. Temperature profiles resulting from the application of therapeutic tFUS beams for a duration of 10 seconds with and without refocusing were measured. In addition, heating rates were used as a comparison criterion to show the validity of the refocusing algorithm in improving the focusing gain at selected control points. We started the experiments by first generating 3D volume scan images of the embedded skull in the phantom and then selecting various positions of image slices with respect to markers on the skull, including the bregma, lambda, and medial suture lines. Based on the hydrophone scan results presented in Chapter 3, we verified that the distortion and loss in ultrasound intensity are strongly correlated with the selected imaging slice over the skull. Six imaging slices were selected to place the DMUA over the skull as shown in Figure 4.13. For each position, we performed

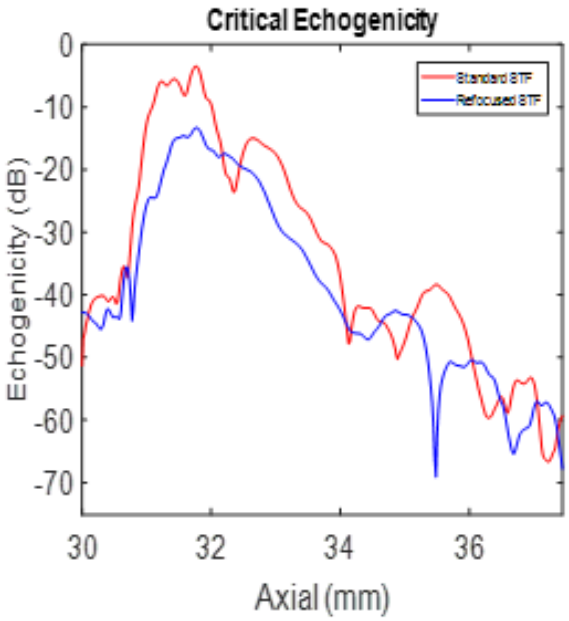

(a)

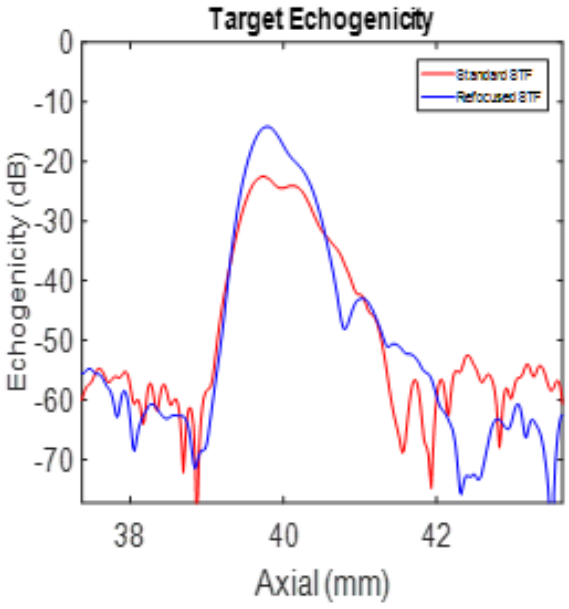

(b)

Figure 4.12: 45-dB grayscale STF images using: (a) geometrically focused and (b) optimally refocused DMUA excitation vectors.

the following:

- Acquiring SA images to guide the selection of target and critical points.
- Executing the refocusing algorithm to compute an optimal array excitation vector capable of minimizing the ultrasound intensity at the critical point while maximizing it at the target point.
- Generating STF images with and without refocusing to validate the improvement in echogenicity at and around the said points.
- Delivering tFUS with and without refocusing in order to validate the improvement in temperature rise and heating rate upon refocusing.

In the following discussion, we present the results obtained at image slices one, three, and four in details, including ultrasound images and line graphs. The results acquired at image slices two, five, and six are summarized in Table 4.7 for the sake of avoiding repetition.

Figure 4.14 shows a 40-dB grayscale SA image of the embedded skull and the inserted thermocouple in the tissue-mimicking phantom. The image was used to select the critical and target points for the imaging slice defined at location one in Figure 4.13. In particular, the critical point was selected along the medial suture line of the skull, while the target point was located at the thermocouple junction, which was inserted underneath the parietal bone of the skull. After extracting focused data matrices associated with the selected control points from RF echo data, updating the propagation operators, and solving for the optimal array excitation vector, we generated refocused STF images. The geometrically focused and refocused 40-dB garyscale STF images shown in Figures 4.15(a) and 4.15(b), respectively, illustrate changes in echogenicity at the target and critical points. The figures demonstrate the improvement in echogenicity at and around the target and critical points. For better visualization of echogenicity increase at the target point and echogenicity decrease at the critical point, we plotted the echogenicity profiles along segments of axial lines pass through the target and critical points with (blue)

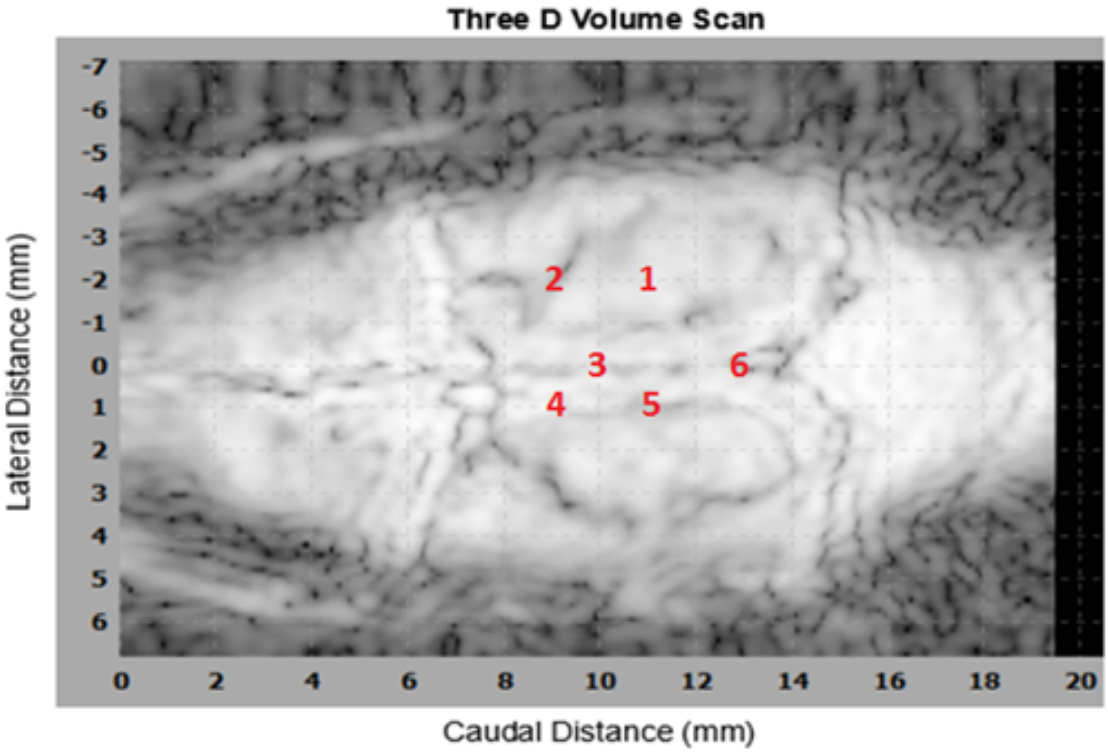

Figure 4.13: Three-dimensional volume scan image shows the selected image slices for tFUS application.

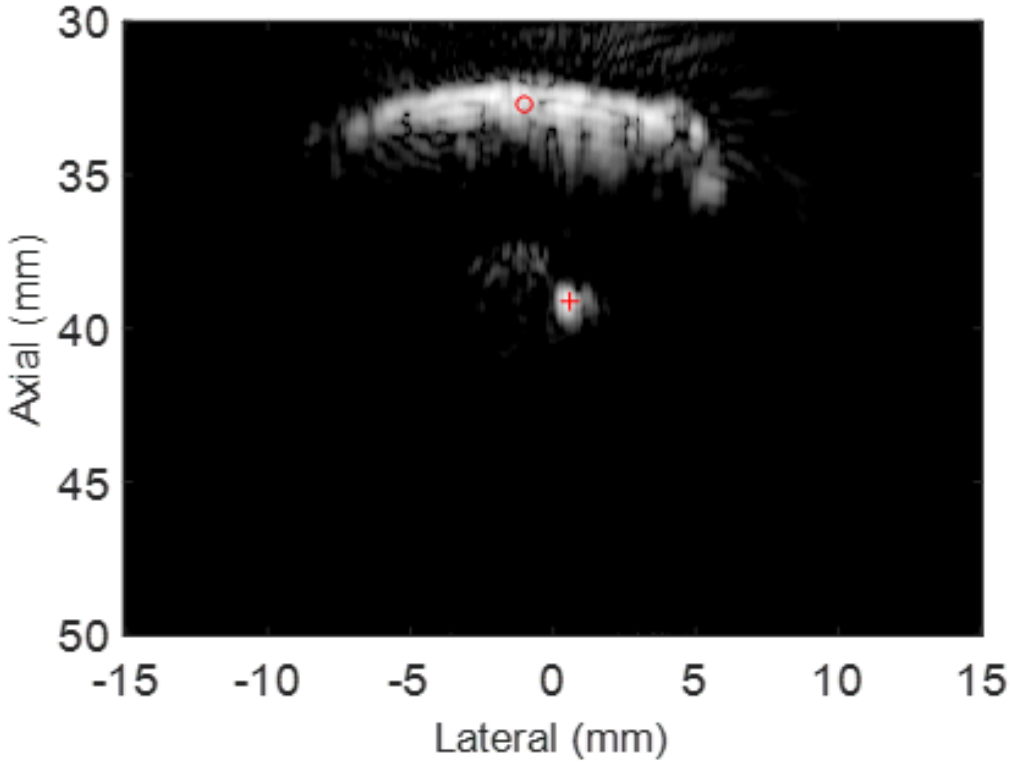

Figure 4.14: 40-dB grayscale SA image of the embedded skull and the inserted thermocouple of the first imaging slice.

and without (red) refocusing as demonstrated in Figures 4.16(a) 4.16(b). The findings clearly show that the echogenicity has increased at the target point and decreased at the critical point. In addition, we calculated the average echogenicity values of 1×1 mm^2 areas around target and critical points in geometrically focused and refocused STF images (Figures 4.15(a) and 4.15(b)). The results are summarized in Table 4.4. After refocusing, the average echogenicity value has increased by 2.8 dB for the target point and decreased by 6.6 dB for the critical point.

The tFUS beam with and without refocusing was used in therapy mode for a duration of 10 seconds to generate heat at the target point. However, the

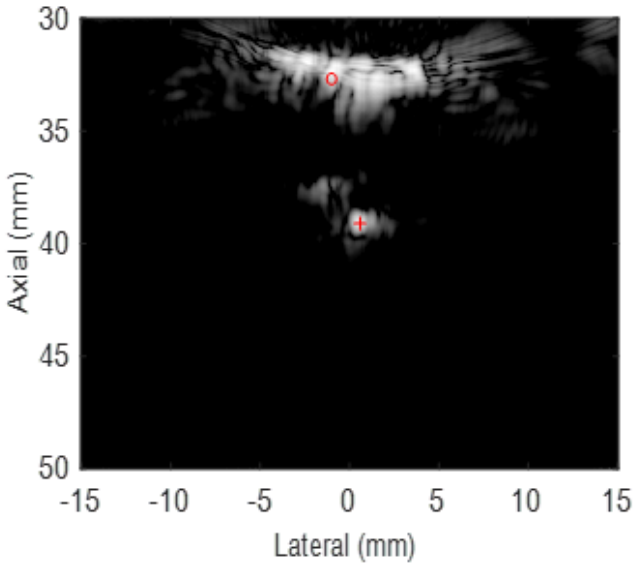

(a)

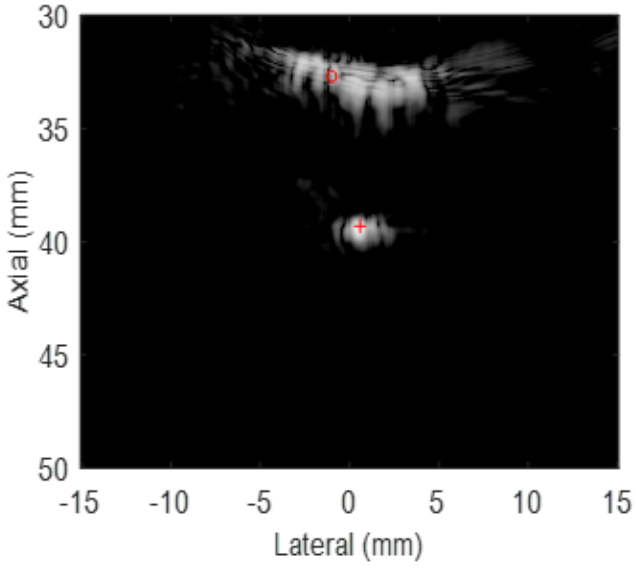

(b)

Figure 4.15: 45-dB grayscale STF images using: (a) geometrically focused and (b) optimally refocused DMUA excitation vectors.

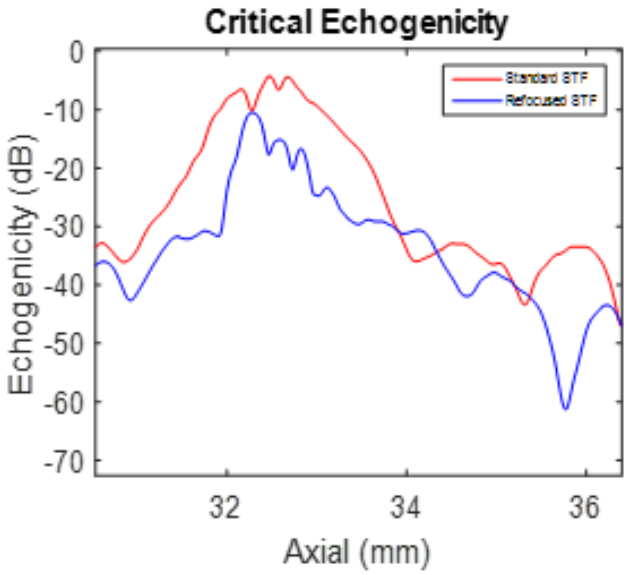

(a)

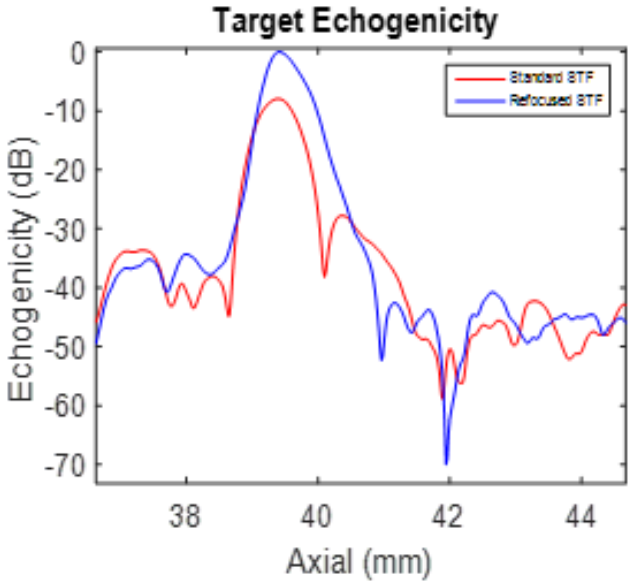

(b)

Figure 4.16: 45-dB grayscale STF images using: (a) geometrically focused and (b) optimally refocused DMUA excitation vectors.

Table 4.4: Average echogenicity values around target and critical points with and without refocusing for imaging slice number one.

Measurement criteria	Standard STF	Refocused STF
Target point average echogenicity (dB)	-11.7	-8.9
Critical point average echogenicity (dB)	-6.4	-13.0
Heating rate (°C/sec)	0.3	1.8

temperature was measured for a duration of 30 seconds, including the therapy time. The temperature profiles normalized to the maximum temperature obtained using the geometrically focused beam are illustrated in Figure 4.17. One can see that the temperature using the refocused tFUS beam increased by 126% compared to the geometrically focused tFUS beam. By calculating the heating rate values of the measured temperature profiles (Figure 4.18), we found that the heating rate increased by a factor of 6 due to refocusing. The maximum heating rate values achieved with and without refocusing are listed in Table 4.4.

For the imaging slice defined at location three in Figure 4.13, we selected the target and critical points to be axially aligned (Figure 4.19) and located at the thermocouple junction as well as along the medial suture line of the skull, respectively. The critical point was selected along the medial suture line because it represents the most complex and the strongest reflector between the bregma and lambda suture lines of the skull. Therefore, it is the biggest obstacle for ultrasound beam as it propagates through the skull to achieve a desired focusing gain deep in the brain. We generated 40-dB grayscale STF images using the geometrically focused and refocused ultrasound beams to characterize the improvement

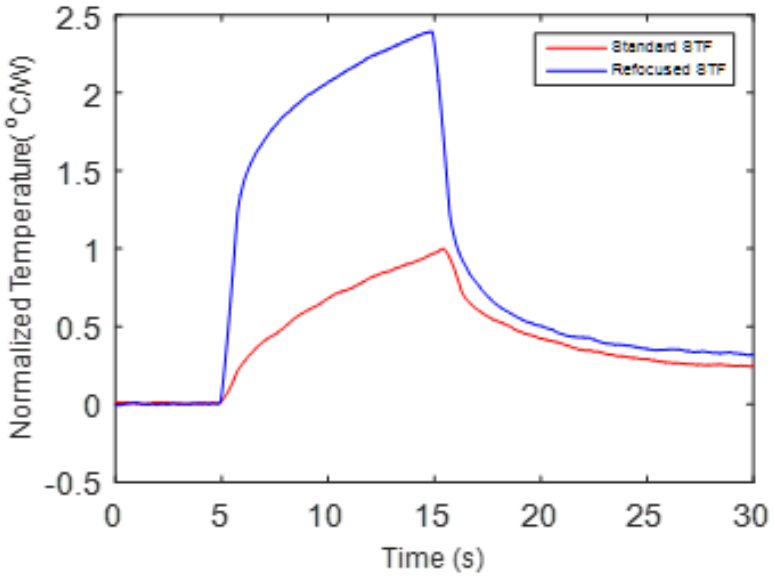

Figure 4.17: Normalized temperature measurement profiles of imaging slice number one with and without refocusing.

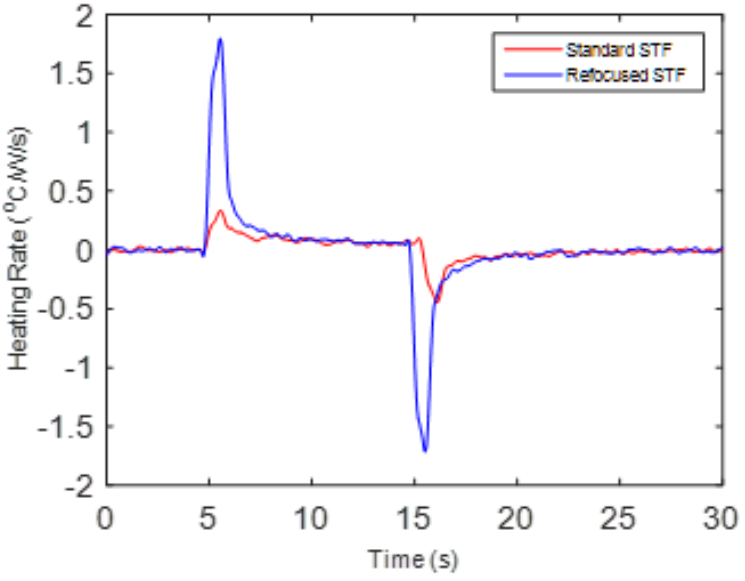

Figure 4.18: Heating rate values of the measured temperature profiles at imaging slice number one with and without refocusing.

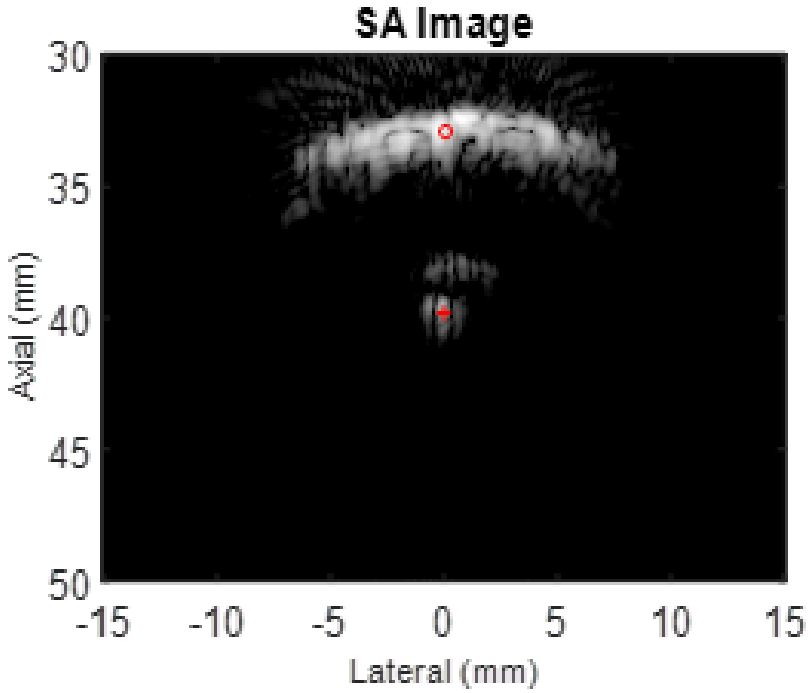

Figure 4.19: 40-dB grayscale SA image of the embedded skull and the inserted thermocouple of the imaging slice at location three.

in echogenicity at the control points due to refocusing. The images are shown in Figure 4.20. They clearly demonstrate the feasibility of the refocusing algorithm to significantly decrease the echogenicity at and around the critical point while increasing it at the target point. In addition, we plotted the echogenicity along an axial line passing through the critical and target points from both STF images for better visualization as demonstrated in Figure 4.21. The graph figure clearly shows the echogenicity increase at the target point and decrease at the critical point. The average echogenicity values of 1×1 mm^2 areas around target and critical points in geometrically focused and refocused STF images are listed in Table 4.5. After refocusing, the average echogenicity value increased by 1.7 dB around the target point, while it decreased by 9.3 dB around the critical point.

We generated a tFUS beam with and without refocusing to be used in therapy

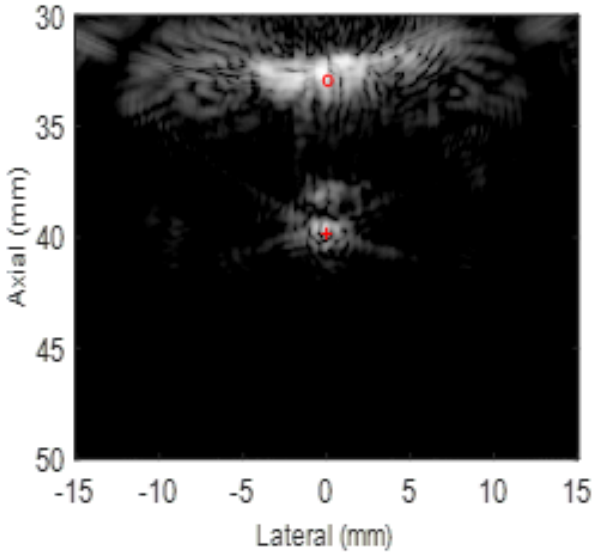

(a)

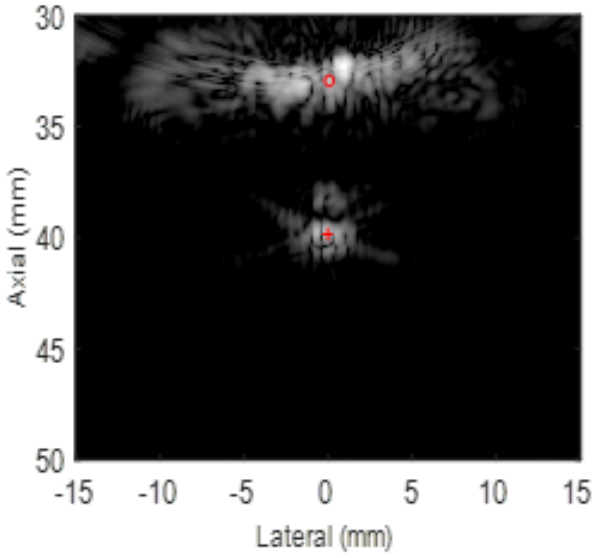

(b)

Figure 4.20: 40-dB grayscale STF images using: (a) geometrically focused and (b) optimally refocused DMUA excitation vectors of imaging slice number three.

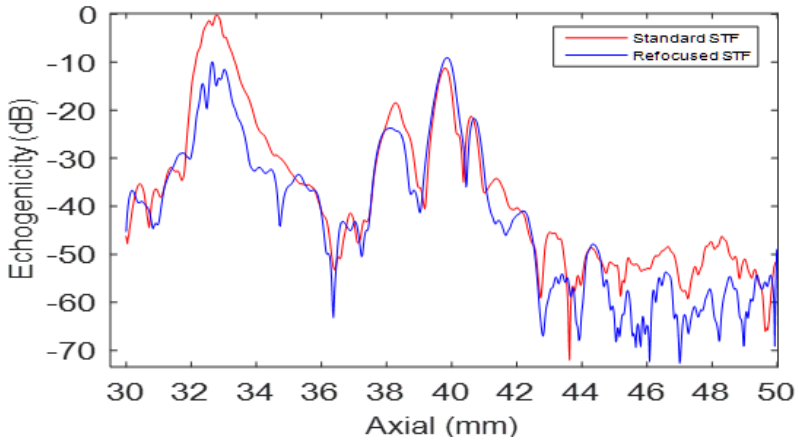

Figure 4.21: Echogenicity profiles in dB along an axial line passes through the critical and target points demonstrated in the previous figure.

Table 4.5: Average echogenicity values around target and critical points as well as heating rate values at target location with and without refocusing for imaging slice number three.

Measurement criteria	Standard STF	Refocused STF
Target point average echogenicity (dB)	-20.7	-19.0
Critical point average echogenicity (dB)	-7.1	-16.4
Heating rate (°C/sec)	1.1	1.4

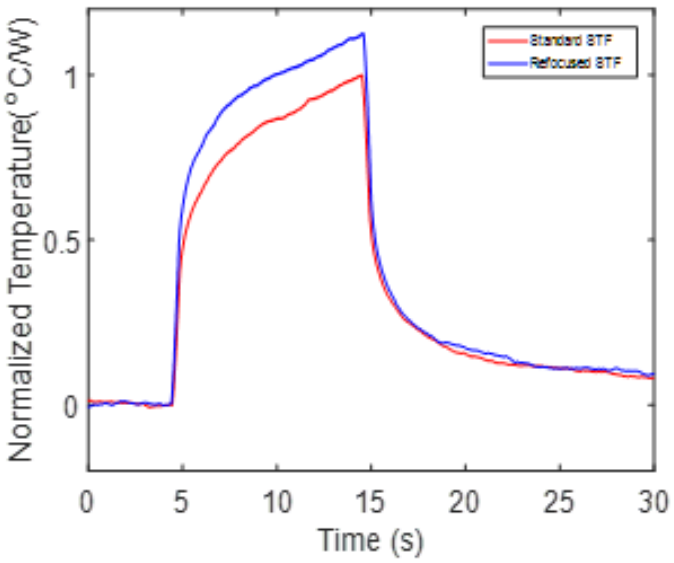

Figure 4.22: The normalized temperature measurement profiles with and without refocusing of imaging slice number three.

mode for a duration of 10 seconds each in order to generate heat at the target point. The temperature profiles normalized to the maximum temperature obtained using the geometrically focused beam are illustrated in Figure 4.22. Temperature measurements were recorded at a rate of 100 readings per second. The maximum temperature recorded during the application of the refocused beam was increased by 13% more than the maximum temperature obtained during the application of the geometrically focused beam.

By deriving the heating rate values of the measured temperature profiles (Figure 4.23), we showed that the heating rate was increased by a factor of 1.27 due to refocusing. Table 4.5 includes the maximum heating rate values achieved with and without refocusing. The improvement of the heating rate at this imaging slice is not as large as the improvement at the imaging slice defined at location one because the tFUS beam in this case was traveling through one of the most complex structures of the skull, which is the medial suture line.

For the imaging slice defined at location four in Figure 4.13, again the target

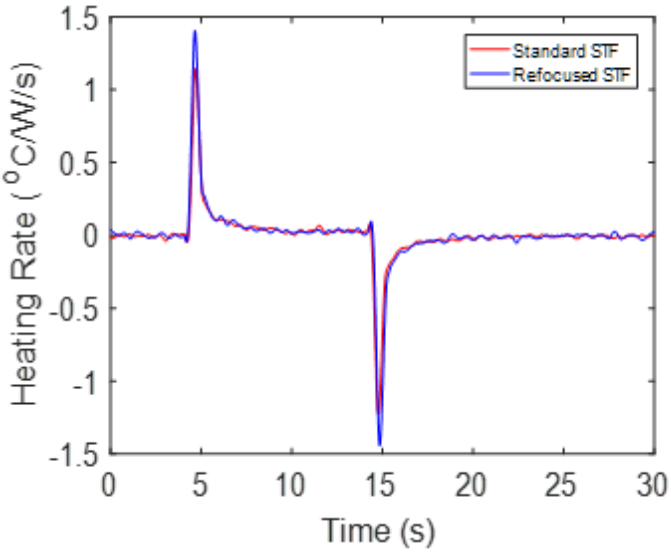

Figure 4.23: Heating rate values of the measured temperature profiles with and without refocusing of imaging slice number three.

and critical points were selected to be at the thermocouple junction and the medial suture line of the skull, respectively. This imaging slice is closer to the bregam suture line as compared to the image slices selected at locations one and three. This means that the bone at this location is thicker than the bone of the image slices selected at locations one and three. Figure 4.24, which is an SA image collected using the DMUA, shows the locations of the target and critical points. We used the figure data to compute a refocused array excitation vector capable of reducing the acoustic energy deposition over the critical point while improving the energy deposition at the target point. The refocused array excitation vector and the geometrically focused one were used in both imaging and therapy modes to validate the feasibility of the refocusing algorithm.

In imaging mode, we collected 40-dB grayscale STF images with and without refocusing and validated the improvement in terms of echogenicity. It is clear from the images (Figure 4.25) that the echogenicity decreased at and around the critical point, while it increased at the target point. The echogenicities along axial

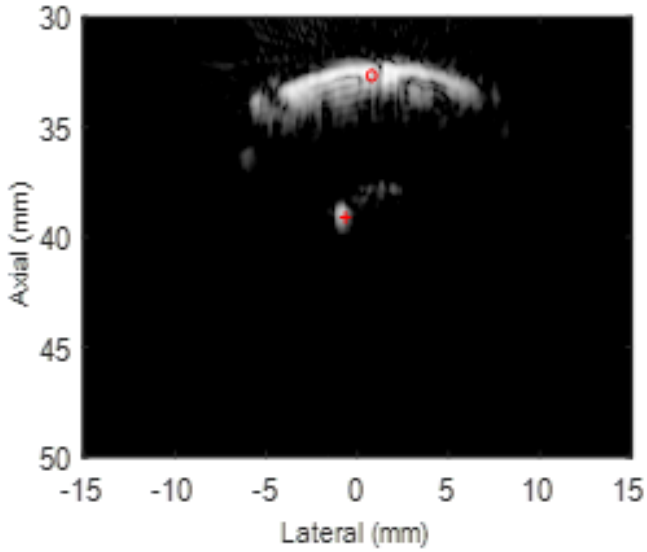

Figure 4.24: 40-dB grayscale SA image of the embedded skull and the inserted thermocouple of the imaging slice at location four.

line segments pass through the critical and target points from both STF images are shown in Figure 4.26 for better visualization. The blue lines demonstrate the results from the refocused STF image, while the red lines demonstrate the result from the geometrically focused STF image. From this figure, one can easily see that the echogenicity has increased at the target point, while it has decreased at the critical point. The average echogenicity values of a 1×1 mm^2 areas around the target and critical points in geometrically focused and refocused STF images are listed in Table 4.6. After refocusing, the average echogenicity value increased by 0.5 dB around the target point, while it decreased by 4.4 dB around the critical point.

In therapy mode, we generated tFUS beams with and without refocusing to generate heat at the target point. The beams were used for a duration of 10 seconds and the temperature was recorded for a duration of 30 seconds. The

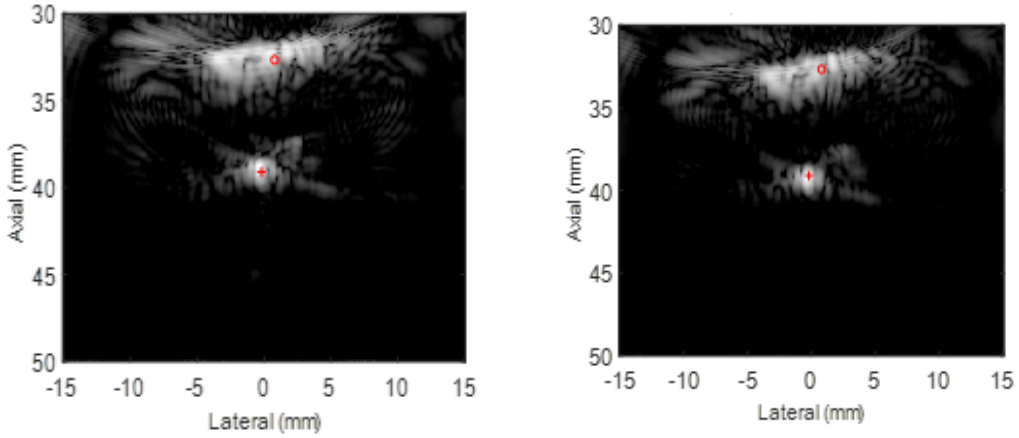

(a) (b)

Figure 4.25: 40-dB grayscale STF images using: (a) geometrically focused and (b) optimally refocused DMUA excitation vectors of imaging slice number four.

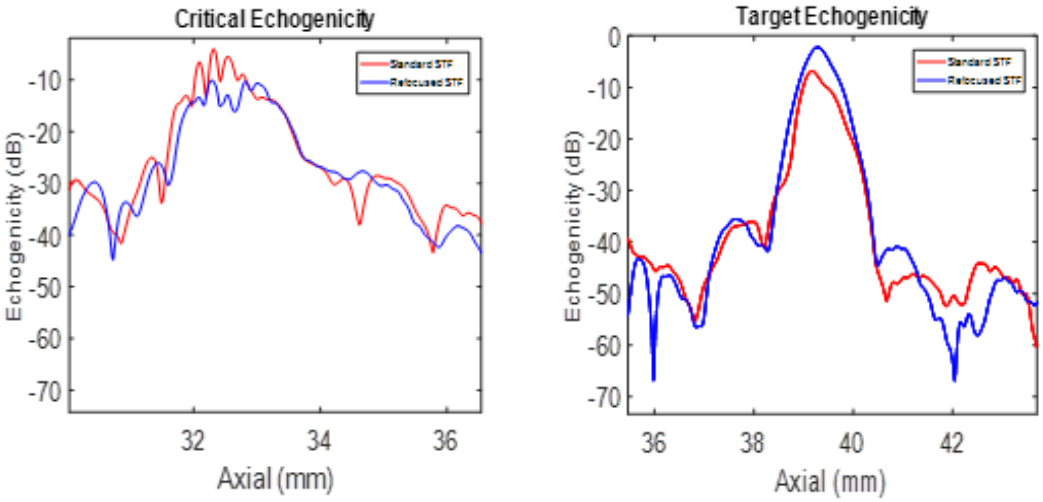

(a) (b)

Figure 4.26: Echogenicity profiles in dB along a segment of axial lines through the selected: (a) critical point on the skull and (b) target point on the thermocouple junction.

Table 4.6: Average echogenicity values around target and critical points as well as heating rate values at target location with and without refocusing for imaging slice number four.

Measurement criteria	Standard STF	Refocused STF
Target point average echogenicity (dB)	-10.3	-9.8
Critical point average echogenicity (dB)	-7.6	-12.0
Heating rate (°C/sec)	0.4	0.9

recording started 10 seconds before applying the beam and continued for 10 seconds after the beam application. Temperature measurements were collected using a rate of 100 readings per second. The temperature profiles are shown in Figure 4.27. We derived the heating rate values of the measured temperature profiles and demonstrated the results in Figure 4.28. As we can see from the results, the heating rate was increased by a factor of 2.25 due to refocusing. Table 4.6 includes the maximum heating rate values obtained using the geometrically focused and the refocused ultrasound beams.

The experimental results of refocusing over image slices 2, 5, and 6, as identified in the skull three-dimensional scan (Figure 4.13), are summarized in Table 4.7. At each image slice location, the generated refocused excitation vector as well as the geometrically focused vector were used in both imaging and therapy modes. The imaging mode was used to validate the improvement due to refocusing in terms of echogenicity, while the therapy mode was used to validate the improvement in terms of heating rate. The improvements at target points were varied from one imaging slice location to another because each location was interfaced

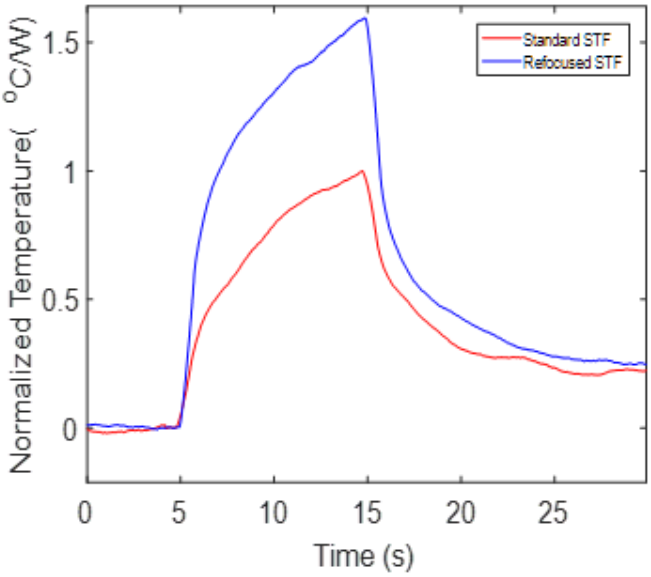

Figure 4.27: The normalized temperature measurement profiles with and without refocusing of imaging slice number four.

with different skull bone structure. The generated B-mode images as well as the temperature and heating rate curves are not shown here to avoid repetition.

4.5 Discussion

The results presented in this chapter validate a new real-time image-based refocusing algorithm for tFUS applications in order to achieve sub-therapeutic and therapeutic ablative treatments. To the best of our knowledge, the refocusing algorithm presented is the first one to compute an optimal array excitation vector that controls the acoustic power incidence at selected target and critical points and download it into the DMUA driver in real-time. The availability of the advanced DMUA technology and the arbitrary waveform generator is a key to implementing the algorithm. DMUAs are capable of operating in both therapy and imaging modes in real-time allowing for immediate feedback on tFUS-tissue

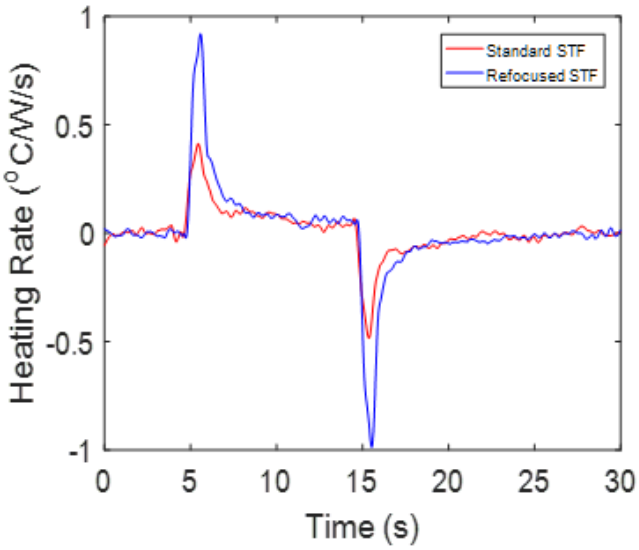

Figure 4.28: Heating rate values of the measured temperature profiles with and without refocusing of imaging slice number four.

interactions. The high frame rate imaging capability of the DMUA as well as the inherent registration between its imaging and therapeutic coordinate systems allow us to use it for guidance and monitoring. The system that we have in our laboratory supports 30 frames per second (fps) in SA imaging mode and up to 1000 fps in STF imaging mode [18]. The frame rate upper limit limitation is due to the use of a gigabit ethernet to upload the DMUA element data for processing. Nevertheless, the supported frame rates are sufficient to capture the fast tissue deformation dynamics, including pulsations, breathing and mechanical responses to the acoustic radiation force effects of tFUS.

The results presented in this chapter emphasized the different levels of tFUS beam distortion and loss through different parts of the skull. These results add to the benefits of performing a 3D volume scan of the skull before targeting specific locations in the brain. Selecting image slices over thin parts of the skull means achieving higher focusing gain at a target location due to tFUS application. Temperature measurement profiles and heating rate calculations at target locations

Table 4.7: Average echogenicity values around target and critical points from STF images and the heating rate values at target location with and without refocusing at locations 2, 5, and 6 shown in Figure 4.13.

Imaging location	Paradigm	Aver. Echogen. at Target (dB)	Aver. Echogen. Crit. Pt (dB)	Heating Rate (°C/sec)
2	Standard STF	-16.8	-5.8	0.3
	Refocused STF	-7.3	-8.8	1.6
5	Standard STF	-11.6	-15.5	0.5
	Refocused STF	-9.2	-16.9	1.3
6	Standard STF	-22.6	-6.3	0.28
	Refocused STF	-15.3	-7.1	0.57

demonstrate that there is an improvement in focusing gain every time we perform refocusing. This is true regardless of where the target location is selected underneath the skull. However, if the embedded skull is tilted in the elevation direction and not perpendicular to the tFUS beam, the capability of refocusing to achieve high ultrasound intensity level at a targeted location is compromised. Furthermore, finding the correct location of the thermocouple junction without aberration is a limitation in this study because we insert the thermocouple in the tissue-mimicking phantom after we embed the skull.

4.6 Conclusion

A real-time image-based refocusing algorithm for optimal delivery of focused ultrasound to a selected target point while minimizing the exposure to a selected critical point on the skull surface has been experimentally demonstrated. The demonstration utilized *ex vivo* skull samples from animals that have undergone *in vivo* treatments under IACUC approved protocol [18]. Water tank measurements

using the tip of a needle hydrophone as a target demonstrated the advantages of the refocusing algorithm in improving the relative echogenicity at the target with respect to the echogenicity at the selected critical point at the surface of the skull. This offers the promise of using echogenicity as a form of feedback in adaptive refocusing. A more realistic demonstration was performed using *ex vivo* skull samples embedded in tissue-mimicking phantoms where a steel needle thermocouple was used as a target. In these experiments, heating of the thermocouple was used as an indicator od improved focusing. More specifically, heating rate was used as a measure of focusing gain improvements due to the refocusing algorithm.

The experimental results shown in this chapter allows for the following specific conclusions:

1. For each target location, refocusing resulted in measurable improvement in heating rate, i.e. improved focusing gain.

2. Improvements in focusing gain are spatially dependent.

3. Changes in echogenicity at the target and critical points are consistent with the improved delivery of focused ultrasound to the target while minimizing the energy at the critical point. However, at least for the beamforming settings used in generating the results reported herein, they are not quantitative.

It should be emphasized that 3D DMUA imaging of the skull surface for defining the target planes played a significant role in the repeatability of the measurements reported herein. This is due to the now established fact that the geometry and propagation properties of the skull have significant spatial variability, especially near the suture lines.

Chapter 5

Wideband Transskull Transmission Characteristics and Refocusing of Ultrasound Beams

5.1 Introduction

Transcranial focused ultrasound (tFUS) is capable of providing subtherapeutic and therapeutic ablative treatments in the brain. It represents a promising non-invasive treatment modality for treating several brain related diseases, including tumor ablation, Parkinsons disease, epilepsy, and essential tremor. This relies on the theoretical promise of generating spatially localized acoustic power deposition in the targeted region within the brain. Advances in image guidance, including MRI, have led to increased interest in new tFUS-based therapies.

The early efforts of targeting brain tissue using ultrasound beams were performed with the skull removed (craniotomy). This was performed because the presence of the skull and other obstacles in the propagation path of the ultrasound beam distort the beam in several forms, including absorption, scattering, and reflection. In addition, the large discrepancy in acoustic properties (e.g. speed of sound and density) between soft tissues and skull tissues adds up to the

challenges of using tFUS beams effectively.

The research presented in this chapter is intended to provide quantitative measurements of the acoustic energy loss due to the skull at different operating frequencies. In particular, we used a set of 32 discrete frequencies that cover the frequency range from 1.9 to 5.0 MHz. At each frequency, we performed transskull hydrophone point and plane scan measurements; therefore, a range of tFUS beam distortions was documented. These distortions could compromise the effectiveness and the specificity of targeting brain circuitry and/or cause collateral damage at unintended locations. In addition, we present *ex vivo* experimental results demonstrating the feasibility of the image-based refocusing at each frequency of the set to maximize the localization and reclaim the focusing gain. The experiments have been performed in a deionized/degassed water tank and on tissue mimicking phantoms.

5.2 Materials and Methods

5.2.1 Dual-Mode Ultrasound Array Prototype

Our experiments were anchored on the use of the DMUA system that we have in our laboratory, Ultrasound Imaging and Signal Processing Laboratory (UISPL). In particular, a wideband DMUA prototype of 32 channels, 40-mm radius of curvature was utilized. Some of the key features of the DUMAs are their capability to perform real time-imaging in several methods and the inherent registration between their imaging and therapy coordinates. In other words, the imaging and therapy modes of operation share the same transducer elements, and hence the insonified medium seen by the two modes is the same. The difference between the two modes of operation is only in the excitation signal amplitude levels and duration. Therefore, the imaging data can be used as a map of acoustic energy deposition during therapy. Another key feature is that DMUAs are capable of using custom-designed arbitrary waveforms in imaging and therapy modes, making

it possible to correct for skull-induced aberration in real time. In the refocusing experiments presented in this chapter, we computed a refocused array excitation vector, generated refocused excitation waveforms, and pushed the waveforms into the DMUA system in real time.

5.2.2 Hydrophone in Water Tank Experiments

A Wideband 0.2 mm needle hydrophone (Onda Corp, Sunnyvale, CA) of operating frequency range from 0.5 to 10 MHz have been used to characterize the tFUS beam deformation through the skull. The studies were performed in a water tank with and without the presence of rodent skull samples. The skull samples were extracted from Sprague Dawley rats and preserved in formalin solution. At the beginning of the experiments, we firmly fixed the DMUA in the water tank with the help of mechanical screws and then filled the tank with deionized/degassed water. Afterwards, the needle hydrophone was immersed in the tank using an electronically controlled 3-stage motor (Parker Daedal, Rohnert Park, CA). The hydrophone tip was localized at the focal point of the DMUA with the guidance of SA imaging.

We performed hydrophone single point measurements and plane scans to characterize the tFUS beam distortions due to the of the skull. We introduced the skull between the DMUA and the hydrophone tip using forceps as demonstrated in Figure 5.1. The skull was positioned at a distance of 32 mm from the apex of the DMUA. This location corresponds to the skull location during our *in vivo* experiments. A 3D volume scan was performed to identify the bregma and lambda suture lines of the skull, and hence selecting planes between the lines to apply the tFUS beam. To understand the tFUS beam nature without skull-induced aberrations, we repeated the measurements and the scans without the skull presence. The acoustic data captured by the needle hydrophone with and without the skull were first amplified using AH 2010 preamplifier, and then acquired by a Tektronix oscilloscope. Afterwards, they were transferred to a PC using an Ethernet cable.

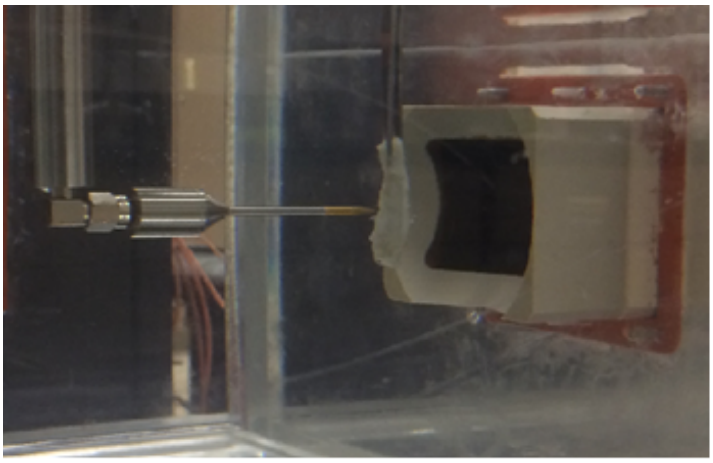

Figure 5.1: Transcranial FUS beam characterization experimental setup.

The tFUS beams used during the experiments were generated at a set of 32 discrete frequencies within the DMUA transducer bandwidth. The set covers the frequency range from 1.9 to 5.0 MHz with a separation frequency of 100 KHz. At every frequency, a gated sinusoidal waveform of 11 μs duration was designed and fed into the DMUA system to generate an ultrasound beam. Figure 5.2 shows the generated sinusoidal signals at frequencies 2.4 and 4.7 MHz. Transcranial FUS beams produced at each frequency out of the 32 frequencies were used in performing the single point measurements as well as the complete plane scans with and without the skull. The measurements were taken at several points behind the skull, where the hydrophone tip was initially located at the geometric center of the DMUA and then was moved to selected point locations.

The plane scans were performed in a plane parallel to the surface of the array (lateral-elevation directions) with a separation distance of 40 mm from the array apex. We used the needle hydrophone to execute the scans of the acoustic intensities generated at each frequency in the set. The hydrophone measured the intensities with and without the skull at increments of 0.05 mm the lateral direction and 0.1 mm in the elevation direction.

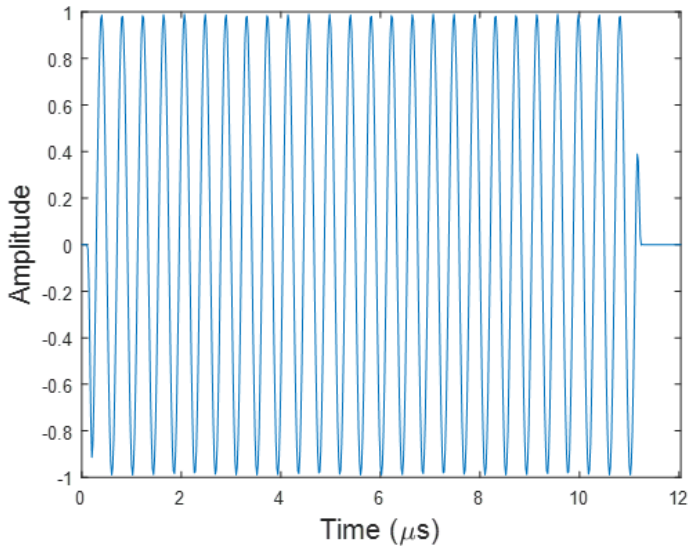

(a)

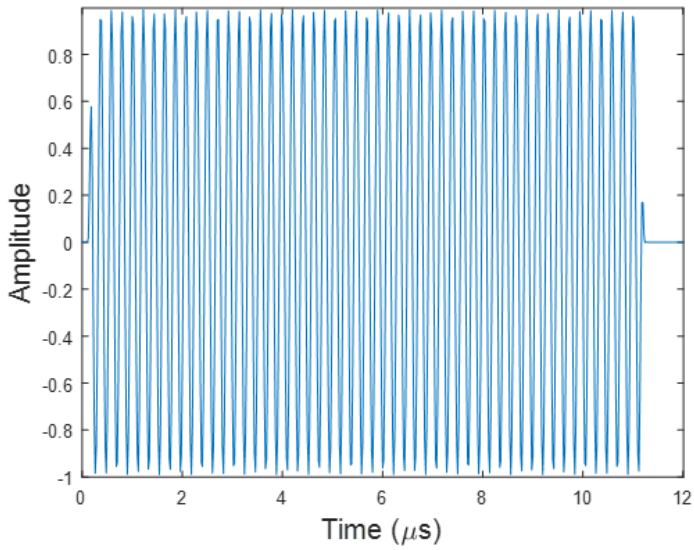

(b)

Figure 5.2: Gated sinusoidal signals of frequencies (a) 2.4 MHz and (b) 4.7 MHz.

5.2.3 Thermocouple in Tissue-Mimicking Phantom Experiments

A fine diameter (200 μm) T-type constant thermocouple have been used to characterize heat rates with and without tFUS refocusing in phantom experiments. We designed and fabricated tissue-mimicking phantoms that contain rodent skull samples for the sake of the experiments. We used specific quantities of graphite, gelatin, propanol, glutaraldehyde, and water in phantom fabrication. The quantities are described in [67, 68]. During phantom fabrication, we first fixed the skull in the phantom container and then added the phantom mixture into the container, while it was still in the liquid state. The phantom mixture was degassed using laboport vacuum pump manufactured by KNF Neuberger Inc., Trenton, NJ, USA.

The embedded skulls were positioned at a distance of approximately 32-mm from the apex of the DMUA (corresponding to the skull position during *in vivo* experiments). This positioning was made possible by controlling the amount of water encapsulated inside the DMUA bolus as seen in Figure 5.3. To ensure a strong coupling between the DMUA bolus and the phantom surface, we added a layer of degassed ultrasound gel. At the beginning of each experiment, we performed a 3D volume scan of the embedded skull to visualize important landmarks over the skull and select an appropriate imaging slice. Then, we inserted the thermocouple in the phantom underneath the skull so that its shaft was perpendicular to the DMUA imaging slice. The thermocouple junction was closest to the geometric center of the DMUA and used as a target point in the refocusing experiments. A data acquisition unit (34970A, Agilent, Santa Clara, CA) was set at a rate of 100 Hz and connected to the thermocouple to acquire the temperature measurements.

Transcranial FUS beams at a set of different frequencies were used to generate heat at the thermocouple junction underneath the skull with and without refocusing. The set of 32 discrete frequencies ranged from 1.9 to 5.0 MHz with a separation frequency of 100 KHz. At every frequency in the set, we designed a

Figure 5.3: DMUA encapsulated within a water bolus.

gated sinusoidal waveform of 158 μs duration and fed it into the DMUA system to generate a tFUS beam. Figure 5.4 shows the generated sinusoidal signal at frequency 3.0 MHz and its spectrogram. An 80-dB spectrogram of all the used signals is demonstrated in Figure 5.5. It is clear from the figure that the signals are orthogonal and centered at their designated frequencies.

5.2.4 Real-Time Image Based Refocusing

The Real-time image-based refocusing algorithm described in Chapter 4 is used to produce the refocusing results presented in this chapter but with the set of 32 frequencies. Briefly, the objective of the refocusing algorithm is to optimize the tFUS beam in order to improve the focusing gain at selected target and critical points. This was achieved by exploiting the availability of the RF echo data received by

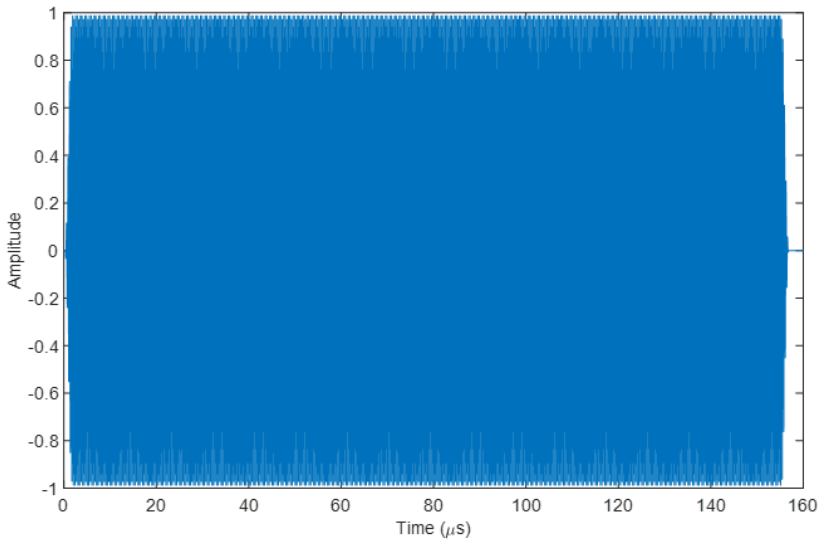

(a)

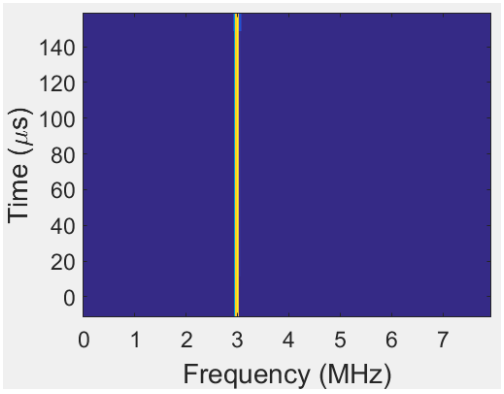

(b)

Figure 5.4: (a) Gated sinusoidal signal of frequency 3.0 MHz and (b) its 80 dB spectrogram.

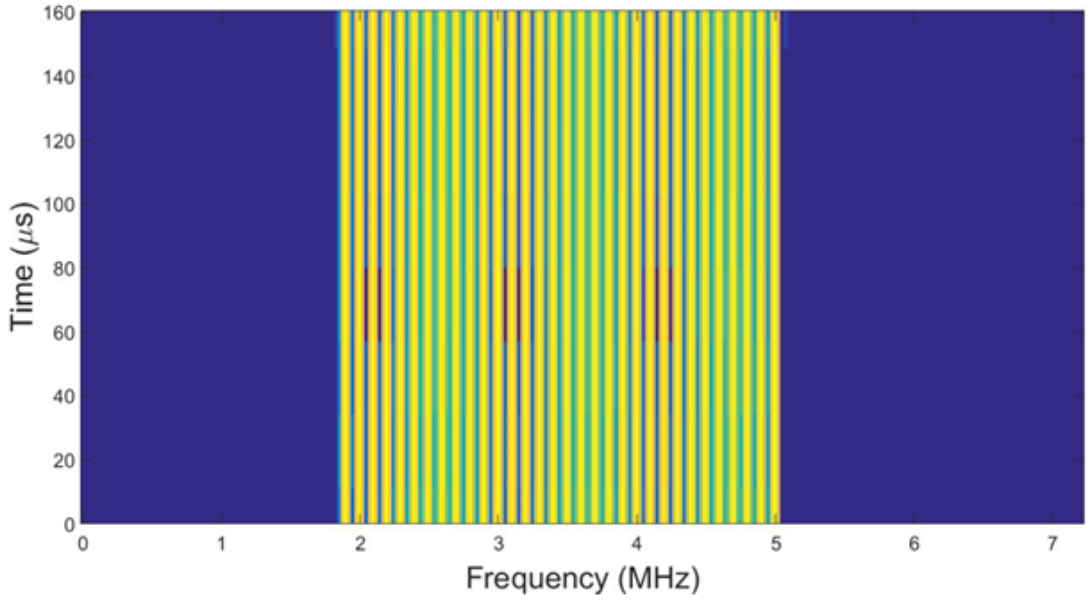

Figure 5.5: 80 dB spectrogram plot shows the frequency content of the designed signals.

each element of the DMUA to form focused data matrices (FDMs) corresponding to the selected control points. The FDMs were utilized to solve eigenvalue decomposition problems, and then the computed eigenvalues and eigenvectors were used to update the propagation operators from the elements of the DMUA to the control points. The propagation operator defines the basis for synthesizing an array driving excitation vector. The entries of the propagation operator matrix represent the array element directivities at the control points in the field of view of the ultrasound array. For example, the entry $h(m, n)$ is the directivity of the ultrasound array n^{th} element at the m^{th} control point. With the propagation operators in hand, an optimal solution to the pattern synthesis problem could be obtained by the following equation:

$$\boldsymbol{u}_{opt} = \boldsymbol{W}_c^{-1}\boldsymbol{H}_t^*(\boldsymbol{H}_t\boldsymbol{W}_c^{-1}\boldsymbol{H}_t^*)^{-1}p_t, \tag{5.1}$$

with

$$\boldsymbol{W}_c = (\boldsymbol{H}_c^*\boldsymbol{H}_c + \gamma\boldsymbol{I}), \tag{5.2}$$

where $\boldsymbol{H}_t$ and $\boldsymbol{H}_c$ are the forward propagation operators from the DMUA elements toward the target and critical points, respectively. The scalar p_t is the desired acoustic pressure at the target location and γ is a regularization parameter.

5.3 Results

In this section, we present the findings of experimental studies performed to characterize the tFUS beam distortions due to the skull at different operating frequencies. In addition, refocusing experimental results at the set of operating frequencies in water tank and tissue-mimicking phantom will be presented.

5.3.1 Single-Point Hydrophone Measurements

The results of single-point hydrophone measurements in the degassed/deionized water tank with and without the skull are presented in this subsection. We selected the points to be at and around the geometric center of the of the DMUA as follows:

- At the geometric center of the DMUA, (0, 40) mm from the DMUA apex.
- Two millimeter to the left of the DMUA geometric center, (-2, 40) mm.
- Two millimeter to the right of the DMUA geometric center, (2, 40) mm.
- Two millimeter closer to the DMUA surface from geometric center, (0, 38) mm.
- Two millimeter away in the axial direction from geometric center, (0, 42) mm.

Figure 5.6 shows 40 dB-grayscale SA images of the hydrophone tip behind the skull captured at each point. As can be seen from the figure, the skull is located at a distance of 32 mm from the surface of the DMUA. We selected two planes over the skull to characterize the broadband transmission of the tFUS beam. The skull

plane selection was marked with respect to the bregma suture line. We selected the first plane at bregma -0.5 mm and the second plane at bregma -2.5 mm as demonstrated in Figure 5.7.

Figure 5.8 shows the results of the normalized acoustic energy received by the hydrophone when it was positioned at the geometric center of the DMUA. The results are normalized with respect to the acoustic energy received in plain water without the presence of the skull. As we can see from the figure, the transmission efficiency of the tFUS beams at a specific location over the skull varied as a function of frequency in a nonmonotonic manner. For example, the acoustic energy received behind location one of the skull, which was selected at bregam -0.5 mm, is about -4 dB at operating frequency of 1.9 MHz, -7 dB at operating frequency of 3.0 MHz, and -3 dB at operating frequency of 4.2 MHz. In addition, different regions after the same skull have different transmission efficiency of a tFUS beam operating at the same frequency. For instance, the acoustic energy received due to applying a tFUS beam operating at 4.8 MHz behind location one of the skull (bregma -0.5 mm) is about -5 dB, while behind location two (bregma -2.5 mm) is about -8 dB.

When we positioned the hydrophone tip around the geometric center of the DMUA, we obtained the results depicted in Figure 5.9. Specifically, Figure 5.9(a) illustrates the normalized acoustic energy received by the hydrophone when its tip was localized at a distance of two millimeter to the left of the DMUA geometric center (i.e. (-2, 40) mm). The results presented in the figure emphasize the fact that tFUS beams operating at different frequencies experience different levels of distortion. Some frequencies achieve higher acoustic energy transmission than others over the same region of the skull. In addition, the results demonstrate that different regions over the same skull have different transmission efficiency for the ultrasound beam. After moving the hydrophone tip two millimeter to the right of the DMUA geometric center, we obtained the findings seen in Figure 5.9(b). The findings clearly demonstrate the idea that the skull represents an inhomogeneous barrier for the tFUS beam. In other words, the transmission efficiency of the

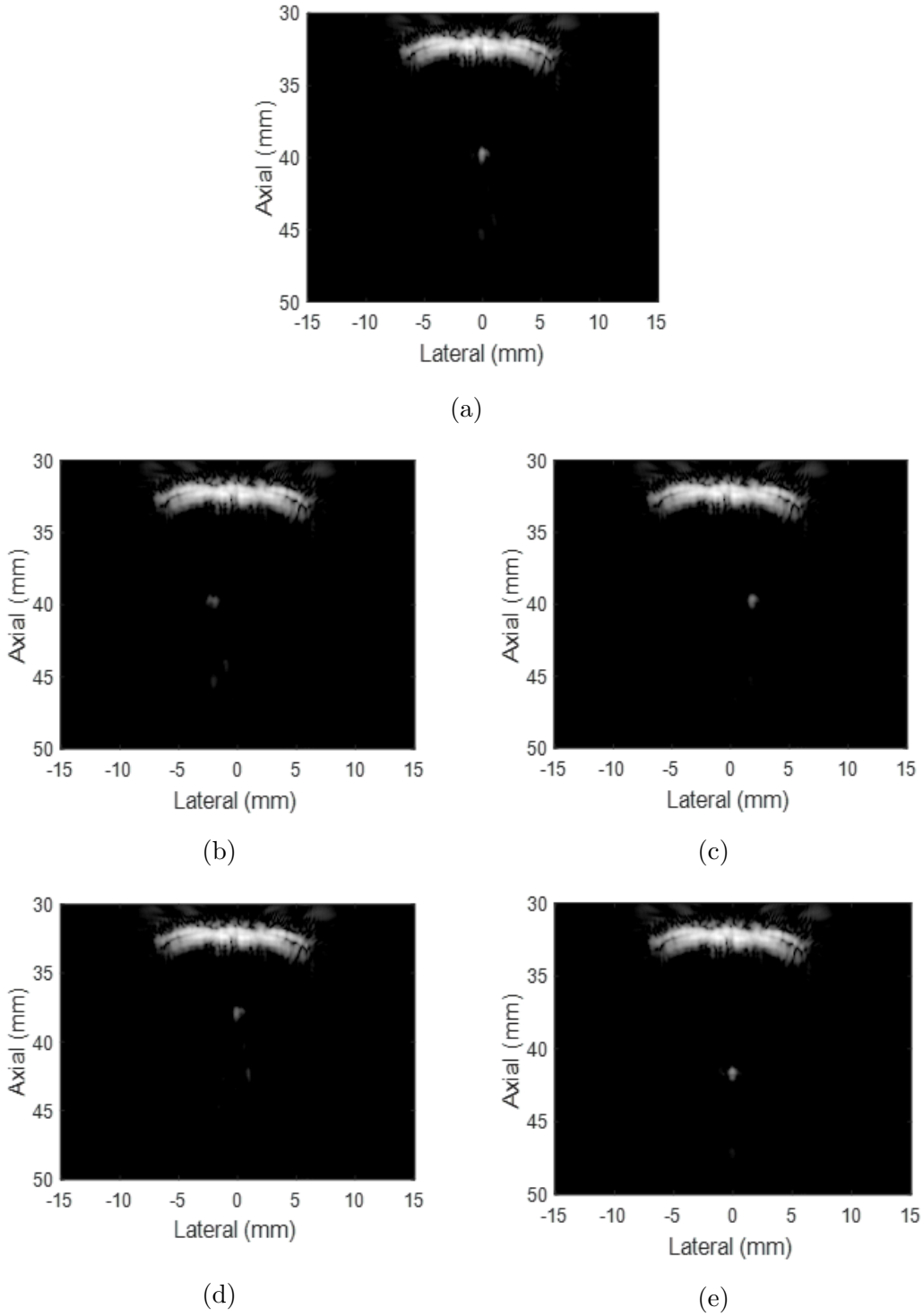

Figure 5.6: 40 dB-grayscale SA images of the skull and hydrophone tip at (a) (0, 40) mm) (the DMUA geometric center), (b) (-2, 40) mm, (c) (2, 40) mm, (d) (0, 38) mm, and (e) (0, 42) mm.

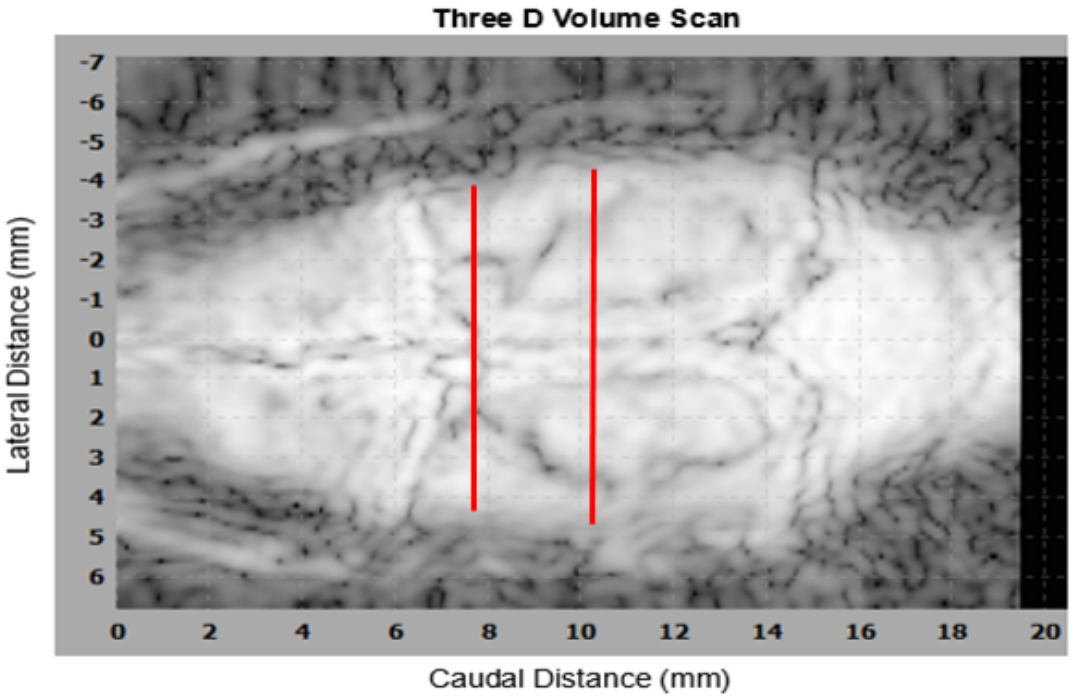

Figure 5.7: Three dimensional volume scan of the skull illustrating two imaging slices at bregma -0.5 mm and bregma -2.5 mm.

tFUS beams at a specific location over the skull varied as a function of frequency in a nonmonotonic manner. Moreover, different planes over the same skull, have different transmission efficiency of a tFUS beam operating at the same frequency. Figure 5.9(c) illustrates the acoustic energy received by the hydrophone when its tip was localized at (0, 38) mm, two millimeter closer to the DMUA surface from geometric center. The curves in the figure express the same behavior seen at other hydrophone tip locations. In addition, the results obtained when the hydrophone tip was at (0, 42) mm from the apex of the DMUA illustrated the nonmonotonic nature of the received energy as a function of frequency and the skull region. However, the results are not shown here to avoid repetition.

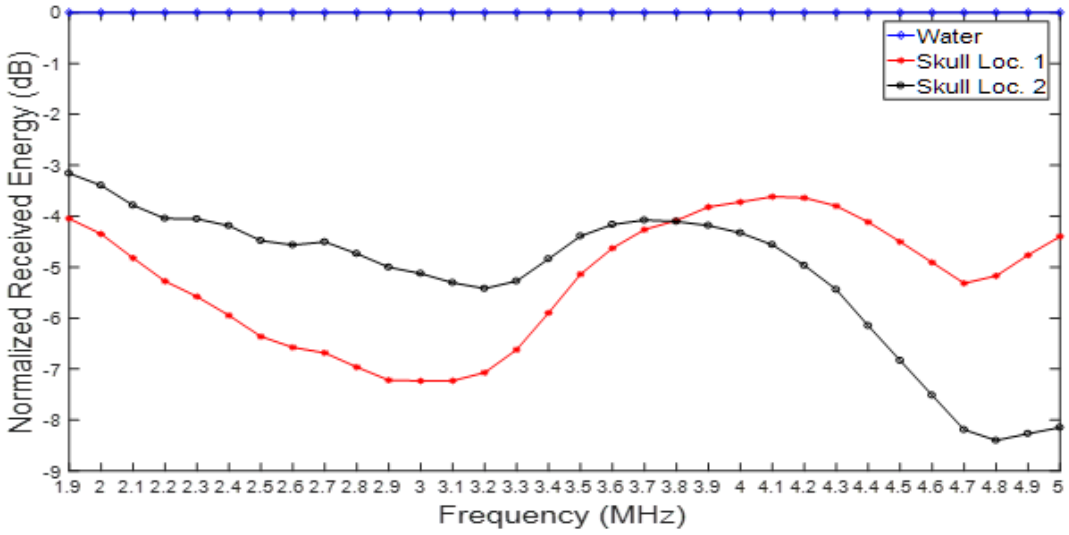

Figure 5.8: Wideband acoustic energy when the hydrophone tip was located at the DMUA geometric center, (0, 40) mm.

5.3.2 Refocusing in Water Tank and Tissue-Mimicking Phantom

In a water tank experimental setup as the one shown in Figure 5.1, we performed planar acoustic hydrophone scans of the tFUS beam with and without refocusing. The skull was placed approximately 32 mm axially from the apex of the DMUA, mimicking the skull location during our *in vivo* experiments. We selected bregma -3 mm plane to be the imaging slice of the DMUA during the scans. Figure 5.10 shows example transskull intensity patterns at 4 different frequencies without (a) and with (b) refocusing. The profiles at each frequency are normalized with respect to the maximum after refocusing. For this target location, one can make the following observations:

- At all four frequencies, the intensity patterns without refocusing have peaks at approximately 300 μm from the center in the lateral direction. This is due to the curvature of the skull and largely independent of the frequency.

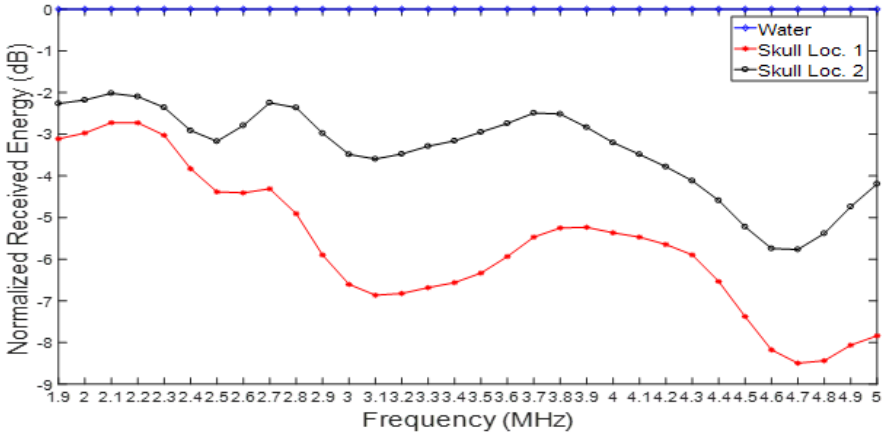

(a)

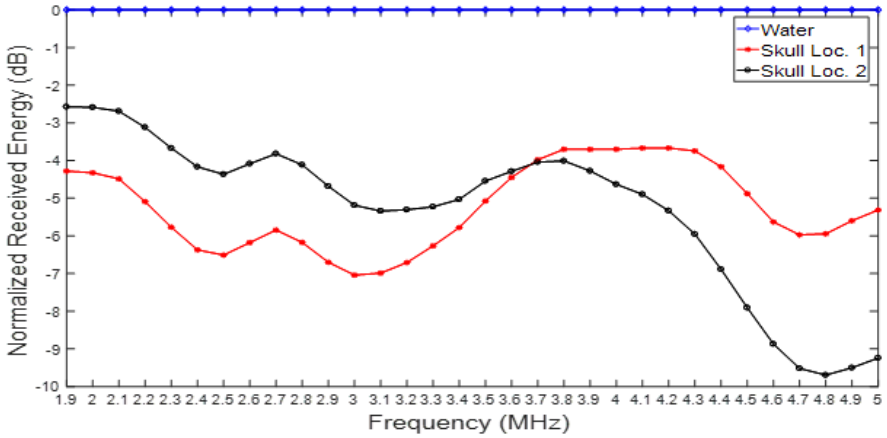

(b)

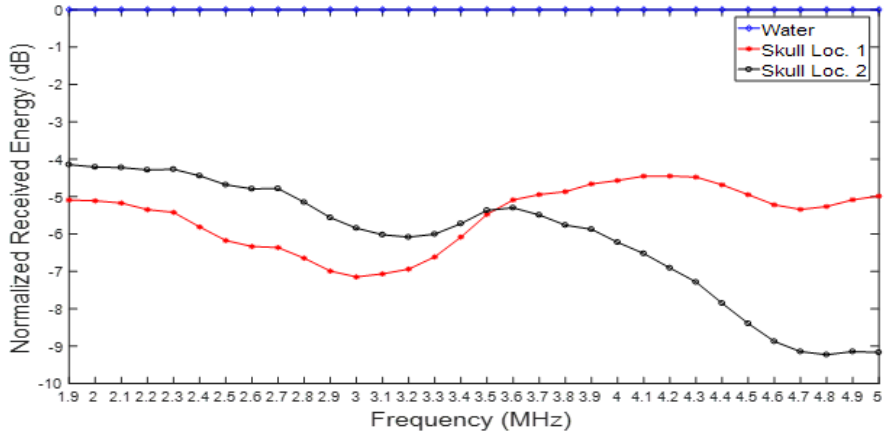

(c)

Figure 5.9: Acoustic energy received by the hydrophone when its tip was located at (a) (2, 40) mm, (b) (-2, 40) mm, and (c) (0, 38) mm from the apex of the DMUA.

Figure 5.11 clearly illustrates this point for all 32 measured intensity patterns.

- Refocusing shifts the peak intensity back towards the geometric center in the lateral direction, but has minimal effect on the position of the peak in the elevation direction. Figure 5.12 clearly illustrates this point for all 32 measured intensity patterns.

- The effect of refocusing is exhibited by reduced sidelobe levels, primarily in the lateral direction. Any effect on the sidelobes in the elevation direction is indirect.

- The improvement in focusing gain due to refocusing is a nonmonotonic function of frequency. Figure 5.13 illustrates the focal point intensity values of the scanned planes with and without refocusing at each frequency in the set. The results are normalized with respect to the maximum focusing gain achieved using the refocused tFUS beam. The red line in the figure represents the intensity values without refocusing, while the blue one represents the values with refocusing. As can be seen from the figure, there is a significant improvement in the focal point intensity due to refocusing in the frequency range from 2.5 to 4.1 MHz, and the performance is almost the same in other frequency bands.

It should be noted that we we used the same driving signal amplitude for all frequencies in the range. Therefore, the red curve (without refocusing) reflects the electrical to acoustic conversion efficiency of the DMUA. Therefore, the hydrophone measurements at frequencies in the outerbands of the transducer (below 2.5 MHz and above 4.1) may be less reliable.

To further quantify the improved focusing of transskul field patterns, we estimated the area of the focal spot from the scanned 2D intensity profiles. This was done by treating each measured profile as a 2D distribution and computing its center of mass (mean) and variance. The variance is a measure of the focal area

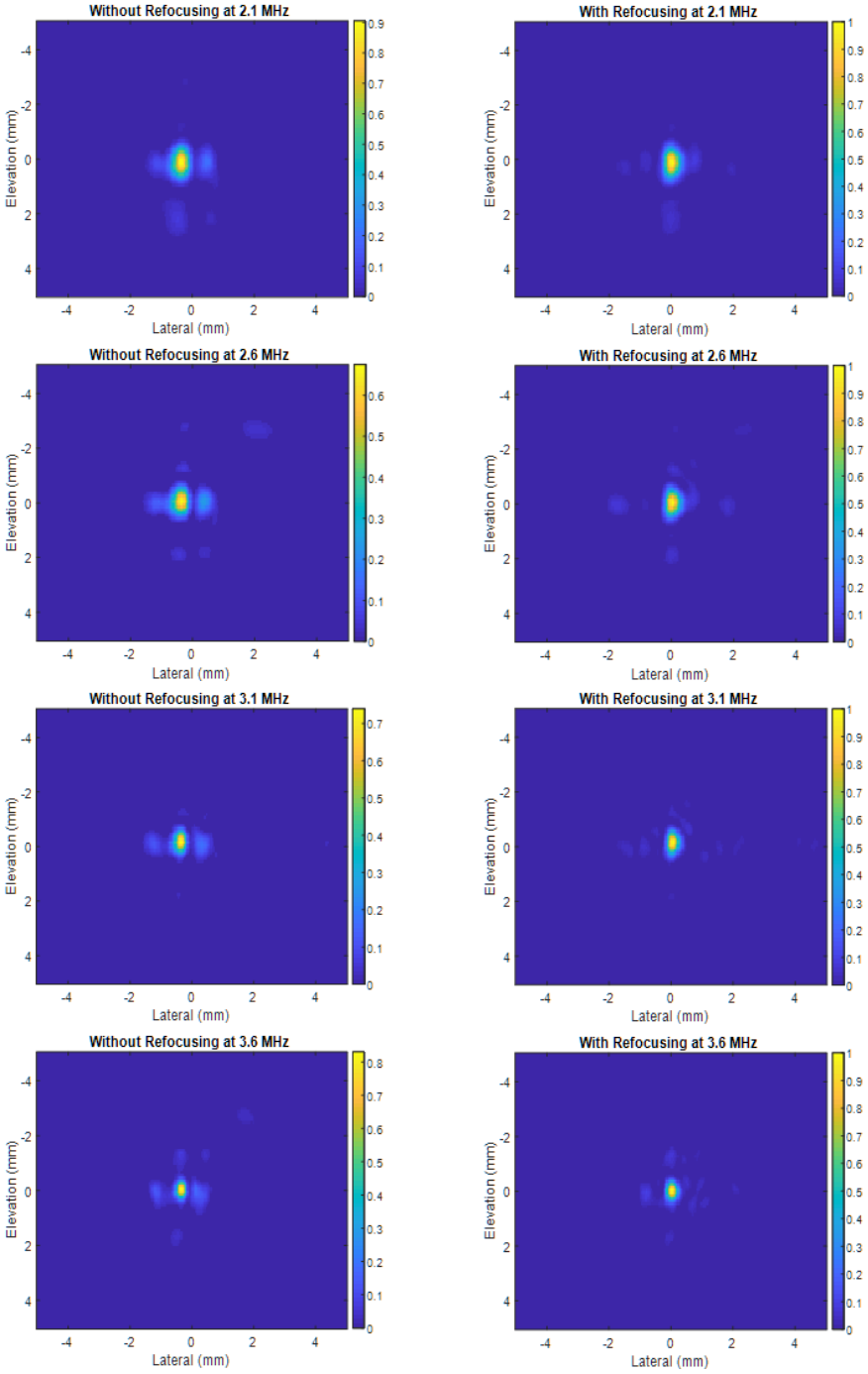

(a) (b)

Figure 5.10: Measured transskull intensity profiles at 4 different frequencies: (a) Without refocusing. (b) With refocusing. Each pair is normalized with respect to the peak of the refocused pattern.

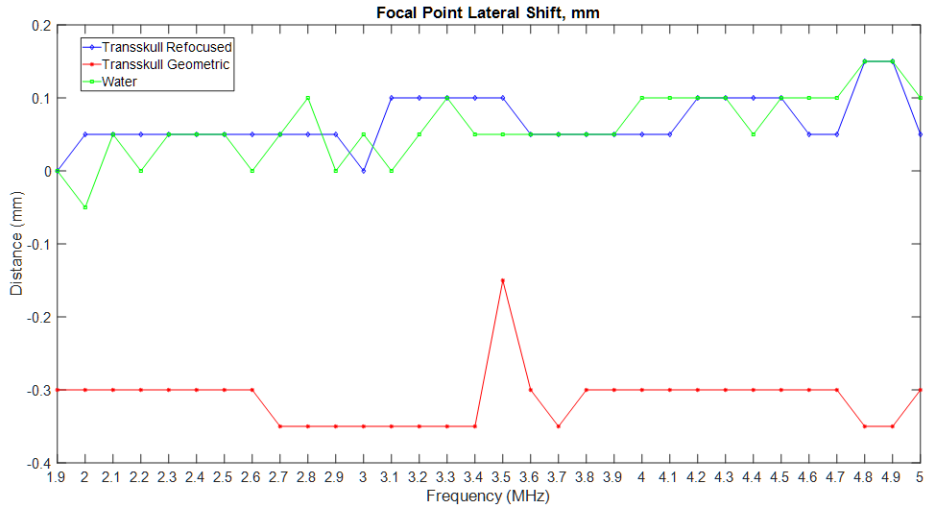

Figure 5.11: Position of the spatial peak intensity of the measured intensity profiles in the lateral direction: Water only (green), transskull without refocusing (red) and transskull with refocusing (blue).

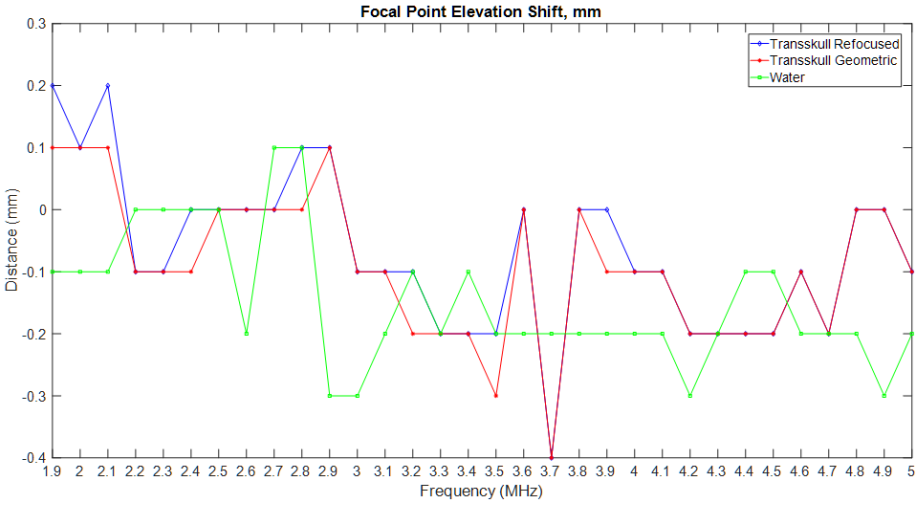

Figure 5.12: Position of the spatial peak intensity of the measured intensity profiles in the elevation direction: Water only (green), transskull without refocusing (red) and transskull with refocusing (blue).

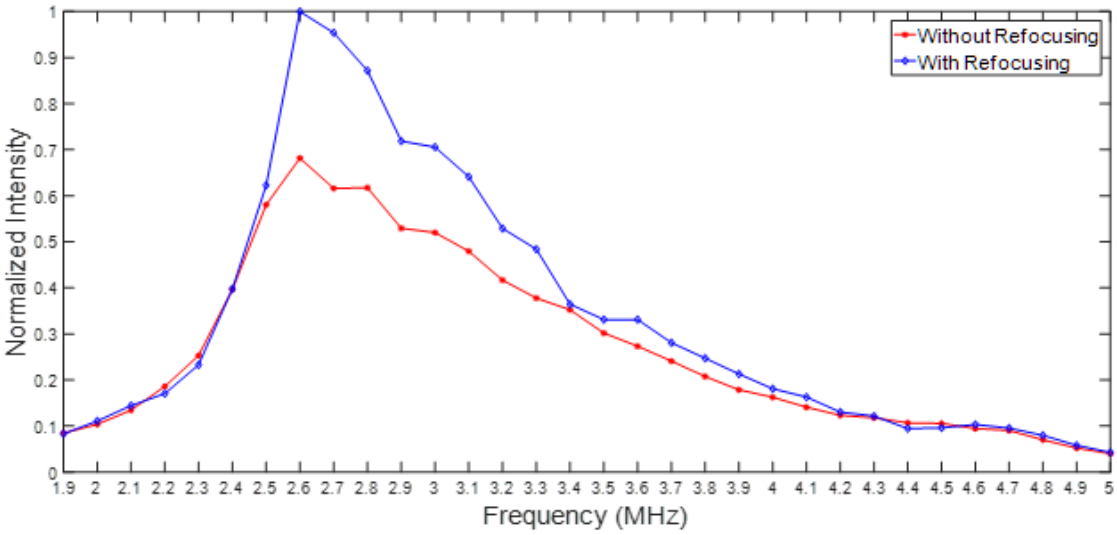

Figure 5.13: Focal point intensity as a function of frequency tank with and without refocusing.

around the center of the wavefront passing through the focal plane. The area was computed for each frequency in the range of 1.9 - 5 MHz for each intensity profile measured in plain water or transskull with and without refocusing. The result is shown in Figure 5.14, which shows approximately monotonic decrease in the focal area for the plain water measurement as expected.

The transskull measurements without refocusing are shown in red and exhibit nonmonotonic behavior. This is due to refocusing, but it should be noted that the defocusing effects appear to be much more pronounced at frequencies in the outerbands of the transducer bandwidth, where the measurements may be less reliable. The estimated focal area measurements upon refocusing are shown in blue. The graph exhibits significant reduction of area upon refocusing at all frequencies, with some variability at some frequencies[1] , especially higher frequencies above 3.7 MHz. The measurements shown in Figure 5.14 need to be confirmed by performing additional experiments in more locations and in more *ex vivo* skull samples.

[1] Measurement at 3.5 MHz was deemed unreliable and was not included.

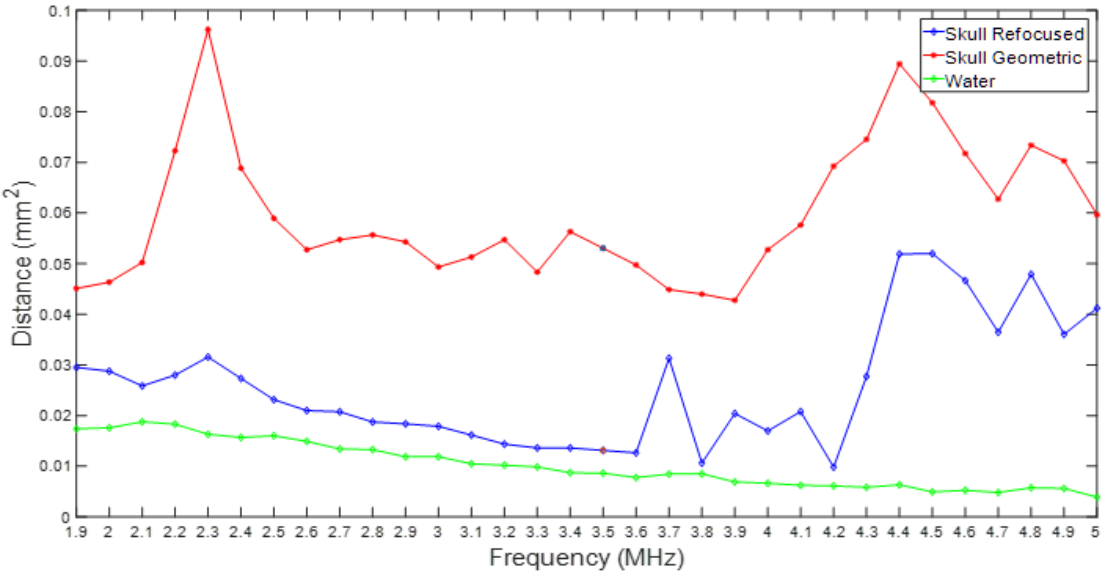

Figure 5.14: Estimated area of the focal spot of the FUS beam: Water only (green), transskull without refocusing (red) and transskull with refocusing (blue).

In the tissue-mimicking phantom experiments designed to characterize the tFUS wideband transmission improvements due to refocusing, the procedure was similar to the water tank experiments. The similarity was in terms of using rodent skull samples, generating 3D volume scan images and selecting an appropriate imaging slice of the embedded skull, and using SA imaging mode to guide the localization of the thermocouple junction at the geometric center of the DMUA. However, the excitation signals were longer in duration to generate a considerable amount of heat at the thermocouple junction. The set of the thirty-two frequencies from 1.9 to 5.0 MHz was used to generate tFUS beams with and without refocusing. The temperature due to the application of each tFUS beam for a duration of 10 seconds with and without refocusing was recorded. In Figure 5.15, we show the maximum temperature measured using the thermocouple due to the applications of the wideband transskull ultrasound beams. The blue and red curves in the figure illustrate the maximum temperature values recorded at each operating frequency with and without refocusing, respectively. It is clear that there

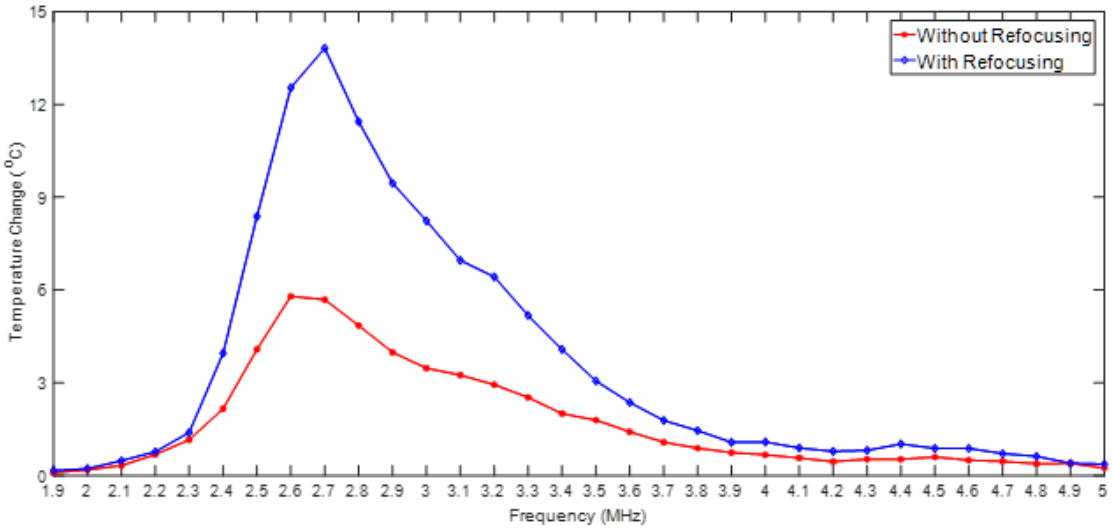

Figure 5.15: FUS-induced temperature rise as a function of operating frequency with and without refocusing.

is an improvement in maximum temperature value due to refocusing almost all operating frequency. The improvement is significant in the frequency range from 2.4 to 3.5 MHz. For example, the maximum temperature achieved due to applying a tFUS beam operating at frequency of 2.7 MHz without refocusing is about 6 °C, while it is about 14 °C with refocusing. In other words, the temperature increased by 8 °C due to applying the real-time image-based refocusing algorithm at frequency of 2.7 MHz.

In addition, we validated the feasibility of the wideband image-based refocusing in terms of heating rate improvement. We computed heating rate values of the measured temperature profiles at each frequency of the thirty-two frequencies with and without refocusing. The computations were based on the method mentioned in [69]. It basically performs smoothing and time derivative of the measured temperature values. Heating rate results are demonstrated in Figure 5.16. It is obvious from the figure that the heating rate is increased due to refocusing at each frequency within the frequency range from 2.0 to 5.0 MHz. For instance, there is about 6 °C/sec improvement in heating rate due tFUS beam refocusing

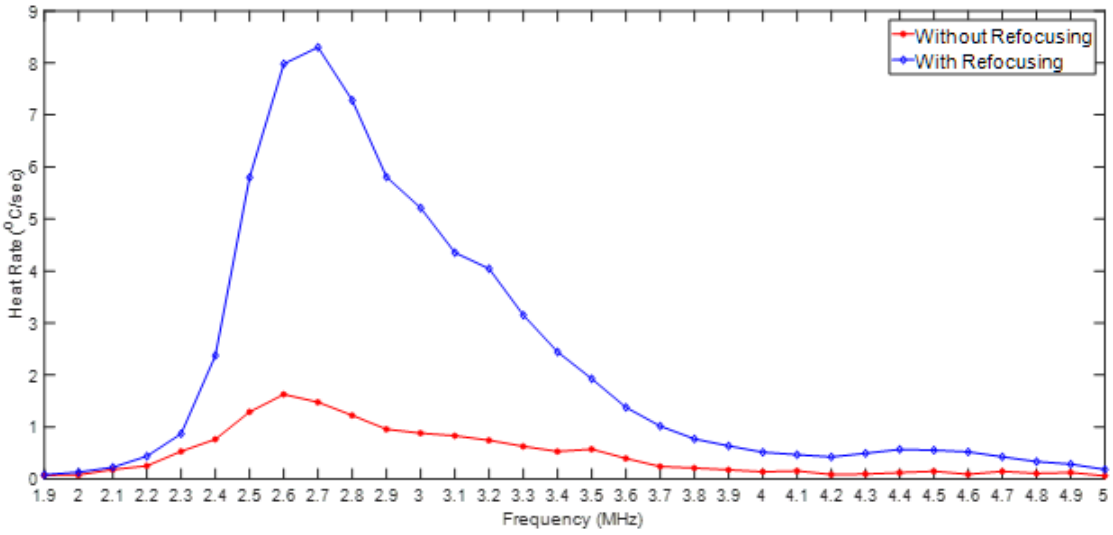

Figure 5.16: FUS-induced heating rate values as a function of operating frequency with and without refocusing.

at 2.6 MHz operating frequency. Specifically, the heating rate is about 2 °C/sec without refocusing (from the red curve), while it is 8 °C/sec with refocusing (from the blue curve).

5.4 Discussion

The results of the experimental study described in this chapter demonstrated the nature of distortions to tFUS beams as being non monotonic with high spatial dependence. They also demonstrated the value of refocusing at every available frequency within the transducer bandwidth. However, there are several limitations of this study that should be stated before final conclusions can be drawn:

1. Due to the time-consuming nature of this experiment, the key results were not repeated enough to characterize the range of variability across sufficient number of samples.

2. No effort was made to account for measurement signal to noise by adjusting

the transmit power of the different frequency components. Therefore, the measurements performed at frequencies below 2.4 MHz and above 4 MHz may be questionable.

3. The enhancement in focusing gain (heating rate) shown in Figure 4.13 may be subject to additional uncertainty. Specifically, nonlinear propagation, which could further enhance the heating rate upon refocusing. No effort was made to characterize the nonlinear generation in the tFUS beams, with or without refocusing.

4. The There are a few outlier measurements corresponding to the outer frequency bands of the transducer. In some cases, these may be indicative of severe defocusing. However, this has not been confirmed at the time of writing.

5.5 Conclusions

Despite the limitations enumerated in Sec. 5.4, it is possible to draw several useful conclusions from the results of the experimental studies on multiband refocusing:

1. The results confirm the non-monotonic nature of the loss in focusing gain of tFUS beams as a function of frequency.

2. The loss in focusing gain exhibits strong spatial dependence at the different frequency bands in the investigated range (1.9 - 5 MHz in this study).

3. For a fixed treatment plane, the variation in the focusing gain loss can be as large as 6 - 7 dB at different target points. This suggests the design of the spectral characteristics of the transmit waveforms to match the available transmission bandwidth.

4. The transmission loss experiments were performed on multiple *ex vivo* skull samples. The results varied from one sample to another, but the trends shown in Figures 5.8 and 5.9 are representative.

5. The water tank measurements showed improved confinement of the refocused FUS energy around the center of the focal beam at every frequency in the investigated range (1.9 - 5 MHz). However, it is worth noting that the measurements at frequencies outside the main bandwidth of the transducer are less reliable than those within the main bandwidth (2.5 - 4.0 MHz).

6. Measurements in the tissue mimicking phantom clearly demonstrate the improvements in focusing gain due to refocusing, but strictly within the operating bandwidth of the DMUA. The main conclusion here is that refocusing improved the gain at every frequency where reliable measurement of temperature change was made.

Finally, we conclude this chapter by pointing out that the full power of wideband refocusing is not demonstrated by the results shown herein. Such demonstration would require the synthesis of driving signals covering the full bandwidth of the transducer based on the multiband refocusing results. In principle, using wideband excitation vectors synthesized based on optimal refocusing would produce larger improvement of the therapeutic gain. The demonstration of this aspect of wideband refocusing is a subject of future studies at UISPL.

Chapter 6

Conclusion and Future Work

6.1 Conclusion

The optimization of the transcranial delivery of focused ultrasound energy to selected target points within the brain is an important problem with highly significant clinical applications. Not only do we seek the maximization of focusing gain at the target(s), but we also seek to do so while minimizing exposure to critical points in the path of the beam. The research results presented in this thesis provided experimental verification of key aspects of the optimization problem in realistic settings approximating the *in vivo* experiment setup described in [18]. The imaging capabilities of the DMUA system, especially 3D imaging to identify the suture lines [50], have played a key role in the successful completion of the experiments, which included multiple target points in multiple *ex vivo* skull samples and repeated for 32 frequency bands in the range of 1.9 - 5.0 MHz. Using 3D image guidance, target planes could be identified with submillimeter precision for both water tank and tissue-mimicking phantom experiments.

The optimization problem investigated in this thesis is structurally similar to the transthoracic refocusing problem introduced in [55] and its image-based version demonstrated experimentally in [39]. However, this dissertation describes the first experimental demonstration of the concept of focused data matrix (FDM),

which is computed from the raw channel echo data resulting from DMUA SA transmissions. The eigenvalue decomposition of the Gramian of the FDM provides an aberration correction term on top of the geometric beamforming term used in forming the FDM itself. The phase alignment due to aberration correction can be highly significant in transcranial focusing due to the fact that the whole FUS wavefront experiences the aberrations due to the skull to varying degrees. On the other hand, the bulk of the energy at the target(s) in the transthoracic focusing can be attributed to the portions of the wavefront traversing the intercostals, which suffer from less severe aberrations.

The refocusing algorithm described in this thesis is also distinctly different from the DORT method described by Parada *et al* [60, 59] in several aspects. Fundamentally, our formulation builds on the *pseudoinverse* introduced by Ebbini [66], which represents an *spatial equalization* solution well suited for multiple-focus patterns. On the other hand, the DORT method is an extension of the time reversal method introduced by Fink [58] as a *spatial matched filtering* solution. Our approach also utilizes imaging and geometric beamforming terms to improve the specificity of focusing to the selected target or multiple targets.

Our algorithm can also be distinguished from the work of Aubry *et al* [37] and Hynynen *and co workers* [52] as these methods fundamentally employ a phase conjugation (*spatial matched filtering*) based on pretreatment solutions from a computational models. Our solution is based on real-time imaging data accounting for the exact position of the array with respect to the skull (target).

To the best of our knowledge, this thesis is the first to address the frequency characterization of the transmission characteristics to selected target points transcranially. The results clearly demonstrated the nonmonotonic nature of the transmission as a function of frequency. The measured *frequency response* functions are different for different target points behind the skull and exhibit strong dependence on the portion of the skull interacting with the FUS beam. These results strongly suggest that refocusing should account for the spectral characteristics of the transmitted waveforms to achieve the *maximum focusing gain* subject to constraints

at the skull or *minimum exposure levels at the skull* subject to constraints at the target point(s). Other formulations of the optimization problem can be considered considered based on the transmission characteristics of the skull in the path of the FUS beam. This is the subject of two thesis research topics currently being pursued at the Ultrasound Imaging and Signal Processing Laboratory (UISPL).

The inherent registration between the imaging and therapeutic coordinate systems of the DMUAs allowed for exploiting imaging data to produce optimally refocused therapeutic beams. This is due to the fact that in DMUAs the imaging waveforms are a modified version of the therapeutic waveforms, where the differences are only in the waveform duty cycle and the excitation levels. In addition to the crucial advantages of synthetic aperture DMUA images in guidance, target selection and forming of the FDM, the refocusing algorithm benefited from STF imaging as a form of feedback. STF images from every refocusing experiment showed reduction in the echogenicity at the critical point with respect to the reference echogenicity at the target point upon refocusing.

The results shown in this thesis were obtained using a 1D DMUA, but they are applicable for 2D arrays with refocusing capabilities in three dimensions. In fact, the maximum improvement in focusing gain cannot be achieved without compensation for aberrations in all three spatial dimensions. Despite the limitation of using a 1D array, however, the improvements in focusing gain was measurable and significant at a range of frequencies within the transducer bandwidth. In particular, both water tank and tissue mimicking phantom experiments provided unequivocal demonstration of improved focusing gain throughout the frequency range of 1.9 - 5.0 MHz, which covers the main transducer bandwidth (2.5 - 4.0 MHz) and its outer bands. The transskull measured intensity profiles in water exhibited reduction in the effective area upon refocusing, which translates into improvement in focusing gain, since $G_I \propto A_t/\lambda^2$, where A_t is the transducer area and λ is the wavelength ([65], Eq. 2.10 p. 12). In the tissue-mimicking phantom experiments, the heating rate was used to demonstrate improved focusing gain.

Both sets of measurements showed improved focusing gain at a range of frequencies, especially the main band. It should be noted that the exposure levels were very different for the two sets of measurements, which does not allow for direct comparison. No attempt was made to reconcile any discrepancies at the time of writing of this thesis.

6.2 Future Work

In the discussion of the experiment results reported in this thesis, we have identified several limitations that must be addressed by more carefully designed experiments. Fortunately, none of these limitations is fundamental in nature and we were able to state important conclusions from our studies. These set the ground for a number of extensions to be addressed by future studies. The following are some of the more obvious suggestions:

- STF-based Refocusing Using DMUAs: One major advantage of STF imaging provided by the DMUA approach is the use of the same beamforming parameters for transmit focus patterns in both imaging and therapy modes. In STF imaging, the array excitation waveforms have μsec durations but otherwise mimic the characteristics of the therapeutic excitation waveforms (much longer in duration and/or higher amplitudes). Therefore, updating the refocusing algorithm to utilize STF-imaging data will provide the basis for an *adaptive refocusing* technique. This is based on the fact that, in all of our refocusing experiments, echogenicity changes at both the target and critical points were consistent with the expected change upon refocusing, i.e. the echogenicity the target increasing or non decreasing while the echogenicity of the critical point decreasing or non increasing.

- Adaptive Transcranial Refocusing: With the STF-based refocusing algorithm validated and its performance characterized, the way is paved for

investigating adaptive refocusing as an iterative procedure. In every iteration, refocused waveforms will be synthesized and used to generate an STF image. Afterwards, the focusing gain at selected control points will be examined to validate the sufficient improvement at the points. For instance, if the target focusing gain is no less than a minimum threshold and the critical focusing gain is no more than a maximum threshold, then this can be a stopping criterion for the iteration process.

- Quantitative Feedback for Adaptive Refocusing: In principle, changes in echogenicity at the target should reflect the increase in focusing gain upon refocusing, but this is not expected to lead to a quantitative measure of focusing gain. This is largely due to the complexity of the speckle pattern with its random constructive and destructive interference patterns. However, tissue displacement estimation using speckle tracking could provide a quantitative measure of focusing gain. Specifically, it would be possible to use *ultrasound thermography* [70] to estimate minute temperature changes due to refocused *subtherapeutic* tFUS beams. UISPL's SDUS imaging system provides an ideal vehicle for investigating the feasibility of this approach.

- Multiple Frequency Synthesis: Combining narrowband signals to synthesize a wideband signal in order to use it to drive the array of ultrasound transducer elements. In particular, we studied in this thesis the wideband refocusing at a set of discrete frequencies within the transducer bandwidth. Based on that, the most efficient frequencies that achieve desirable focusing gains at control points can be optimally combined to produce a wideband driving signal. Wideband waveforms will be able to provide images with higher spatial resolution as well as provide therapy with more efficient focusing gain than any of the narrowband waveforms.

- Utilizing 2D Array for Refocusing: The use of 2D array would have produced even higher focusing gain deep at the target location by taking advantage of the elevation direction. The experimental results presented in this thesis

were obtained using a 1D array, and the refocusing was achieved only in the axial and lateral directions.

References

[1] J. G. Lynn and T. J. Putnam, "Histology of cerebral lesions produced by focused ultrasound," *The American journal of pathology*, vol. 20, no. 3, p. 637, 1944.

[2] W. Fray, J. Barnard, F. Fray, R. Krumins, and J. Brennan, "Ultrasonic lesions in the mammalian central nervosus system," *Science*, vol. 122, no. 3168, pp. 517–518, 1955.

[3] V. Wulff, W. Fry, D. Tucker, F. J. Fry, and C. Melton, "Effects of ultrasonic vibrations on nerve tissues.," *Proceedings of the Society for Experimental Biology and Medicine*, vol. 76, no. 2, pp. 361–366, 1951.

[4] W. J. Fry, W. Mosberg Jr, J. Barnard, and F. Fry, "Production of focal destructive lesions in the central nervous system with ultrasound," *Journal of neurosurgery*, vol. 11, no. 5, pp. 471–478, 1954.

[5] W. Fry and F. Fry, "Fundamental neurological research and human neurosurgery using intense ultrasound," *IRE transactions on medical electronics*, no. 3, pp. 166–181, 1960.

[6] F. Fry, H. Ades, and W. Fry, "Production of reversible changes in the central nervous system by ultrasound," *Science*, vol. 127, no. 3289, pp. 83–84, 1958.

[7] J. Barnard, W. Fry, F. Fry, and J. Brennan, "Small localized ultrasonic lesions in the white and gray matter of the cat brain," *AMA Archives of Neurology & Psychiatry*, vol. 75, no. 1, pp. 15–35, 1956.

[8] P. Lele and A. Pierce, "The thermal hypothesis of the mechanism of ultrasonic focal destruction in organized tissues," *Interaction of ultrasound and biological tissues. FDA*, pp. 73–8008, 1972.

[9] V. Rieke and K. Butts Pauly, "Mr thermometry," *Journal of Magnetic Resonance Imaging: An Official Journal of the International Society for Magnetic Resonance in Medicine*, vol. 27, no. 2, pp. 376–390, 2008.

[10] K. Hynynen, O. Pomeroy, D. N. Smith, P. E. Huber, N. J. McDannold, J. Kettenbach, J. Baum, S. Singer, and F. A. Jolesz, "Mr imaging-guided focused ultrasound surgery of fibroadenomas in the breast: a feasibility study," *Radiology*, vol. 219, no. 1, pp. 176–185, 2001.

[11] K. Hynynen, N. McDannold, G. Clement, F. A. Jolesz, E. Zadicario, R. Killiany, T. Moore, and D. Rosen, "Pre-clinical testing of a phased array ultrasound system for mri-guided noninvasive surgery of the braina primate study," *European journal of radiology*, vol. 59, no. 2, pp. 149–156, 2006.

[12] C. M. Tempany, E. A. Stewart, N. McDannold, B. J. Quade, F. A. Jolesz, and K. Hynynen, "Mr imaging–guided focused ultrasound surgery of uterine leiomyomas: a feasibility study," *Radiology*, vol. 226, no. 3, pp. 897–905, 2003.

[13] R. Salomir, A.-S. Delemazure, J. Palussière, O. Rouvière, F. Cotton, and J.-Y. Chapelon, "Image-based control of the magnetic resonance imaging-guided focused ultrasound thermotherapy," *Topics in Magnetic Resonance Imaging*, vol. 17, no. 3, pp. 139–151, 2006.

[14] M. Bayat, J. R. Ballard, and E. S. Ebbini, "Adaptive motion compensation for in vivo ultrasound temperature estimation," in *Ultrasonics Symposium (IUS), 2013 IEEE International*, pp. 1797–1800, IEEE, 2013.

[15] D. Liu and E. S. Ebbini, "Real-time 2-d temperature imaging using ultrasound," *IEEE transactions on bio-medical engineering*, vol. 57, no. 1, p. 12, 2010.

[16] R. Souchon, L. Soualmi, M. Bertrand, J.-Y. Chapelon, F. Kallel, and J. Ophir, "Ultrasonic elastography using sector scan imaging and a radial compression," *Ultrasonics*, vol. 40, no. 1-8, pp. 867–871, 2002.

[17] E. S. Ebbini, H. Yao, and A. Shrestha, "Dual-mode ultrasound phased arrays for image-guided surgery," *Ultrasonic Imaging*, vol. 28, no. 2, pp. 65–82, 2006.

[18] A. Haritonova, D. Liu, and E. S. Ebbini, "In vivo application and localization of transcranial focused ultrasound using dual-mode ultrasound arrays," *IEEE transactions on ultrasonics, ferroelectrics, and frequency control*, vol. 62, no. 12, pp. 2031–2042, 2015.

[19] N. McDannold, G. T. Clement, P. Black, F. Jolesz, and K. Hynynen, "Transcranial magnetic resonance imaging–guided focused ultrasound surgery of brain tumors: initial findings in 3 patients," *Neurosurgery*, vol. 66, no. 2, pp. 323–332, 2010.

[20] E. Martin, D. Jeanmonod, A. Morel, E. Zadicario, and B. Werner, "High-intensity focused ultrasound for noninvasive functional neurosurgery," *Annals of Neurology: Official Journal of the American Neurological Association and the Child Neurology Society*, vol. 66, no. 6, pp. 858–861, 2009.

[21] M. Kinoshita, N. McDannold, F. A. Jolesz, and K. Hynynen, "Noninvasive localized delivery of herceptin to the mouse brain by mri-guided focused ultrasound-induced blood–brain barrier disruption," *Proceedings of the National Academy of Sciences*, vol. 103, no. 31, pp. 11719–11723, 2006.

[22] W. Legon, T. F. Sato, A. Opitz, J. Mueller, A. Barbour, A. Williams, and W. J. Tyler, "Transcranial focused ultrasound modulates the activity of primary somatosensory cortex in humans," *Nature neuroscience*, vol. 17, no. 2, p. 322, 2014.

[23] J. Manlapaz, K. Åström, H. Ballantine Jr, and P. Lele, "Effects of ultrasonic radiation in experimental focal epilepsy in the cat," *Experimental neurology*, vol. 10, no. 4, pp. 345–356, 1964.

[24] H. Kim, S. J. Taghados, K. Fischer, L.-S. Maeng, S. Park, and S.-S. Yoo, "Noninvasive transcranial stimulation of rat abducens nerve by focused ultrasound," *Ultrasound in medicine & biology*, vol. 38, no. 9, pp. 1568–1575, 2012.

[25] R. L. King, J. R. Brown, and K. B. Pauly, "Localization of ultrasound-induced in vivo neurostimulation in the mouse model," *Ultrasound in medicine & biology*, vol. 40, no. 7, pp. 1512–1522, 2014.

[26] H. Kim, S. D. Lee, A. Chiu, S.-S. Yoo, and S. Park, "Estimation of the spatial profile of neuromodulation and the temporal latency in motor responses induced by focused ultrasound brain stimulation," *Neuroreport*, vol. 25, no. 7, p. 475, 2014.

[27] R. L. King, J. R. Brown, W. T. Newsome, and K. B. Pauly, "Effective parameters for ultrasound-induced in vivo neurostimulation," *Ultrasound in medicine & biology*, vol. 39, no. 2, pp. 312–331, 2013.

[28] T. Deffieux, Y. Younan, N. Wattiez, M. Tanter, P. Pouget, and J.-F. Aubry, "Low-intensity focused ultrasound modulates monkey visuomotor behavior," *Current Biology*, vol. 23, no. 23, pp. 2430–2433, 2013.

[29] E. Mehić, J. M. Xu, C. J. Caler, N. K. Coulson, C. T. Moritz, and P. D. Mourad, "Increased anatomical specificity of neuromodulation via modulated focused ultrasound," *PLoS One*, vol. 9, no. 2, p. e86939, 2014.

[30] W. J. Elias, N. Lipsman, W. G. Ondo, P. Ghanouni, Y. G. Kim, W. Lee, M. Schwartz, K. Hynynen, A. M. Lozano, B. B. Shah, *et al.*, "A randomized trial of focused ultrasound thalamotomy for essential tremor," *New England Journal of Medicine*, vol. 375, no. 8, pp. 730–739, 2016.

[31] M. Rohani and A. Fasano, "Focused ultrasound for essential tremor: review of the evidence and discussion of current hurdles," *Tremor and Other Hyperkinetic Movements*, vol. 7, 2017.

[32] W. S. Chang, H. H. Jung, E. J. Kweon, E. Zadicario, I. Rachmilevitch, and J. W. Chang, "Unilateral magnetic resonance guided focused ultrasound thalamotomy for essential tremor: practices and clinicoradiological outcomes," *J Neurol Neurosurg Psychiatry*, vol. 86, no. 3, pp. 257–264, 2015.

[33] N. Lipsman, M. L. Schwartz, Y. Huang, L. Lee, T. Sankar, M. Chapman, K. Hynynen, and A. M. Lozano, "Mr-guided focused ultrasound thalamotomy for essential tremor: a proof-of-concept study," *The Lancet Neurology*, vol. 12, no. 5, pp. 462–468, 2013.

[34] J. Sun and K. Hynynen, "Focusing of therapeutic ultrasound through a human skull: a numerical study," *The Journal of the Acoustical Society of America*, vol. 104, no. 3, pp. 1705–1715, 1998.

[35] K. Shapoori, J. Sadler, A. Wydra, E. V. Malyarenko, A. N. Sinclair, and R. G. Maev, "An ultrasonic-adaptive beamforming method and its application for trans-skull imaging of certain types of head injuries; part i: Transmission mode," *IEEE Transactions on Biomedical Engineering*, vol. 62, no. 5, pp. 1253–1264, 2015.

[36] T. W. Barber, J. A. Brockway, and L. S. Higgins, "The density of tissues in and about the head," *Acta neurologica scandinavica*, vol. 46, no. 1, pp. 85–92, 1970.

[37] J.-F. Aubry, M. Tanter, M. Pernot, J.-L. Thomas, and M. Fink, "Experimental demonstration of noninvasive transskull adaptive focusing based on prior computed tomography scans," *The Journal of the Acoustical Society of America*, vol. 113, no. 1, pp. 84–93, 2003.

[38] K. Hynynen and J. Sun, "Trans-skull ultrasound therapy: The feasibility of using image-derived skull thickness information to correct the phase distortion," *IEEE transactions on ultrasonics, ferroelectrics, and frequency control*, vol. 46, no. 3, pp. 752–755, 1999.

[39] J. R. Ballard, A. J. Casper, Y. Wan, and E. S. Ebbini, "Adaptive transthoracic refocusing of dual-mode ultrasound arrays," *IEEE Transactions on Biomedical Engineering*, vol. 57, no. 1, pp. 93–102, 2010.

[40] P. Dumas, J. Poguet, and G. F.-I. SA, "Piezocomposite technology an innovative approach to the improvement of ndt performance using ultrasounds," in *8th European Conference on Non Destructive Testing, June 2002, Barcelona, Spain*, 2002.

[41] G. Fleury, D. M. de Lima, K. Hynynen, R. Berriet, O. Le Baron, and B. Huguenin, "New piezocomposite transducers for therapeutic ultrasound," in *Thermal Treatment of Tissue: Energy Delivery and Assessment II*, vol. 4954, pp. 227–237, International Society for Optics and Photonics, 2003.

[42] Y. Wan and E. S. Ebbini, "Imaging with concave large-aperture therapeutic ultrasound arrays using conventional synthetic-aperture beamforming," *IEEE transactions on ultrasonics, ferroelectrics, and frequency control*, vol. 55, no. 8, 2008.

[43] R. Mucci, "A comparison of efficient beamforming algorithms," *IEEE Transactions on Acoustics, Speech, and Signal Processing*, vol. 32, no. 3, pp. 548–558, 1984.

[44] R. L. Tutwiler, "Ultrasonic beamforming architectures," in *Medical Imaging 1998: Ultrasonic Transducer Engineering*, vol. 3341, pp. 43–55, International Society for Optics and Photonics, 1998.

[45] T. L. Szabo, *Diagnostic ultrasound imaging: inside out*. Academic Press, 2004.

[46] A. V. Oppenheim, *Discrete-time signal processing*. Pearson Education India, 1999.

[47] J. A. Jensen, S. I. Nikolov, K. L. Gammelmark, and M. H. Pedersen, "Synthetic aperture ultrasound imaging," *Ultrasonics*, vol. 44, pp. e5–e15, 2006.

[48] P. Corl and G. Kino, "A real-time synthetic-aperture imaging system," in *Acoustical Imaging*, pp. 341–355, Springer, 1980.

[49] R. F. Wagner, M. F. Insana, and S. W. Smith, "Fundamental correlation lengths of coherent speckle in medical ultrasonic images," *IEEE transactions on ultrasonics, ferroelectrics, and frequency control*, vol. 35, no. 1, pp. 34–44, 1988.

[50] D. Liu, K. Schaible, W. Low, and E. S. Ebbini, "Three-dimensional image guidance for transcranial focused ultrasound therapy," in *Biomedical Imaging (ISBI 2017), 2017 IEEE 14th International Symposium on*, pp. 916–919, IEEE, 2017.

[51] F. Fry and J. Barger, "Acoustical properties of the human skull," *The Journal of the Acoustical Society of America*, vol. 63, no. 5, pp. 1576–1590, 1978.

[52] K. Hynynen and F. A. Jolesz, "Demonstration of potential noninvasive ultrasound brain therapy through an intact skull," *Ultrasound in medicine & biology*, vol. 24, no. 2, pp. 275–283, 1998.

[53] F. Fry, "Transkull transmission of an intense focused ultrasonic beam," *Ultrasound in Medicine and Biology*, vol. 3, no. 2, pp. 183–184, 1977.

[54] R. Seip, P. VanBaren, and E. S. Ebbini, "Dynamic focusing in ultrasound hyperthermia treatments using implantable hydrophone arrays," *IEEE transactions on ultrasonics, ferroelectrics, and frequency control*, vol. 41, no. 5, pp. 706–713, 1994.

[55] Y. Y. Botros, E. S. Ebbini, and J. L. Volakis, "Two-step hybrid virtual array ray(var) technique for focusing through the rib cage," *IEEE transactions on ultrasonics, ferroelectrics, and frequency control*, vol. 45, no. 4, pp. 989–1000, 1998.

[56] D. White, J. Clark, J. Chesebrough, M. White, and J. Campbell, "Effect of the skull in degrading the display of echoencephalographic b and c scans," *The Journal of the Acoustical Society of America*, vol. 44, no. 5, pp. 1339–1345, 1968.

[57] D. White, J. Clark, D. White, J. Campbell, K. Bahuleyan, A. Kraus, and R. Brinker, "The deformation of the ultrasonic field in passage across the living and cadaver head," *Medical and biological engineering*, vol. 7, no. 6, pp. 607–618, 1969.

[58] M. Fink, "Time reversal of ultrasonic fields. i. basic principles," *IEEE transactions on ultrasonics, ferroelectrics, and frequency control*, vol. 39, no. 5, pp. 555–566, 1992.

[59] C. Prada, J.-L. Thomas, and M. Fink, "The iterative time reversal process: Analysis of the convergence," *The Journal of the Acoustical Society of America*, vol. 97, no. 1, pp. 62–71, 1995.

[60] C. Prada, S. Manneville, D. Spoliansky, and M. Fink, "Decomposition of the time reversal operator: Detection and selective focusing on two scatterers," *The Journal of the Acoustical Society of America*, vol. 99, no. 4, pp. 2067–2076, 1996.

[61] J. Sun and K. Hynynen, "Focusing of therapeutic ultrasound through a human skull: a numerical study," *The Journal of the Acoustical Society of America*, vol. 104, no. 3, pp. 1705–1715, 1998.

[62] R. M. Jones and K. Hynynen, "Comparison of analytical and numerical approaches for ct-based aberration correction in transcranial passive acoustic imaging," *Physics in Medicine & Biology*, vol. 61, no. 1, p. 23, 2015.

[63] G. Maimbourg, A. Houdouin, T. Deffieux, M. Tanter, and J.-F. Aubry, "3d-printed adaptive acoustic lens as a disruptive technology for transcranial ultrasound therapy using single-element transducers," *Physics in Medicine & Biology*, vol. 63, no. 2, p. 025026, 2018.

[64] A. J. Casper, D. Liu, J. R. Ballard, and E. S. Ebbini, "Real-time implementation of a dual-mode ultrasound array system: In vivo results," *IEEE Transactions on Biomedical Engineering*, vol. 60, no. 10, pp. 2751–2759, 2013.

[65] E. S. Ebbini, *Deep localized hyperthermia with ultrasound-phased arrays using the pseudoinverse pattern synthesis method*. PhD thesis, University of Illinois at Urbana-Champaign, 1990.

[66] E. Ebbini and C. Cain, "Optimization of the intensity gain of multiple-focus phased-array heating patterns," *International journal of hyperthermia*, vol. 7, no. 6, pp. 953–973, 1991.

[67] T. J. Hall, M. Bilgen, M. F. Insana, and T. A. Krouskop, "Phantom materials for elastography," *IEEE transactions on ultrasonics, ferroelectrics, and frequency control*, vol. 44, no. 6, pp. 1355–1365, 1997.

[68] K. R. Nightingale, M. L. Palmeri, R. W. Nightingale, and G. E. Trahey, "On the feasibility of remote palpation using acoustic radiation force," *The Journal of the Acoustical Society of America*, vol. 110, no. 1, pp. 625–634, 2001.

[69] A. Savitzky and M. J. Golay, "Smoothing and differentiation of data by simplified least squares procedures.," *Analytical chemistry*, vol. 36, no. 8, pp. 1627–1639, 1964.

[70] E. S. Ebbini, C. Simon, and D. Liu, "Real-time ultrasound thermography and thermometry [life sciences]," *IEEE Signal Processing Magazine*, vol. 35, pp. 166–174, March 2018.

[71] J. Lockwood and J. Willette, "High-speed method for computing the exact solution for the pressure variations in the nearfield of a baffled piston," *The Journal of the Acoustical Society of America*, vol. 53, no. 3, pp. 735–741, 1973.

[72] R. J. McGough, "Rapid calculations of time-harmonic nearfield pressures produced by rectangular pistons," *The Journal of the Acoustical Society of America*, vol. 115, no. 5, pp. 1934–1941, 2004.

[73] J. A. Jensen and N. B. Svendsen, "Calculation of pressure fields from arbitrarily shaped, apodized, and excited ultrasound transducers," *IEEE transactions on ultrasonics, ferroelectrics, and frequency control*, vol. 39, no. 2, pp. 262–267, 1992.

[74] K. B. Ocheltree and L. Frizzel, "Sound field calculation for rectangular sources," *IEEE transactions on ultrasonics, ferroelectrics, and frequency control*, vol. 36, no. 2, pp. 242–248, 1989.

Appendix A

Acronyms

Care has been taken in this thesis to minimize the use of jargon and acronyms, but this cannot always be achieved. The appendix contains a table of acronyms and their meaning.

A.1 Acronyms

Table A.1: Acronyms

Acronym	**Meaning**
FUS	Focused Ultrasound
MRI	Magnetic Resonance Imaging
DMUA	Dual-Mode Ultrasound Array
ThxOF	Therapeutic Operating Field
SA	Synthetic Aperture
STF	Single Transmit Focus
FDM	Focused Data Matrix
MRgFUS	Magnetic Resonance Guided Focused Ultrasound
USgFUS	Ultrasound-guided Focused Ultrasound
HIFU	High-Intensity Focused Ultrasound
tFUS	Transcranial Focused Ultrasound
A/D	Analog to Digital Converter
RF	Radiofrequency

A.2 DMUA and Acoustic Field Simulation

Many researchers have proposed different methods to mathematically formulate and simulate acoustic radiation patterns of an ultrasound source in a homogenous medium [71], [72], [73]. Ocheltree and Frizzel [74] developed an efficient method for computing the acoustic field of a continuous wave (CW) generated from a rectangular ultrasound source. According to this method, each DMUA element is divided into a set of rectangular sub-elements, and the directivity from each sub-element (n) in the array to a control point (m) can be formulated as in Equation A.1,

$$h(m,n) = \frac{j\rho ck}{2\pi} \int_{-h/2}^{h/2} \int_{-w/2}^{w/2} \frac{e^{(\alpha+jk)r}}{r} dx_o dy_o, \tag{A.1}$$

where ρ is the medium density, c is the speed of sound, k is the wave number, α is the attenuation coefficient, r is the distance between the differential area of the sub-element (n) to the control point (m), h and w are the height and width of the sub-element, respectively.

The complex acoustic pressure at the control point location due to a particle velocity (u) normal to the sub-element surface can be expressed as in Equation A.2,

$$p(r) = \frac{j\rho ck}{2\pi} u \int_{-h/2}^{h/2} \int_{-w/2}^{w/2} \frac{e^{(\alpha+jk)r}}{r} dx_o dy_o. \tag{A.2}$$

For an array consisting of N elements, each element would contribute in creating the acoustic pressure at the control point. Considering a linear system approach, the superposition principle can be applied to compute the generated acoustic pressure (p_o) at the point location. Equation A.3 shows the total acoustic pressure at a control point (m) due to an ultrasound array of N elements.

$$p_o = \frac{j\rho ck}{2\pi} \sum_{n=1}^{N} u \int_{-h/2}^{h/2} \int_{-w/2}^{w/2} \frac{e^{(\alpha+jk)r}}{r} dx_o dy_o. \tag{A.3}$$

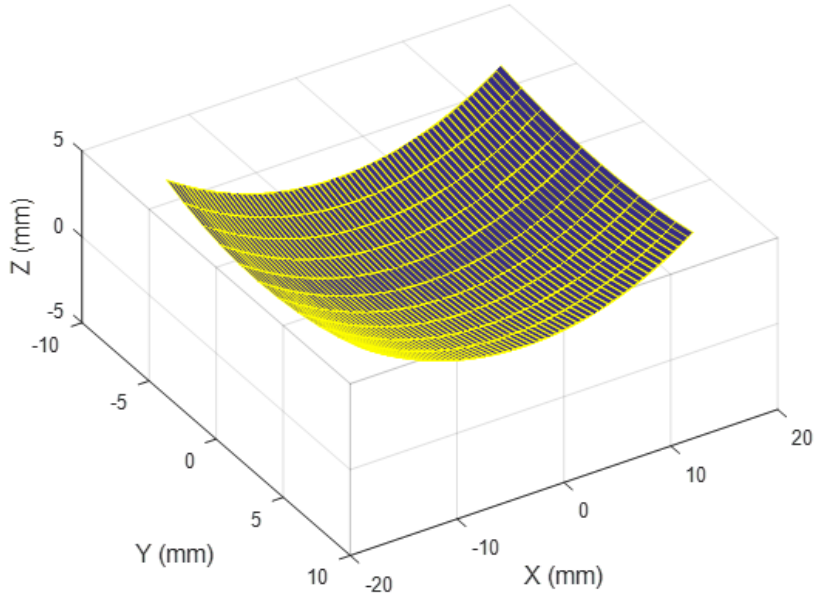

Figure A.1: Simulation of a 64-element ultrasound phased array.

As demonstrated in [74], Equation A.3 can be simplified in to the following:

$$p_o = \frac{j\rho ck\Delta S}{2\pi}\sum_{n=1}^{N}\frac{u}{R}e^{-(\alpha+jk)R}sinc(\frac{k\acute{x_n}w}{2R})sinc(\frac{k\acute{y_n}h}{2R}), \tag{A.4}$$

where R is the distance from the center of each array element to the control point, ΔS is the surface area of each element, $\acute{x_n}$ and $\acute{y_n}$ are the distances between the center of the array and each array element in the x and y directions, respectively.

Figure A.1 shows a simulation of a 64-elements ultrasound phased array. The array is concave, as can be seen from the figure, with 40-mm radius of curvature. Each element of the array is diced into ten elements, therefore, a total of 640 rectangular sub-element are generated.

The simulation results of using the phased array shown in Figure A.1 to generate acoustic field at specific control point are demonstrated in the following

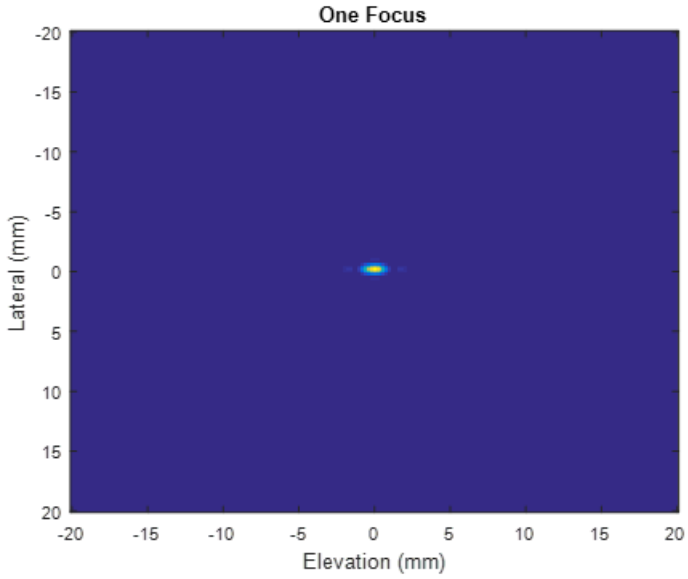

Figure A.2: Single focus simulation at the geometric center of the array in the lateral-elevation plane.

discussion. Figure A.2 illustrates the simulation result of generating a single focus at the geometric center of the phased array in the lateral-elevation plane. The geometric center is located at (0, 0, 40) mm in the lateral, elevation, axial directions, respectively. Moreover, we simulated the acoustic field of the array in the lateral-axial direction as depicted in Figure A.3.

In addition, we used the simulated phased array to generate multiple foci field patterns. Figure A.4 shows the simulation results of generating two foci acoustic field pattern in the lateral-elevation plane. The foci were designed to be shifted from the geometric center of the array by ±2mm in the lateral direction. Figure A.5 illustrates the results in the lateral-axial plane.

The simulation result of creating three foci pattern in the lateral-elevation plane is demonstrated in Figure A.6. The foci locations were designed to be at the phased array geometric center and ±2mm out of the geometric center in the lateral direction.

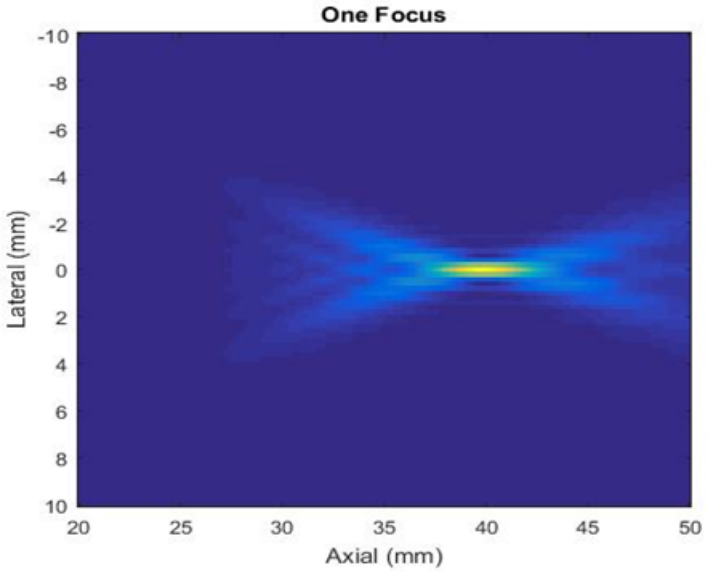

Figure A.3: Single focus simulation at the geometric center of the array in the lateral-axial plane.

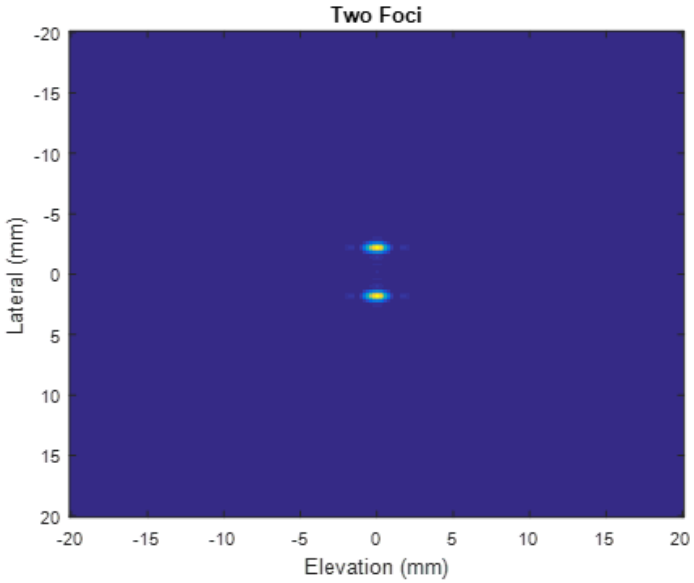

Figure A.4: Two foci simulation result in the lateral-elevation plane.

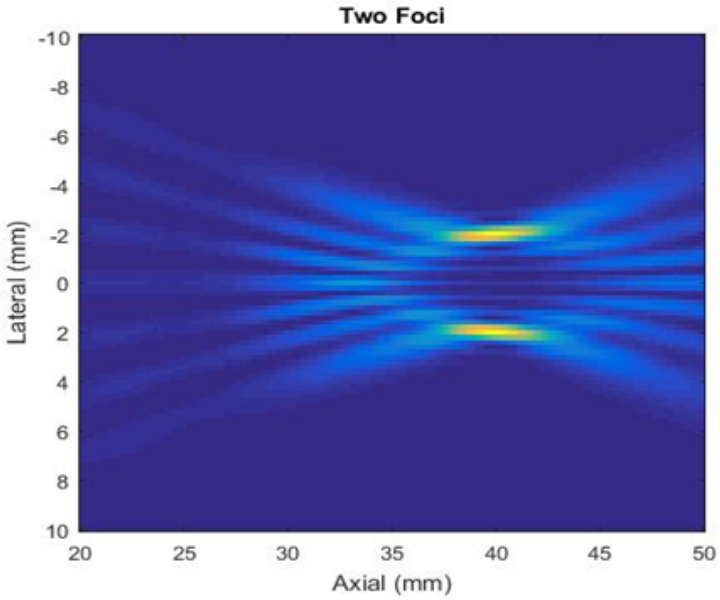

Figure A.5: Two foci simulation result in the lateral-axial plane.

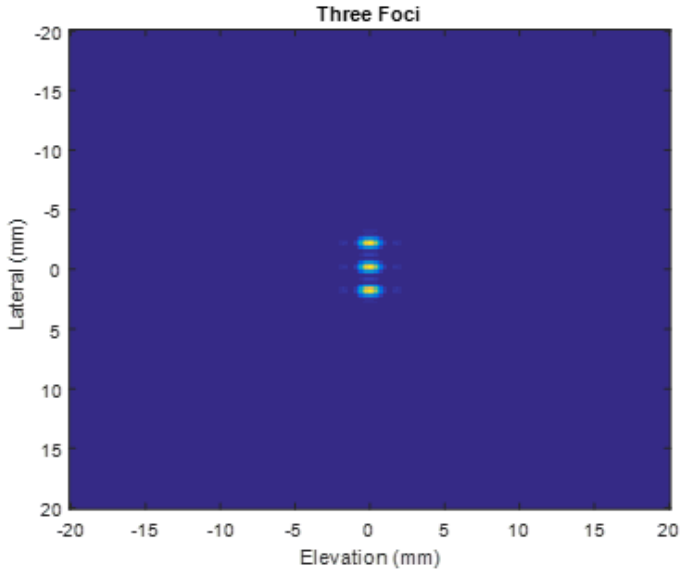

Figure A.6: Three foci simulation result in the lateral-elevation plane.